Antenna Characterization using Phaseless Near-field Measurements

Trevor Brown

A Thesis submitted to the Faculty of Graduate Studies of the University of Manitoba in partial fulfillment of the requirements for the degree of

Master of Science

Department of Electrical and Computer Engineering
University of Manitoba
Winnipeg, Manitoba, Canada

Abstract

This thesis focuses on the application of electromagnetic inverse source techniques to characterize antennas using phaseless (amplitude-only) near-field (NF) measurement data. Removing the need to measure phase reduces the overall cost of the measurement apparatus since simple power meters can be used instead of expensive vector network analyzers. It has also been shown in the literature that a phaseless approach can improve the accuracy of the calculated far-field (FF) pattern in the presence of probe positioning errors compared to the amplitude-and-phase approach. A brief discussion on the state-of-the-art methods for characterizing antennas using phaseless near-field measurement data is presented. Two general approaches used most often to perform near-field to far-field (NF-FF) transformations, namely modal expansion and source reconstruction, are explained in detail for scenarios with and without phase information. A phaseless source reconstruction method (SRM) is the primary focus of this work. The SRM is an application of an electromagnetic inverse source technique and therefore, the complexities of solving the associated ill-posed inverse source problem are discussed. The application of the SRM to spherical and planar measurement geometries are presented along with the concerns regarding regularization resulting from discretizing the ill-posed system. A multiplicative regularization (MR) scheme originally developed for inverse scattering is adapted to suit the nonlinear cost functional for the phaseless planar measurement case and the mathematical framework is derived in detail. The resulting MR-SRM is fully automated and incorporates adaptive regularization. The developed algorithms are evaluated using several examples with synthetic phaseless NF data demonstrating the benefits and limitations of the source reconstruction method and the multiplicative regularization scheme. The application of the SRM to antenna diagnostics using phaseless NF data is also shown. Finally, the developed planar algorithms are tested with experimentally collected phaseless measurement data to demonstrate their potential as suitable antenna characterization techniques that can be of interest to the antenna measurement community.

Contributions

This thesis includes the following contributions:

- The development of a MATLAB computer code that can perform near-field to far-field transformations using the source reconstruction method for both planar and spherical measurement geometries. The code is capable of the following:
  - Characterizes antennas using near-field measurement data with or without phase information
  - Provides diagnostic information via the generated equivalent currents
  - Generates the normalized far-field radiation pattern
  - Produces synthetic near-field measurement data for testing purposes
  - Uses adaptive cross approximation to accelerate the SRM for spherical measurements
- The multiplicatively regularized source reconstruction method was proposed and developed. To this end, a multiplicative regularization scheme originally developed for inverse scattering was modified and extended to suit the planar source reconstruction problem for phaseless NF measurements. The mathematical framework for the regularization scheme was derived and implemented in the developed code.
- The developed algorithms were evaluated using synthetic data, and in the case of the planar measurement code, using experimental data as well. The developed planar techniques were also compared with state-of-the-art alternatives that were based on the concept of modal expansion.

Below we provide a list of the published works resulting from this research.

Refereed Journal Papers

1. **Trevor Brown**, Ian Jeffrey, and Puyan Mojabi. "Multiplicatively Regularized Source Reconstruction Method for Phaseless Planar Near-Field Antenna Measurements". IEEE Transactions on Antennas and Propagation. Manuscript ID: AP1507-1047.R2. Submitted July 2015 [Under Review].

Refereed Conference Papers

1. Puyan Mojabi, Nariman Firoozy, Nozhan Bayat, **Trevor Brown**, Chaitanya Narendra, Pedram Mojabi, Chen Niu, Tyler Tiede, Thomas Neusitzer, Xiang Li, Ian Jeffrey, Joe LoVetri, and David Barber. "Electromagnetic Inversion for Biomedical Imaging, Antenna Characterization, and Sea Ice Remote Sensing Applications". URSI Asia-Pacific Radio Science Conference, August 21-25, 2016. Paper ID: S-K7_1003.

2. **Trevor Brown**, Ian Jeffrey, and Puyan Mojabi. "On the Use of Pre-Scaled Data with the Source Reconstruction Method for Near-field Antenna Measurement". Radio Science Meeting (Joint with AP-S Symposium), June 25 - July 1, 2016. Paper ID: 2198.

3. Chaitanya Narendra, Ian Jeffrey, **Trevor Brown**, Jonatan Aronsson, and Puyan Mojabi. "Hierarchical Matrix Acceleration of the Source Reconstruction Method for Antenna Measurements". Radio Science Meeting (Joint with AP-S Symposium), June 25 - July 1, 2016. Paper ID: 2240.

4. **Trevor Brown**, Ian Jeffrey, and Puyan Mojabi. "Multiplicatively Regularized Source Reconstruction Method for Phaseless Near-Field Antenna Measurements". Radio Science Meeting (Joint with AP-S Symposium), 2015 USNC-URSI, pp. 73, 19-24 July, 2015.

Technical Reports

1. **Trevor Brown**, Chaitanya Narendra, Chen Niu, and Puyan Mojabi. "NSERC Engage Project: Phaseless Inversion of Planar Magnetic Near-Field Antenna Measurements". Technical report presented to EMSCAN Corp. (Not Published), Calgary, AB, Canada, Mar. 2016. (20pp)

2. **Trevor Brown**, Chaitanya Narendra, Ian Jeffrey, and Puyan Mojabi. "NSERC Engage Project: The Source Reconstruction Method for Near-Field Antenna Measurements". Technical report presented to NovAtel Inc. (Not Published), Calgary, AB, Canada, Feb. 2015. (23pp)

Acknowledgements

First of all I would like to thank my academic advisors, Dr. Puyan Mojabi and Dr. Ian Jeffrey, for their endless advice, support, and friendship over the past few years. They are the two main reasons why I enjoyed graduate studies as much as I did and I could not ask for two better people to learn from.

I would like to express my appreciation to my friends and colleagues, and Chai Narendra in particular for his involvement with the development of the spherical SRM code and for preventing the long days of research from becoming dull. I would also like to acknowledge Xiang Li for allowing me to use his iterative Fourier technique code for comparison and validation and Brad Tabachnick for his assistance in the Antennas Laboratory.

I also would like to extend my gratitude to my M.Sc. committee, Dr. Gregory Bridges and Dr. Jason Fiege, for taking the time to evaluate and improve this work.

Lastly, I want to thank the Natural Sciences and Engineering Research Council of Canada and the University of Manitoba GETS program for their financial support.

To Manny

Table of Contents

List of Figures

List of Tables

List of Abbreviations

Abbreviation	Description
ACA	Adaptive cross approximation
AUT	Antenna under test
CG	Conjugate gradient
EFIE	Electric field integral equation
FF	Far-field
FFT	Fast Fourier transform
IFT	Iterative Fourier technique
ME	Modal expansion
MR	Multiplicative regularization
MRE	Maximum radial extent
NF	Near-field
OEW	Open-ended waveguide
PEC	Perfect electric conductor
PMC	Perfect magnetic conductor
PNFR	Planar near-field range
RMS	Root-mean-square
PWS	Plane wave spectrum
RWG	Rao-Wilton-Glisson
SRM	Source reconstruction method
SVD	Singular value decomposition

List of Symbols

Herein we provide some remarks about the notation used in this thesis along with a list of commonly used symbols:

- Vector-valued functions are denoted using an arrow over uppercase or lowercase non-bold letters, such as $\vec{E}\,(\vec{r})$, $\vec{H}\,(\vec{r})$, $\vec{J}\,(\vec{r}\,')$, $\vec{M}\,(\vec{r}\,')$, and $\vec{f}_n\,(\vec{r}\,')$.
- Discrete quantities are denoted using bold font. Matrices are represented by bold uppercase letters, such as $\mathbf{A}_1$, $\mathbf{A}_2$, and $\mathbf{\Sigma}$, while vectors are represented using bold lowercase letters, such as $\mathbf{x}$, $\mathbf{f}$, and $\mathbf{d}$.
- Cost functionals are represented using $\mathcal{C}$ with appropriate subscripts.

Symbol	Description
$\hat{x}, \hat{y}, \hat{z}$	Unit vectors in the x, y, and z directions
$\vec{r}$	Position vector to a general observation point
$\vec{r}\,'$	Position vector to a general source point
j	Imaginary unit ($j^2 = -1$)
D	The reconstruction domain
$\langle \cdot, \cdot \rangle_D$	Inner product defined on D
$\| \cdot \|_D$	L_2-norm defined on D
S	The measurement domain (with subscripts for multiple domains)
$\langle \cdot, \cdot \rangle_S$	Inner product defined on S
$\| \cdot \|_S$	L_2-norm defined on S
$\vec{E}$	Electric field intensity
$\vec{H}$	Magnetic field intensity
$\vec{J}$	Electric current
$\vec{M}$	Magnetic current
k_0	Free space wavenumber
λ	Wavelength in free space
∇	Gradient operator
$\nabla \cdot$	Divergence operator
$\nabla \times$	Curl operator
∇^2	Laplacian operator
x	Unknown equivalent current distributions
$(\cdot)^H$	Hermitian operator
$(\cdot)^*$	Complex conjugate operator

Chapter 1

Introduction

Wireless technologies have become ubiquitous in the world we live in today. Consequently, the need for accurate and useful tools for characterizing antennas and their performance is only increasing. These tools can play a major role in shortening antenna design cycles, improving the quality of validation, and lowering the cost and time required to perform antenna measurements. These potential benefits are of utmost importance for companies looking to gain a competitive edge in the antenna design and manufacturing industries. Antennas are typically characterized by measuring the produced electromagnetic field and processing this data to provide valuable performance metrics and information. To this end, this thesis focuses on the development of such a characterization tool and examines some of the potential benefits and limitations.

1.1 Motivation

To properly design and use an antenna for a specific application (*e.g.* telecommunications, remote sensing, satellite systems), certain properties of the antenna must be known. These properties include gain, radiation efficiency, sidelobe levels, beamwidth, polarization, and most importantly, the far-field (FF) radiation pattern. For this reason, antenna measure-

ments must be performed to determine these quantities, thereby completely characterizing the antenna.

Antenna measurements are typically performed by measuring either the electric or magnetic field produced by an antenna under test (AUT). Measurement techniques are divided into two broad categories based on where the measurements are acquired in relation to the AUT: FF antenna measurements and near-field (NF) antenna measurements. With FF measurement systems, the electric (or equivalently, magnetic) field is sampled at an electrically large distance from the AUT, while NF systems perform measurements at electrically small distances, *e.g.* at 3λ from the AUT where λ denotes the wavelength of operation.

In FF measurement systems, the large separation between the measurement probe and the AUT results in several benefits. The probe is located in the FF or radiation zone of the AUT, meaning that the electromagnetic field observed consists only of radiating energy. Therefore, FF measurements taken in this region will directly provide the radiation pattern of the AUT without the need for extensive post-processing of the measurement data. This being said, the large separation also results in significant drawbacks, most importantly the required measurement system size. With either large AUTs and/or low frequency measurements, the separation required to perform measurements in the FF can become impractically large. For this reason, NF measurement techniques have been developed and researched extensively during the past 40 years.

NF measurement systems[1] are distinct from FF measurement systems in two ways. Firstly, field measurements are performed in the radiating NF regions of the AUT [2]. The NF zone is significantly closer to the AUT than the FF zone, and therefore NF measurement systems are typically much more compact than their FF counterparts. The compact nature of NF systems is also well suited to indoor measurements, allowing for a more controllable

[1]It should be noted that commercial NF systems collect the NF data in three different configurations: (I) on a plane in front of the AUT; (II) on a cylinder around the AUT; and, (III) on a sphere enclosing the AUT. These configurations are referred to as planar, cylindrical, and spherical near-field antenna measurements ranges, respectively.

measurement environment with the use of an anechoic chamber. Secondly, since the radiated field is not measured directly, post-processing is required to determine the FF radiation pattern from the NF measurements. This post-processing is often referred to as a NF to FF (NF-FF) transformation. Consequently, the development of these data processing algorithms is what constitutes most of the recent research in the area of antenna measurements. Last but not least, some NF systems provide a way of keeping the AUT stationary while performing antenna measurements, which is a requirement for certain types of antennas.

Until recently, NF-FF transformation algorithms have used both the amplitude and phase of the measured field data to accurately produce the FF radiation pattern; however, the challenge is that with the recent trend toward antenna operation at higher frequencies, accurately measuring the phase of the field becomes difficult and requires the use of expensive, specialized equipment [3]. Research has shown that eliminating the need to measure phase not only increases the cost-effectiveness of the measurement apparatus but also reduces the detrimental effects of probe positioning errors [4]. The difficulty arises when trying to produce the FF radiation pattern from the amplitude-only field data, as the solution to such a problem is not unique [5]. The desire to overcome these challenges has inspired the development of many phaseless NF-FF transformation techniques, each with their own set of advantages and limitations. Broadly speaking, to handle the lack of phase data, phaseless techniques often collect the amplitude-only data on two measurement domains (*e.g.* two planes) as opposed to one domain (*e.g.* one plane) used in the amplitude and phase approach. It can be intuitively understood that the relation between the amplitude data on the two measurement domains can be implicitly or explicitly used to reconstruct the phase information. Once the reconstructed phase is found it can be used with the measured amplitude data to calculate the FF pattern of the AUT.

1.2 Current Methods

Current NF-FF phaseless transformation algorithms can be classified into two broad categories: (I) phase retrieval techniques and (II) inverse source techniques. Phase retrieval techniques attempt to *directly* recover the phase of the measurement data over one of the measurement domains in a variety of ways. In general, these techniques make use of the Fourier transform to propagate the measured field from one domain to another, or to the FF. The first phase retrieval technique was applied to phaseless NF antenna measurements in [6], in which the amplitude data on measurement domains was propagated to the FF using an iterative application of a Fourier transform operator. The problem was further developed as the minimization of a quadratic cost functional using squared amplitude data [7] using a finite dimensional representation of the measured NF data. Prior information about the system dynamic range, AUT aperture, FF pattern shape, and measurement system accuracy was utilized to improve the phase retrieval accuracy and stability [8]. A phase retrieval algorithm, known as the plane-to-plane method or the iterative Fourier technique (IFT), was developed for bi-polar planar NF antenna measurements[2] using an interpolation scheme for the irregularly sampled field data [10]. Phase retrieval techniques were made more robust by improving the quality of the initial phase guess [11, 12] and including appropriate constraints taking into account the aperture shape of the AUT [13]. Although most phase retrieval development has been for planar NF measurements, the method has been applied to measurements acquired over cylindrical [3, 14] and spherical [15] domains.

Inverse source techniques approach the problem in a slightly different way: rather than use the NF measurements to directly determine the FF pattern (by first retrieving the phase in the phaseless case), these techniques use an intermediate step that first attempts to find a distribution of electric and/or magnetic surface currents that radiate the exact

[2]Planar NF antenna measurement systems typically collect the measurement data over the measurement plane(s) using one of three different grids: (I) rectilinear; (II) polar; and, (III) bi-polar. In addition, a pendulum-based planar NF antenna measurement system has recently been proposed [9].

same electromagnetic field as the AUT. The second and final step of these techniques is to use the equivalent currents to generate the FF pattern of the AUT. This method was originally referred to as the 'equivalent current approach' and was first developed for planar NF measurements with both amplitude and phase data [16] and then extended to arbitrary measurement domains [17]. The equivalent currents were then found over arbitrarily-shaped surfaces [1, 18, 19] and constraints were enforced that resulted in currents that could be used for antenna diagnostics [20, 21]. Within this framework, the use of phaseless measurement data was first applied to the planar measurement case [22] and later to spherical and arbitrary measurement geometries [23, 24]. In recent years the underlying framework has been referred to as the 'source reconstruction method' (SRM), since the 'source' of radiation, the equivalent currents, is to be reconstructed from the measured data. Once this source is reconstructed, the FF of the antenna can be calculated. In this thesis, the focus is on the phaseless SRM.

During the past decade, a phaseless NF-FF transformation technique that shares similarities with both phase retrieval and the SRM has been developed [25, 26, 27]. This technique seeks to optimize a cost functional quantifying the discrepancy between the measured and simulated phaseless data (similar to the SRM), but the field transformations are performed using a Fourier transform (as with many phase retrieval techniques). Contrary to typical SRM the cost functional is not minimized over the equivalent currents, but instead over the expected AUT aperture field using properly selected basis functions with unknown coefficients. The choice of basis functions allows for the incorporation of available prior information about the AUT, which is advantageous when attempting to solve the inverse problem. While this method can be considered state-of-the-art, it is beyond the scope of this work and will not be used as a basis for comparison.

Clearly there has been significant research attention directed towards the development of phaseless NF-FF transformation algorithms. This being said, this is still an active area

of research. The main challenge is that in order to accurately produce the FF pattern, most algorithms require prior information about the AUT, which may not always be available. Additionally, most algorithms also require the user to tune certain parameters that can vary from one measurement to the next. The desire to overcome these challenges is what inspired this work.

1.3 Novelties of this Thesis

To address the challenges concerning the prior information requirements and the parameter tuning, we propose approaching the phaseless NF-FF transformation using the framework of the SRM. The SRM will be implemented for both planar and spherical NF measurement geometries and be able to function with either complex (amplitude and phase) or phaseless NF measurement data. Love's condition will be enforced with the spherical SRM and Schelkunoff's condition will be enforced with the planar SRM to ensure that the reconstructed equivalent currents are representative of the aperture fields.

To overcome the difficulty of selecting appropriate regularization parameters (regularization weights) for each unique measurement, we propose the novel adaptation of a multiplicative regularization (MR) scheme originally developed for inverse scattering applications [28], which results in an automated regularization scheme. We then propose to utilize this MR in conjunction with the SRM as to have a robust and automated algorithm which we refer to as the MR-SRM in this thesis. The mathematical framework for the regularization scheme will be presented in detail along with results from its implementation with the SRM for planar measurements.

1.4 Overview

We begin with an explanation and comparison of the modal expansion (ME) and source reconstruction NF-FF transformation techniques in Chapter 2. The ill-posedness of the inverse problem and the need for regularization are also discussed in this chapter along with the effects of enforcing Love's or Schelkunoff's equivalence conditions. In Chapter 3 we explain how the methods described in Chapter 2 are modified to suit phaseless NF measurements and outline the accompanying challenges. Chapter 4 describes the details of the developed phaseless SRM algorithms for both spherical and planar NF measurements. The MR scheme is introduced in Chapter 5 and the mathematical framework is derived in detail. The developed SRM algorithms are evaluated using synthetic and (in the case of planar measurements) experimental data in Chapter 6. The effect of MR with the planar SRM is shown and compared with results obtained from an implementation of the IFT. Lastly, conclusions and possible future work are presented in Chapter 7.

Chapter 2

NF-FF Techniques

Most antenna characterization concepts (*e.g.* gain, beamwidth, directivity, etc.) rely on the knowledge of the FF pattern. As explained in Section 1.1, directly measuring the FF produced by an antenna can be cumbersome and expensive. Fortunately, there is a fundamental electromagnetic principle that allows us to measure the radiated field much closer to the AUT so as to determine the FF pattern of the antenna. The uniqueness theorem states: "*A field in a lossy region is uniquely specified by the sources within the region plus the tangential components of* $\vec{E}$ *over the boundary, or the tangential components of* $\vec{H}$ *over the boundary, or the former over part of the boundary and the latter over the rest of the boundary*" [29]. This theorem can also be extended to the lossless case by considering the fields to be the limit of the corresponding fields in a lossy medium as the loss goes to zero [29]. In other words, if we *know the source* and measure the tangential electric (or equivalently, magnetic) field on a closed surface around it, the field everywhere is uniquely defined. In the case of NF antenna measurements we do not know the source (the AUT current distribution), and therefore we cannot uniquely determine the field inside the measurement surface. However, the measurement surface also bounds the space on the other side, which happens to be source-free and contain the region that we are interested in

(FF). Therefore the measured tangential fields uniquely define the fields everywhere outside the measurement surface independently from the AUT. This is the concept that makes NF antenna measurements possible. What differentiates various NF-FF transformation techniques is how the measurement data is used to determine the FF, and these differences are substantial as explained in what follows.

2.1 Modal Expansion Techniques

The most established techniques for performing NF-FF transformations rely on the concept of modal expansion (ME): any monochromatic electromagnetic field can be represented by a summation of orthogonal 'modes' in the coordinate system of interest [2]. In the planar case, the orthogonal modes are plane waves with different amplitudes and travelling in different directions. In cylindrical and spherical coordinate systems, the fields can be represented by the superposition of cylindrical and spherical waves, respectively.

The goal of a ME technique is to use the NF measurement data to determine the mode coefficients that represent the field produced by the AUT. This approach has been previously implemented for planar, cylindrical, and spherical NF measurement systems. The planar case is the simplest of the three, and in this case the electric field $\vec{E}$ radiated by the AUT can be expanded as the following superposition of plane waves

$$\vec{E}\,(x,y,z) = \frac{1}{4\pi^2}\int_{-\infty}^{\infty}\int_{-\infty}^{\infty}\vec{F}\,(k_x,k_y)\,e^{-j\vec{k}\cdot\vec{r}}dk_x dk_y \tag{2.1}$$

where $\vec{F}\,(k_x,k_y)$ is the 'plane wave spectrum' (PWS) [2] of the field defined as

$$\vec{F}\,(k_x,k_y) = \hat{x}f_x\,(k_x,k_y) + \hat{y}f_y\,(k_x,k_y) + \hat{z}f_z\,(k_x,k_y) \tag{2.2}$$

where $\hat{x}$, $\hat{y}$, and $\hat{z}$ are the Cartesian unit vectors. The function $\vec{F}\,(k_x,k_y)$ can also be thought

of as the vector amplitude of each plane wave in the summation. The term $\vec{r}$ is a position vector defined as

$$\vec{r} = \hat{x}x + \hat{y}y + \hat{z}z \tag{2.3}$$

and $\vec{k}$ is the propagation factor given by

$$\vec{k} = \hat{x}k_x + \hat{y}k_y + \hat{z}k_z \tag{2.4}$$

and the magnitude of $\vec{k}$ is k_0, the wavenumber in free space. It can be shown that the x and y components of the PWS, f_x and f_y, are related to the x and y components (respectively) of the electric field over an infinite plane at $z = 0$ through the Fourier transforms [2]

$$f_x(k_x, k_y) = \int_{-\infty}^{\infty}\int_{-\infty}^{\infty} E_x\left(x', y', z' = 0\right) e^{j(k_x x' + k_y y')} dx' dy' \tag{2.5}$$

$$f_y(k_x, k_y) = \int_{-\infty}^{\infty}\int_{-\infty}^{\infty} E_y\left(x', y', z' = 0\right) e^{j(k_x x' + k_y y')} dx' dy' \tag{2.6}$$

In other words, if we can measure the x and y components of the electric field over an infinite plane, we can compute the x and y components of the PWS for the field. Obviously we cannot measure the field over an *infinite* plane, but since we are typically dealing with directive antennas with planar measurement systems, we can truncate the measurement plane and assume the field outside the truncated portion is negligible. This simplifies (2.7) and (2.8) to

$$f_x(k_x, k_y) \approx \int_{-a/2}^{a/2}\int_{-b/2}^{b/2} E_x\left(x', y', z' = 0\right) e^{j(k_x x' + k_y y')} dx' dy' \tag{2.7}$$

$$f_y(k_x, k_y) \approx \int_{-a/2}^{a/2}\int_{-b/2}^{b/2} E_y\left(x', y', z' = 0\right) e^{j(k_x x' + k_y y')} dx' dy' \tag{2.8}$$

where a and b are the x and y dimensions of the measurement plane, respectively. Once the x and y components of the PWS are found, they can be related to the electric field in the FF region using the following expressions [2]

$$E_r(r,\theta,\varphi) \simeq 0 \tag{2.9}$$

$$E_\theta(r,\theta,\varphi) \simeq j\frac{k_0 e^{-jk_0 r}}{2\pi r}\left(f_x\cos\varphi + f_y\sin\varphi\right) \tag{2.10}$$

$$E_\varphi(r,\theta,\varphi) \simeq j\frac{k_0 e^{-jk_0 r}}{2\pi r}\cos\theta\left(-f_x\sin\varphi + f_y\cos\varphi\right) \tag{2.11}$$

The expressions in (2.9) through (2.11) are not exact and include approximations that are only accurate for the FF region. More complex expressions can be used to produce the field at locations that are not in the FF, but we do not consider these herein [2].

The same steps can be followed to perform the NF-FF transformation from measurements obtained over a spherical or cylindrical domain [30]. The only difference is in the analytical relationships between the spectrum functions and the field.

2.2 The Source Reconstruction Method

The source reconstruction method (SRM) differs from PWS-based techniques by adding an intermediate step in the NF-FF transformation process. Instead of directly computing the FF pattern from the NF measurements, a set of *equivalent currents* are found that represent the AUT. The FF radiation pattern can then be computed analytically from these currents. The differences in the two techniques are indicated in Figure 2.1.

The SRM is based on the electromagnetic equivalence principle. More specifically, we use the *surface* equivalence principle originally introduced in [31]. To illustrate this principle, we begin with an AUT enclosed by a fictitious surface that we denote as D, typically referred to as the 'reconstruction surface', as shown in Figure 2.2 (a). Note that this surface is not the same as the measurement surface S, and generally D is enclosed by

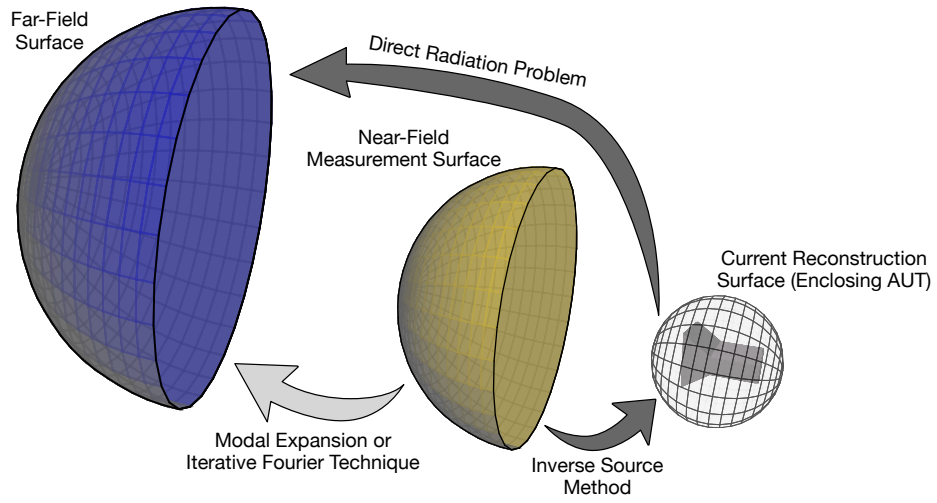

Fig. 2.1: The most common NF-FF transformation techniques. Modal expansion (or PWS) techniques directly compute the FF from the NF measurement data while inverse source (or SRM) techniques add the intermediary step of computing equivalent currents. Figure based on [1].

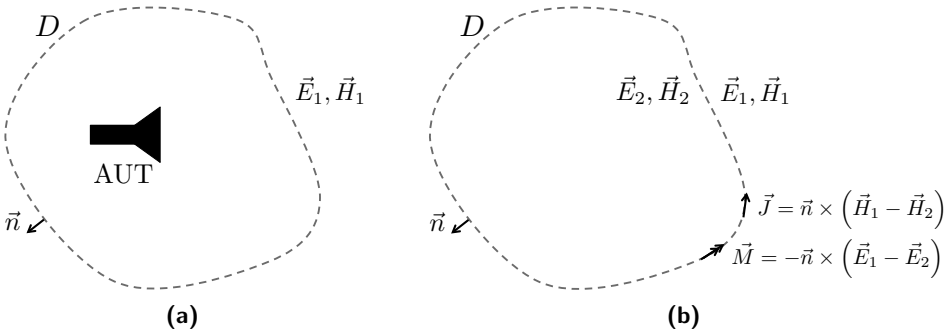

Fig. 2.2: The electromagnetic equivalence principle. The original sources in (a), *i.e.* the AUT, have been replaced by a set of equivalent surface currents $\vec{J}$ and $\vec{M}$ in (b) that produce the exact same fields outside of D.

S. The fields produced by the AUT *everywhere* in space are denoted as $\vec{E}_1$ and $\vec{H}_1$. The surface equivalence principle states that we can construct an equivalent scenario in which the fields outside the surface are the same ($\vec{E}_1$ and $\vec{H}_1$), but with different fields inside the surface, which we call $\vec{E}_2$ and $\vec{H}_2$. To support the discontinuity introduced between the two different fields, sources are required on the surface to satisfy the well-known boundary conditions. This relationship is shown in Figure 2.2 (b). The sources are surface currents ($\vec{J}$ for electric current and $\vec{M}$ for magnetic current) that are related to the difference between the tangential fields on either side of the boundary and are given by

$$\vec{J} = \vec{n} \times \left(\vec{H}_1 - \vec{H}_2 \right) \tag{2.12}$$

$$\vec{M} = -\vec{n} \times \left(\vec{E}_1 - \vec{E}_2 \right) \tag{2.13}$$

where $\vec{n}$ is an outward unit normal vector to D. These surface currents (equivalent currents) will radiate in free space and produce the fields $\vec{E}_1$ and $\vec{H}_1$ outside D and $\vec{E}_2$ and $\vec{H}_2$ inside D.

In the context of NF antenna measurements, we are able to measure the electric field $\vec{E}_1$ on a surface outside D. From this, the SRM attempts to find the surface currents $\vec{J}$ and $\vec{M}$ on D that produce the measured field $\vec{E}_1$ on S. Since we are trying to find the cause from an observed effect, this is an *inverse* problem. It should be noted that, at this point, we are not constraining what the field inside D should be. Therefore any field $\vec{E}_2$ and $\vec{H}_2$ produced by the surface currents is acceptable as long as the same surface currents produce the observed field on S. From this it is clear that there is not a unique solution to the inverse problem and hence the inverse problem is ill-posed [32]. Since in this thesis the SRM will be used to characterize the AUT using phaseless NF data, we now briefly describe some aspects of this algorithm for amplitude and phase NF data. Later in the thesis we will present how the SRM will be used for phaseless NF data.

2.2.1 Forward Problem

In order to solve the inverse problem associated with the SRM we need to model the relationship between the surface currents and the electric field that the currents produce, *i.e.* the forward problem. The relationships between the electric and magnetic currents and the produced electric field are given by the electric field integral equations (EFIE)

$$\vec{E}_J(\vec{r}) = -j\eta k_0 \int_D \left[\vec{J}(\vec{r}\,') + \frac{1}{k_0^2}\,\nabla\nabla'_D \cdot \vec{J}(\vec{r}\,')\right] g_0(\vec{r},\vec{r}\,')d\vec{r}\,' \tag{2.14}$$

$$\vec{E}_M(\vec{r}) = -\nabla \times \int_D \vec{M}(\vec{r}\,')\; g_0(\vec{r},\vec{r}\,')d\vec{r}\,', \tag{2.15}$$

where $\vec{E}_J$ and $\vec{E}_M$ are the electric fields produced by the surface currents $\vec{J}$ and $\vec{M}$, respectively. The integral is performed over the domain D where the currents are located, k_0 is the free space wave number, η is the intrinsic impedance of free space, and $g_0(\vec{r},\vec{r}\,')$ is the free space Green's function given by

$$g_0(\vec{r},\vec{r}\,') = \frac{e^{-jk_0|\vec{r}-\vec{r}\,'|}}{4\pi|\vec{r}-\vec{r}\,'|}. \tag{2.16}$$

In these formulations $\vec{r}$ represents the locations where the field is observed and $\vec{r}\,' \in D$ represents the source locations of the equivalent currents confined to the reconstruction surface. Additionally, dual integral equation expressions exist for the magnetic field and can be used equivalently.

The total electric field is simply a sum of the fields produced by the electric and magnetic currents

$$\vec{E}(\vec{r}) = \vec{E}_J(\vec{r}) + \vec{E}_M(\vec{r}), \tag{2.17}$$

which we can write as

$$\vec{E}(\vec{r}) = \mathcal{A}\left(\vec{J}\left(\vec{r}\,'\right), \vec{M}\left(\vec{r}\,'\right)\right), \tag{2.18}$$

where $\mathcal{A}$ is a linear operator representing the two integral equations (2.14) and (2.15). If we denote the currents $\vec{J}(\vec{r}\,')$ and $\vec{M}(\vec{r}\,')$ collectively as $x(\vec{r}\,')$, then we can further simplify the expression to

$$\vec{E}(\vec{r}) = \mathcal{A}\Big(x\left(\vec{r}\,'\right)\Big). \tag{2.19}$$

The forward problem can then be expressed as follows: for a given x, find $\vec{E}$; however, in the SRM we know $\vec{E}$, and we would like to find x, which is the inverse problem. To solve the inverse problem, we still need to solve the forward problem to evaluate how well the fields associated with a predicted x match the measured data. We now focus on the inverse problem in the next section.

2.2.2 Inverse Problem

Now that we have a mathematical model for the forward problem we can begin to analyze the complexities of solving the inverse problem. The integral equations shown in (2.14) and (2.15) are both Fredholm integral equations of the first kind [33]. A linear inverse problem where the operator is a discretized form of this type of integral equation has been shown to be ill-posed in the sense of Hadamard [34]. An ill-posed problem is defined as one that does not satisfy one or more of the following criteria

1. A solution exists.
2. The solution is unique.
3. The solution depends continuously on the data (system is stable).

In our case, we must sample the electric field at a finite number of observation points over the measurement domain. Because of this, current distributions may exist that produce zero field at the measurement locations, leading to an infinite number of possible solutions and violating the criterion of uniqueness. Evanescent fields may also be produced that cannot be observed at the measurement locations. Additionally, the discretized representation of

the current distributions will not be able to *exactly* produce all possible fields, violating the criterion of existence. Lastly, while the solution to our problem may depend continuously on the data, the operator is typically highly ill-conditioned due to the smoothness of the kernel (Green's function) of the integral equations. The ill-conditioned nature becomes a problem when attempting to solve the system numerically, and impacts the stability from a practical standpoint.

The smoothness of the Green's function is important enough to warrant further discussion. As you move further away from the source (or equivalently the AUT), the Green's function acts as a low-pass filter and 'smooths' out any high spatial variations in the field [34]. This means that the Green's function causes a loss of information about the source, and thus solving the inverse problem (trying to recover the source from the measured data) becomes difficult. Furthermore, since the inverse problem involves the reverse process of the Green's function operator, any high variation components in the measured data will be amplified when finding a solution. Conversely, the smoothness of the Green's function is beneficial when computing the FF radiation pattern once the equivalent currents are found. Any noise of an oscillatory nature (high variation) that is present in the solution will produce fields that will be filtered during the NF-FF transformation. This filtering is more prevalent than that present in the NF operator since the FF pattern is computed at observation locations that are much further away from the source.

The conclusion of the previous discussion is that the SRM problem is inherently ill-posed. We have also noted that the Green's function will 'amplify' any noise present in the measurement data during the inversion process, leading to an unphysical solution. To solve the problem in a stable manner, we must introduce the concept of regularization. The term regularization refers to incorporating added information or constraints in order to select an *appropriate*, stable solution from a set of infinitely many solutions.

There are numerous ways to regularize an ill-posed inverse problem, and the most common way involves balancing the following two L_2-norms

$$\|\mathcal{A}(x) - E\|_S^2 \tag{2.20}$$

$$\|x\|_D^2 \tag{2.21}$$

where E is defined as the 'concatenation' of the two measured tangential field components E_{t1} and E_{t2} (*i.e.* $E_\theta(\vec{r})$ and $E_\varphi(\vec{r})$ for spherical NF measurements) and the spatial dependencies are implied for notational simplicity. The norms in (2.20) and (2.21) are defined as

$$\|E\|_S = \langle E, E\rangle_S^{1/2} \quad \text{and} \quad \langle E_1, E_2\rangle_S = \langle E_{1,t1}, E_{2,t1}\rangle_S + \langle E_{1,t2}, E_{2,t2}\rangle_S \tag{2.22}$$

$$\|x\|_D = \langle x, x\rangle_D^{1/2} \quad \text{and} \quad \langle x_1, x_2\rangle_D = \langle \vec{J}_1, \vec{J}_2\rangle_D + \langle \vec{M}_1, \vec{M}_2\rangle_D. \tag{2.23}$$

The inner products in (2.22) and (2.23) are defined as

$$\langle E_{1,t1}, E_{2,t1}\rangle_S = \int_S E_{1,t1}(\vec{r})\, E_{2,t1}^*(\vec{r})\, d\vec{r} \tag{2.24}$$

$$\langle \vec{J}_1, \vec{J}_2\rangle_D = \int_D \vec{J}_1(\vec{r}) \cdot \vec{J}_2^*(\vec{r})\, d\vec{r}, \tag{2.25}$$

where $*$ denotes the complex conjugate. The first functional, shown in (2.20), quantifies the error between the field observed on S and the field produced on S by the predicted equivalent currents. By minimizing this functional we can find a set of equivalent currents that produce the field that is observed by the measurement system. The second functional, shown in (2.21), is a measure of the 'size' of the solution on the reconstruction domain D. Typically a large solution size is indicative of a non-physical solution due to the inversion of measurement noise, and so finding a solution that minimizes (2.20) while also

keeping (2.21) small is the goal. Tikhonov regularization is performed by minimizing a weighted combination of these two norms

$$\left\| \mathcal{A}(x) - \vec{E} \right\|_S^2 + \gamma^2 \|x\|_D^2 , \tag{2.26}$$

where γ is a regularization parameter that controls the balance between the two norms [34]. If γ is small, we are searching for a solution that satisfies the original problem constraints without placing much emphasis on the physical quality of the solution. If γ is large then we are placing more emphasis on achieving a physically meaningful solution, although in this case the solution may not satisfy the original problem constraints as strictly, or at all. There is a tradeoff that must be made between the two desired outcomes. The optimal value for γ is generally problem specific and finding a suitable value for γ is one of the main reasons that makes solving an ill-posed problem so difficult.

Although there are other regularization techniques, in principle they are all similar to the concepts presented for Tikhonov regularization. One other common technique is the truncated conjugate gradient (CG) procedure, an iterative minimization process in which the number of iterations corresponds to the regularization parameter. Another commonly used regularization technique is a truncated singular value decomposition (SVD) of the operator. Both truncated SVD and CG methods will be discussed in more detail in Chapter 4.

2.2.3 Internal Field Restriction

As discussed in Section 2.2.2, the solution to the inverse problem as posed in (2.19) is not unique. Any combination of sources that produce a null field at the observation points (*i.e.* that is in the null space of the operator) can be added to the solution. In addition, we have not placed any restrictions on the field inside D. Therefore our present formulation allows for the solution to contain sources that radiate zero field external to D and any field inside D that satisfies Maxwell's equations in a source-free homogenous region. Theoretically, a

solution found using this formulation would still result in a suitable NF-FF transformation; however, restricting the field internal to D results in several favorable outcomes. We will discuss the two common restrictions that are used to specify the internal field: Love's equivalence condition or Schelkunoff's equivalence condition.

Love's Equivalence Condition

The most commonly used restriction is to enforce the internal fields to be zero, which is known as Love's equivalence condition [35]. Enforcing the internal field to be zero (*i.e.* the *null* field) simplifies the boundary conditions defining the equivalent currents to

$$\vec{J} = \vec{n} \times \vec{H}_1 \tag{2.27}$$

$$\vec{M} = -\vec{n} \times \vec{E}_1. \tag{2.28}$$

With this condition enforced, the equivalent currents are directly related to the tangential fields $\vec{E}_1$ and $\vec{H}_1$ produced by the original AUT. This is a significant property because $\vec{E}_1$ and $\vec{H}_1$ are not known on D, and the knowledge of the fields in close proximity to the AUT can provide valuable information. Measurement anomalies, defects, interference, and any other measurement issues can quickly be identified if the tangential fields, or equivalently the reconstructed currents, are not as expected. Additionally, enforcing Love's condition has the added benefit of reducing the ill-posedness of the inverse problem by improving the conditioning of the system [36].

Schelkunoff's Equivalence Condition

The second type of internal field restriction is known as Schelkunoff's equivalence condition [31]. This equivalence condition arises from allowing the inner region to be either a perfect electric conductor (PEC) or perfect magnetic conductor (PMC). If the inner region is a PEC, then the electric field in the inner region ($\vec{E}_2$) will be zero. Therefore the bound-

ary condition relating the magnetic current to the electric field is the same as in (2.28). As can be shown using the Lorentz reciprocity theorem [37], any electric surface current on D will not radiate due to the PEC, and thus only $\vec{M}$ must be considered. Similarly, if the inner region is a PMC then the magnetic field in the inner region ($\vec{H}_2$) will be zero, and the boundary condition for $\vec{J}$ will be the same as (2.27). It can also be shown that any magnetic current tangential to a PMC will not radiate, and therefore in this case only $\vec{J}$ must be considered.

In both variations of Schelkunoff's equivalence condition (either PEC or PMC), the corresponding surface current (either $\vec{M}$ or $\vec{J}$, respectively) will radiate in the *presence of the conductor*. This is typically problematic since the Green's function needed to compute the forward operators is no longer the Green's function of free space. In general, this new Green's function is not known analytically and would be extremely computationally expensive to compute. This being said, when the measurement and reconstruction surfaces are planar this limitation can be avoided entirely using image theory. The theory behind this simplification and its implementation with the planar SRM will be discussed in more detail in Section 4.3.

It is important to note that the equivalent currents in both variations of Schelkunoff's equivalence condition are also directly related to the fields just outside of the reconstruction surface. This indicates that the currents resulting from Schelkunoff's condition also have the advantageous property of providing information that can be used for antenna diagnostics.

2.3 NF-FF Method Comparison

While both ME and SRM are able to perform NF-FF transformations, there are some important differences between the two methods. First of all, the SRM adds the intermediary step of finding the equivalent currents while the ME methods directly compute the FF pattern from the NF data. In general, this results in the SRM requiring more computational

time than ME to compute the same NF-FF transformation [38]. This being said, taking the time to generate the equivalent currents does have benefits. If Love's or Schelkunoff's conditions are enforced, the equivalent currents are directly related to the fields on the reconstruction surface. The currents can then be examined and provide information that is extremely useful for antenna diagnostics and the detection of defects.

ME methods also rely on the use of the Fourier transform. While these methods do not require measurements to be acquired over a canonical domain, they do require interpolation schemes that can produce a set of NF data over a uniform set of points [26]. On the other hand, the SRM can work with *arbitrary* measurement geometries, without the need for interpolation. The measurement domain does not need to be fully closed (*i.e.* partial sphere) and the measurement of the different tangential field components do not need to be co-located. Additionally, the reconstruction surfaces used in SRM can also be of arbitrary shape, and can be made conformal to the AUT [1]. A conformal reconstruction surface would result in equivalent currents that nearly represent the *physical* currents on the actual AUT, and would be very useful for antenna design as well as the design of feeding structures and radomes [39].

Lastly, ME methods need to assume field values at locations on the canonical surfaces where measurement data are not available (*e.g.* assuming the field is zero outside of the finite measurement plane for planar NF measurements). These assumptions necessarily introduce a source of error into the NF-FF transformation process, the degree of which depends on the accuracy of the assumption. This is in contrast to the SRM that does not require any such assumptions of the unknown field values.

Chapter 3

Phaseless NF-FF Techniques

Historically, NF-FF transformation methods have required accurate amplitude *and* phase measurements of the NF electric field in order to produce a reliable FF radiation pattern. However, the phase information can become difficult (and expensive) to measure at high frequencies, and these measurements can also be corrupted by probe positioning errors[1] and phase drift [4]. For these reasons there is an interest in the development of new NF-FF transformation techniques that only require phaseless (amplitude-only) measurement data.

3.1 Phase Retrieval Methods

The first class of phaseless NF-FF transformation techniques are based on some form of *phase retrieval*. This involves attempting to directly produce the phase of the measured data from amplitude-only measurements over one or more measurement domains. Once the phase information is recovered, standard NF-FF transformation techniques can be used with the amplitude data and recovered phase to produce the FF radiation pattern. This class of techniques is quite broad, but in this work we focus on the most established phase

[1] Probe positioning errors are defined as the difference between the expected and actual location of the measurement probe, typically caused by uncertainties and tolerances in the mechanical positioning system.

retrieval method for comparison with the SRM algorithms being developed. This method is commonly referred to as the iterative Fourier technique (IFT) or the plane-to-plane method [10]. In general, this method is based on an iterative application of the ME technique outlined in Section 2.1.

More specifically, the IFT is a technique in which the phase of the measured electric field is recovered in an iterative fashion. This method requires at least two measurement domains of phaseless electric field data, and an initial guess for the phase distribution over one of the domains. Then, using the ME procedures described in Section 2.1, the field, along with the phase guess, is propagated to the second measurement domain. The amplitude of the propagated field is replaced with the amplitude that was measured on the second domain while keeping the calculated phase, and then the field is propagated back to the first measurement domain. If the amplitude of the propagated field is close enough to the measured amplitude on the first plane, the iterative procedure is stopped. Otherwise, the phase of the propagated field is used as the new guess and the entire procedure is repeated. Typically two measurement domains are needed to accurately recover the phase, although one measurement domain can be used if two different probes are used to perform the measurements [40]. Regardless, two *non-redundant* sets of measurement data are required.

The main challenge with the IFT is finding a suitable initial phase estimate that allows for the iterative process to converge to a physical solution. Overcoming this challenge typically requires some prior knowledge about the AUT, such as the shape of the aperture and the direction of the main beam. One of the most recent developments on this technique finds an initial phase estimate by employing the differential evolution algorithm, a global optimization technique [12]. Most IFT methods also enforce constraints on the aperture field distribution, based on knowledge of the expected aperture fields [10].

As with any method that relies on the use of the Fourier transform, the IFT requires interpolation of the measured data if not acquired uniformly over canonical measurement

surfaces. The IFT is especially suitable for planar NF measurements, since the plane-to-plane propagation can take advantage of the discrete fast Fourier transform (FFT) and the implementation becomes very computationally efficient [13]. The IFT has also recently been applied to spherical NF phaseless measurements [15].

3.2 Source Reconstruction Methods

Phaseless NF-FF techniques based on the SRM are formulated in nearly the same way as their amplitude-and-phase counterparts. Since we are now working with amplitude-only measurement data, the cost functional in (2.20) is no longer suitable. For this reason, we must modify the functional to relate the difference in the electric field amplitudes measured and produced by the equivalent currents on the measurement domain. Moreover, using the difference between the *squared* amplitudes is preferred for two reasons:

1. The squared amplitude is directly related to the power of the electromagnetic field and can be easily measured using inexpensive equipment such as a power meter.

2. Using the squared amplitude leads to a quadratic cost functional while using the amplitude itself leads to more highly nonlinear operators that are more difficult to invert [7].

The modified cost functional becomes

$$\left\| |\mathcal{A}(x)|^2 - |E|^2 \right\|_S^2, \tag{3.1}$$

where $|\cdot|$ denotes taking the amplitude of *each tangential component* of the complex-valued fields (not to be confused with the spatial magnitude found by combining the separate field components). To overcome the loss of information from the lack of phase data, phaseless SRM methods typically use two sets of measured amplitude-only data, similar to approach

used with phase retrieval techniques. This results in two cost functionals

$$\left\| |\mathcal{A}_1(x)|^2 - |E_1|^2 \right\|_{S_1}^2 \tag{3.2}$$

$$\left\| |\mathcal{A}_2(x)|^2 - |E_2|^2 \right\|_{S_2}^2 \tag{3.3}$$

that are simultaneously minimized to solve for the unknown currents $x(\vec{r}')$ (S_1 and S_2 denote the two measurement domains). These cost functionals are nonlinear (as opposed to the linear functional in the case of amplitude-and-phase SRM as shown in (2.20)), and the way these functionals are minimized differs from method to method. In the simplest case the sum of (3.2) and (3.3) is minimized using the conjugate gradient method, as shown in Section 4.2 with the spherical phaseless SRM implementation. A more advanced method is discussed in Chapter 5.

Recently a phaseless SRM technique has been developed that differs from the general framework described above. The technique iteratively applies the amplitude-and-phase SRM in an iterative fashion with the goal of improving a phase estimate at each step [24]. This method is completely analogous to the IFT, except that the SRM is used to perform the plane-to-plane propagation instead of ME. To the best of our knowledge the method has not been evaluated with added noise or with scanned beam antennas.

As with the amplitude-and-phase SRM, appropriate regularization schemes must be employed and can often present a challenge. Most developed SRM methods require the *ad-hoc* selection of certain regularization parameters that strongly depend on the specifics of problem at hand [23, 24]. This will result in *not* having an automated phaseless NF-FF transformation algorithm.

3.3 Phaseless NF-FF Challenges

While there has been a great deal of research towards developing accurate and efficient phaseless NF-FF transformation algorithms, there are still many practical challenges that have yet to be fully overcome. Limitations of the phase retrieval methods include a heavy reliance on the quality of the initial phase guess and the requirement of interpolation for non-uniform/non-canonical measurements. The quality of the initial phase guess becomes even more important when considering scanned beam antennas [41]. With the SRM, the choice of regularization scheme and the associated regularization parameters are the main limitations offsetting the advantages gained by obtaining the equivalent currents.

For these reasons the aim of this work is to develop a phaseless SRM technique that overcomes the problem of regularization parameter selection and removes the guesswork for the user.

Chapter 4

Development of a Phaseless SRM Algorithm

In this section the discretization procedure and numerical considerations are described for implementing the SRM for both spherical and planar measurement geometries. We describe the SRM for spherical measurements first because of its generality, followed by the planar case which uses some simplifications. In both cases we first describe the appropriate SRM formulation as applied to amplitude and phase data, followed by an extension to the phaseless case.

4.1 Spherical Measurements

In a spherical NF antenna measurement system, the electric field is sampled, rather obviously, over a spherical surface. These systems measure the θ and φ components of $\vec{E}$ at a finite number of locations over the measurement domain, hence discretizing the measurement surface S. The required sampling resolution for spherical NF antenna measurements is provided in [42].

The reconstruction surface D is then discretized into triangular surface elements, or a

surface mesh. The size of the triangular elements are constrained so that no edge is longer than $\lambda/10$, which is common in source reconstruction implementations [18, 36]. Next, we must select appropriate basis functions that will be used to expand the equivalent current distributions $\vec{J}(\vec{r}\,')$ and $\vec{M}(\vec{r}\,')$ over each triangular element. The two most commonly used basis functions are pulse and Rao-Wilton-Glisson (RWG). While a pulse basis is simpler and more easily implemented, it does not enforce continuity in the surface current from element to element. On the other hand, the RWG basis was specifically created with continuity in mind. The tangential fields (represented by the surface currents) on D should be continuous, hence the RWG basis enables us to limit the possible solutions to those that exhibit the desired continuity across element boundaries.

The equivalent currents can be expanded using the piece-wise linear RWG basis [43] as

$$\vec{J}(\vec{r}\,') = \sum_{n=1}^{N} x_n^J \vec{f}_n(\vec{r}\,') \qquad \vec{M}(\vec{r}\,') = \sum_{n=1}^{N} x_n^M \vec{f}_n(\vec{r}\,') \tag{4.1}$$

where x_n^J and x_n^M are complex expansion coefficients corresponding to the n^{th} unique edge of the surface (2D) mesh. An edge is defined as one of the three lines bounding each triangular element. Edges that are only part of one element are known as boundary edges, and the presence of such edges indicates that the mesh is not closed[1]. The non-boundary edges will be shared by two elements, and a mesh with X elements will have at most $3X/2$ unique non-boundary edges. In (4.1) N is the number of *non-boundary* edges, and therefore this basis does not allow current to travel over a boundary edge and violate continuity. The

[1]The framework developed *does* function for meshes that are not closed, but an analysis on the use of such reconstruction surfaces with the SRM for spherical NF measurements is beyond the scope of this work.

RWG vector basis function $\vec{f}_n(\vec{r}\,')$ is defined for each edge as

$$\vec{f}_n(\vec{r}\,') = \begin{cases} \frac{l_n}{2A_n^+}\vec{\rho}_n^{\,+}, & \vec{r}\,' \text{ in } T_n^+ \\ \frac{l_n}{2A_n^-}\vec{\rho}_n^{\,-}, & \vec{r}\,' \text{ in } T_n^- \\ 0, & \text{otherwise} \end{cases} \tag{4.2}$$

where where l_n is the length of the n^{th} edge, $A_n^{\pm}$ is the area of the positive/negative element, and $T_n^{\pm}$ refers to the positive/negative element associated with each edge. Each non-boundary edge will separate two elements, one of which is arbitrarily referred to as the 'positive' element and the other is referred to as the 'negative' element. The position vector $\vec{\rho}_n^{\,+}$ or $\vec{\rho}_n^{\,-}$ determines the direction of the basis function based on whether $\vec{r}\,'$ is in the positive or negative element associated with the n^{th} edge. The vector $\vec{\rho}_n^{\,+}$ is defined as the vector from the free vertex (opposite the edge) to $\vec{r}\,'$, while $\vec{\rho}_n^{\,-}$ is defined as the vector from $\vec{r}\,'$ to the free vertex. With this basis, it can easily be shown that continuity of the *normal* component (with respect to each edge) of the current is required. In other words, the basis only supports distributions in which the current leaving an element is the same as the current entering the adjacent elements. A further discussion on the use of RWG basis functions can be found in [18].

Now that we have a method of discretely representing the current distributions, we need a way to evaluate the integral equations in (2.14) and (2.15). The divergence, gradient, and curl operators can all be computed analytically via the dyadic Green's function [44]. The integration is performed numerically by using openly available symmetric Gaussian quadrature rules for triangular elements [45]. We typically employ a 5^{th} order, 7-point rule, although the developed code can support higher order rules if more accuracy is desired. An adaptive integration scheme could also be implemented to minimize the numerical integration error as well. Now we are able to construct the discrete matrix representation of

the forward problem which allows us to compute the electric field at the observation points produced by the current distribution. Our current distributions are now uniquely represented by two sets, or vectors, of complex expansion coefficients $\mathbf{x}^J$ and $\mathbf{x}^M$. The θ and φ components of the produced electric field at the observation locations are represented as the vectors $\mathbf{E}_\theta$ and $\mathbf{E}_\varphi$, which are concatenated into the vector $\mathbf{E}$. The relationship between the expansion coefficients and the field is directly provided through the use of the RWG basis functions and the numerical integration of (2.14) and (2.15). This allows us to compute operators that map the expansion coefficients to the field produced at the measurement locations as

$$\begin{bmatrix} \mathbf{A}_{J,S} & \mathbf{A}_{M,S} \end{bmatrix} \begin{bmatrix} \mathbf{x}^J \\ \mathbf{x}^M \end{bmatrix} = \begin{bmatrix} \mathbf{E} \end{bmatrix}. \tag{4.3}$$

We now enforce Love's equivalence condition to ensure that the reconstructed surface currents are directly related to the true fields on D. We generate a surface that is a slightly recessed copy of D and we denote this new surface as S' and the volume bounded by it as V'. The uniqueness theorem can be used to show that [29]

$$\vec{n} \times \vec{E}(\vec{r}) = 0, \quad \vec{r} \in S' \implies \vec{E}(\vec{r}) = \vec{H}(\vec{r}) = 0, \quad \vec{r} \in V'. \tag{4.4}$$

Therefore if we enforce that the tangential electric field produced by the equivalent currents is zero on S', then the fields in V' will necessarily be zero as well. We can achieve this approximately by generating operators, similar to those in (4.3), that produce the tangential $\vec{E}$ on S' from the equivalent currents at a finite number of points. We will denote these operators as $\mathbf{A}_{J,S'}$ and $\mathbf{A}_{M,S'}$, and we can write

$$\mathbf{A}_{J,S'}\mathbf{x}^J + \mathbf{A}_{M,S'}\mathbf{x}^M = \mathbf{0}. \tag{4.5}$$

Combining (4.3) and (4.5) we get

$$\begin{bmatrix} \mathbf{A}_{J,S} & \mathbf{A}_{M,S} \\ \mathbf{A}_{J,S'} & \mathbf{A}_{M,S'} \end{bmatrix} \begin{bmatrix} \mathbf{x}^J \\ \mathbf{x}^M \end{bmatrix} = \begin{bmatrix} \mathbf{E} \\ \mathbf{0} \end{bmatrix}. \tag{4.6}$$

This is the inverse problem that will be solved in the case of spherical measurements. To simplify the notation, we will combine the S and S' operators resulting in

$$\begin{bmatrix} \mathbf{A}_J & \mathbf{A}_M \end{bmatrix} \begin{bmatrix} \mathbf{x}^J \\ \mathbf{x}^M \end{bmatrix} = \begin{bmatrix} \mathbf{E}' \end{bmatrix} \tag{4.7}$$

where $\mathbf{E}'$ is the concatenation of $\mathbf{E}$ and $\mathbf{0}$. The length of the zero vector $\mathbf{0}$ is $2N'$ (the factor of two is because the tangential field must be represented by two components), where N' is the number of points at which the electric field is enforced to be zero on S'. In general we oversample and ensure that $N' > N$ because of the point-matching method employed [20].

Since the electric and magnetic currents contribute to the radiated electric field in different ways (see (2.14) and (2.15)), the operator in (4.7) will be poorly scaled. This is overcome by normalizing each of the two matrices $\mathbf{A}_J$ and $\mathbf{A}_M$ using the procedure first described in [1]. The two operators are scaled as

$$\overline{\mathbf{A}}_J = \frac{1}{\mathrm{RMS}\left(\mathbf{A}_J\right)} \mathbf{A}_J \tag{4.8}$$

$$\overline{\mathbf{A}}_M = \frac{1}{\mathrm{RMS}\left(\mathbf{A}_M\right)} \mathbf{A}_M, \tag{4.9}$$

where the RMS value of an m by n complex matrix $\mathbf{P}$ is defined as:

$$\mathrm{RMS} = \sqrt{\frac{\sum_{i=1}^{m} \sum_{j=1}^{n} |\mathbf{P}(i,j)|^2}{mn}}. \tag{4.10}$$

The RMS value of $\mathbf{A}_J$ will typically be about 377 times larger than the RMS value of $\mathbf{A}_M$, and this ratio can generally be approximated by the intrinsic impedance of free space η. Although this approximation becomes worse as the distance between S and D decreases, many SRM implementations avoid calculating the RMS values and use η as the scaling factor [36, 24]. In our case, we now formulate the normalized inverse problem as

$$\begin{bmatrix} \overline{\mathbf{A}}_J & \overline{\mathbf{A}}_M \end{bmatrix} \begin{bmatrix} \overline{\mathbf{x}}^J \\ \overline{\mathbf{x}}^M \end{bmatrix} = \begin{bmatrix} \mathbf{E}' \end{bmatrix}, \tag{4.11}$$

where $\overline{\mathbf{x}}^J$ and $\overline{\mathbf{x}}^M$ indicate that the unknowns found from this equation will differ from the unknowns in (4.7) because of the scaling factors. Once the problem is solved, the scaling factors must be factored out of the solution to produce $\mathbf{x}^J$ and $\mathbf{x}^M$. We further simplify the notation by letting

$$\mathbf{A} = \begin{bmatrix} \overline{\mathbf{A}}_J & \overline{\mathbf{A}}_M \end{bmatrix}, \quad \mathbf{x} = \begin{bmatrix} \overline{\mathbf{x}}^J \\ \overline{\mathbf{x}}^M \end{bmatrix}, \quad \mathbf{f} = \begin{bmatrix} \mathbf{E}' \end{bmatrix} \tag{4.12}$$

and finally we can write

$$\mathbf{A}\mathbf{x} = \mathbf{f}. \tag{4.13}$$

Given that $\mathbf{f}$ and $\mathbf{A}$ are known quantities, we would like to invert $\mathbf{A}$ to find the solution of expansion coefficients $\mathbf{x}$. Direct inversion of $\mathbf{A}$ is not possible because: (i) $\mathbf{A}$ is typically either over- or under-determined; and (II) $\mathbf{A}$ is highly ill-conditioned and therefore non-invertible. Finding a solution to (4.13) is generally not straightforward and requires some consideration in selecting an appropriate method.

4.1.1 Operator Characteristics

We will now take a deeper look at the characteristics of the discrete operator $\mathbf{A}$ from (4.13) using an economic singular value decomposition (SVD). We can decompose the rectangular matrix $\mathbf{A}$ into

$$\mathbf{A} = \mathbf{U}\boldsymbol{\Sigma}\mathbf{V}^H, \tag{4.14}$$

where $\mathbf{U}$ and $\mathbf{V}$ are matrices of left and right singular (column) vectors, respectively, $\boldsymbol{\Sigma}$ is a diagonal matrix with the singular values of $\mathbf{A}$ on the diagonal, and the superscript H denotes the Hermitian operator. Since this is an economic SVD, $\boldsymbol{\Sigma}$ is a square matrix with dimensions equal to the smallest dimension of $\mathbf{A}$, which we will denote as P. Thus, we have P singular values σ_i of $\mathbf{A}$ where $i = \{1, 2, \cdots, P\}$. Substituting (4.14) into (4.13) produces

$$\mathbf{U}\boldsymbol{\Sigma}\mathbf{V}^H\mathbf{x} = \mathbf{f}. \tag{4.15}$$

Since $\mathbf{U}$ is a unitary matrix, we have

$$\boldsymbol{\Sigma}\mathbf{V}^H\mathbf{x} = \mathbf{U}^H\mathbf{f}. \tag{4.16}$$

Since Σ is a diagonal matrix (with singular values guaranteed to be non-zero [34]) and $\mathbf{V}$ is also unitary, we can write

$$\mathbf{x} = \mathbf{V}\ \text{diag}\left(\frac{1}{\sigma_i}\right)\mathbf{U}^H\mathbf{f}, \tag{4.17}$$

where $\text{diag}\left(\frac{1}{\sigma_i}\right)$ is a diagonal matrix with a diagonal elements equal to $\frac{1}{\sigma_i}$. If we denote the i^{th} columns of $\mathbf{U}$ and $\mathbf{V}$ as $\mathbf{u}_i$ and $\mathbf{v}_i$, respectively, we can instead write the product in (4.17) as a summation

$$\mathbf{x} = \sum_i^P \frac{\mathbf{u}_i^H\mathbf{f}}{\sigma_i}\mathbf{v}_i. \tag{4.18}$$

It is now evident that the desired solution $\mathbf{x}$ will be a summation of right singular vectors with coefficients equal to

$$\beta_i = \frac{\mathbf{u}_i^H \mathbf{f}}{\sigma_i}. \tag{4.19}$$

In this formulation we will assume that the summation is ordered such that as i increases, σ_i decreases monotonically.

We now expand the measured data vector $\mathbf{f}$ into

$$\mathbf{f} = \overline{\mathbf{f}} + \mathbf{e}, \tag{4.20}$$

where $\overline{\mathbf{f}}$ is the exact measured data and $\mathbf{e}$ represents the error present in the measurement data (noise, interference, etc.). We can now rewrite (4.18) as

$$\mathbf{x} = \sum_i^P \left[\frac{\mathbf{u}_i^H \overline{\mathbf{f}}}{\sigma_i} \mathbf{v}_i + \frac{\mathbf{u}_i^H \mathbf{e}}{\sigma_i} \mathbf{v}_i \right]. \tag{4.21}$$

Since we are dealing with an operator formed from discretizing a Fredholm integral equation of the first kind, the singular values will decay gradually to zero [34]. In (4.21), we have two terms with σ_i in the denominator that must be analyzed. The first term contains the exact measured data $\overline{\mathbf{f}}$, and the discrete Picard condition states that the magnitude of $\mathbf{u}_i^H \overline{\mathbf{f}}$ will decay at a faster rate than the singular values σ_i [46] and therefore this term does not pose a problem. The problem arises in the second term, where the numerator is not guaranteed to decay faster than the singular values. This causes this term to become extremely large as i increases and results in a non-physical solution.

To overcome this problem we need to introduce some form of regularization, as mentioned earlier in Section 2.2.2. The obvious choice would be to use a truncated SVD expansion of $\mathbf{A}$, in which the solution is computed using (4.18) with the summation truncated once the singular values fall below a certain threshold [47]. This regularization technique

has been used in SRM applications [18], but the process of computing the SVD of $\mathbf{A}$ is very computationally expensive and becomes impractical for larger problems.

4.1.2 Conjugate Gradient Method

In this work we will use the conjugate gradient (CG) method for least-squares problems, which is a Krylov subspace regularization technique [48]. CG is an iterative method that uses derivative based optimization to repeatedly update a solution until some convergence criterion is met. It has been shown that the solution iterate at the k^{th} CG iteration belongs to an approximation of the subspace formed by the first k singular vectors, and therefore truncating the CG iterations has the same regularizing effect as using a truncated SVD procedure [34]. The main benefits of using CG Krylov subspace regularization as compared to the truncated SVD are: (I) its significantly less computational complexity; and, (II) the fact that it does not require explicit storage of the matrix operator. We apply the CG method to solve the least-squares problem

$$\mathbf{A}^H\mathbf{A}\mathbf{x} = \mathbf{A}^H\mathbf{f}, \tag{4.22}$$

or equivalently the minimization of the functional [48]

$$\mathcal{C}(\mathbf{x}) = \left\|\mathbf{A}\mathbf{x} - \mathbf{f}\right\|_S^2. \tag{4.23}$$

The steps of the CG technique will now be described as shown in [48]. We begin with an initial guess for the solution which we denote as $\mathbf{x}_{(0)}$. We denote the residual at the k^{th} iteration as

$$\mathbf{r}_{(k)} = \mathbf{A}\mathbf{x}_{(k)} - \mathbf{f}. \tag{4.24}$$

The initial search direction is defined as

$$\mathbf{d}_{(0)} = \mathbf{A}^H \mathbf{r}_{(0)}. \tag{4.25}$$

At each iteration, the step length in the search direction is found as

$$\alpha_{(k)} = \frac{\mathbf{d}_{(k)}^H \mathbf{d}_{(k)}}{(\mathbf{A}\mathbf{d}_{(k)})^H \mathbf{A}\mathbf{d}_{(k)}}. \tag{4.26}$$

The solution is then updated according to

$$\mathbf{x}_{(k+1)} = \mathbf{x}_{(k)} + \alpha_{(k)} \mathbf{d}_{(k)}, \tag{4.27}$$

and the residual is updated as well, given by

$$\mathbf{r}_{(k+1)} = \mathbf{r}_{(k)} - \alpha_{(k)} \mathbf{A}\mathbf{d}_{(k)}. \tag{4.28}$$

We then check if the stopping criterion is met, specified as

$$\text{if} \quad \frac{\left\|\mathbf{x}_{(k+1)} - \mathbf{x}_k\right\|_D}{\left\|\mathbf{x}_{k+1}\right\|_D} < \text{tol, then stop.} \tag{4.29}$$

This stopping criterion ends the iterative process once the solution begins to 'stagnate', *i.e.* not change significantly between two iterations. If the criterion is not met, compute the new search direction vector as

$$\mathbf{d}_{(k+1)} = \mathbf{A}^H \mathbf{r}_{(k+1)} + \beta_{(k+1)} \mathbf{d}_{(k)}, \tag{4.30}$$

where $\beta_{(k+1)}$ is the Polak-Ribière weighting factor [49] defined as

$$\beta_{(k+1)} = \frac{\left(\mathbf{A}^H\mathbf{r}_{(k+1)} - \mathbf{A}^H\mathbf{r}_{(k)}\right)^H \mathbf{A}^H\mathbf{r}_{(k+1)}}{\left(\mathbf{A}^H\mathbf{r}_{(k)}\right)^H \mathbf{A}^H\mathbf{r}_{(k)}}. \tag{4.31}$$

Other options for the search direction at each iteration are available, such as the Fletcher-Reeves formulation [50], but in our experience the Polak-Ribière choice has resulted in the most stability. Using the new search direction in (4.30) the process is repeated until the condition in (4.29) is reached or a maximum number of iterations have been completed.

Regularization Parameter Selection

In general, selecting an appropriate tolerance value is difficult and requires some knowledge of the problem. In addition, the residual error shown in (4.24) does not always indicate the quality of the solution. The CG process causes the residual error to decrease monotonically, but similar to truncated SVD regularization, in later iterations the system noise may begin to contribute significantly to the reconstruction. During these iterations, CG finds a solution that can more accurately produce the field *and* the noise on the measurement domain. Since the noise typically contains high spatial frequency components, the solution begins to develop extremely high variations of an unphysical nature in order to be able to produce the measurement noise. This causes the residual error to decrease at the expense of the solution quality and FF accuracy. This phenomenon can be observed by plotting how the size of the solution (given by $\|\mathbf{x}\|_D$) changes with respect to the residual error over the CG iterations. This type of plot is known as an L-curve, and a visual example can be found in [51].

As the residual error decreases, the solution size increases. After a certain point, known as the 'knee point' of the curve, the solution size increases massively with relatively little decrease in the residual error. This is the area of under-regularized solutions which we would

like to avoid, and thus the goal is to truncate the iterations prior to this point; however, early truncation leads to an over-regularized solution which we would also like to avoid. In this work we have observed that the stopping criterion in (4.29) performs well with a tolerance on the order of 10^{-3} to 10^{-4}, but in general a method such as the L-curve should be used to ensure robustness.

4.1.3 FF Computation

A solution found using CG results in a set of complex RWG edge coefficients. These coefficients define the electric and magnetic currents on the reconstruction surface through the relation defined in (4.1). Since we enforced Love's condition, these currents are directly related to the tangential fields on the reconstruction surface and can be used for diagnostic purposes.

Additionally, we want to produce the FF radiation pattern from the equivalent currents. To accomplish this we build another matrix operator $\mathbf{A}_{FF}$ that maps the edge coefficients to the electric (or magnetic, or both) field at the desired FF observation locations. This operator is built in exactly the same way as the NF operator, except Love's condition is excluded. Once the operator is computed, the FF pattern can be computed using a simple matrix-vector product (or forward solve)

$$\mathbf{f}_{FF} = \mathbf{A}_{FF}\mathbf{x}. \tag{4.32}$$

In fact, an operator can be constructed that produces the fields at *any* locations outside of the reconstruction surface if desired.

4.2 Phaseless Spherical Measurements

In the phaseless case, we will have two sets of amplitude-only measurement data acquired over spherical surfaces. We will denote these two measurement domains as S_1 and S_2. Two NF operators are built in the same way as the operator in (4.13), resulting in a system of two matrix equations that relates surface currents in $\mathbf{x}$ to field measurements $\mathbf{f}_1$ and $\mathbf{f}_2$ (both amplitude and phase) on the two surfaces respectively

$$\mathbf{A}_1\mathbf{x} = \mathbf{f}_1 \tag{4.33}$$

$$\mathbf{A}_2\mathbf{x} = \mathbf{f}_2. \tag{4.34}$$

We only measure the amplitude of $\mathbf{f}_1$ and $\mathbf{f}_2$, and thus we construct the cost functional for the phaseless problem as

$$\mathcal{C}(\mathbf{x}) = \mathcal{C}_1(\mathbf{x}) + \mathcal{C}_2(\mathbf{x}), \tag{4.35}$$

where $\mathcal{C}_1(\mathbf{x})$ and $\mathcal{C}_2(\mathbf{x})$ represent the normalized error in the squared field amplitude on each of the two measurement domains, calculated as

$$\mathcal{C}_1(\mathbf{x}) = \eta_1 \left\| |\mathbf{A}_1\mathbf{x}|^2 - |\mathbf{f}_1|^2 \right\|_{S_1}^2 \tag{4.36}$$

$$\mathcal{C}_2(\mathbf{x}) = \eta_2 \left\| |\mathbf{A}_2\mathbf{x}|^2 - |\mathbf{f}_2|^2 \right\|_{S_2}^2, \tag{4.37}$$

where the $|\cdot|^2$ operator represents taking the squared amplitude in an *element-wise* fashion of the discrete vector. The terms η_1 and η_2 are normalization factors introduced to equalize the contributions of $\mathcal{C}_1(\mathbf{x})$ and $\mathcal{C}_2(\mathbf{x})$ to the overall cost functional. The normalization

factors can be computed using

$$\eta_1 = \left\| |\mathbf{f}_1|^2 \right\|_{S_1}^{-2} \tag{4.38}$$

$$\eta_2 = \left\| |\mathbf{f}_2|^2 \right\|_{S_2}^{-2}. \tag{4.39}$$

To minimize the *nonlinear* functional in (4.35) with respect to $\mathbf{x}$, we again use the conjugate gradient method. Since we have modified the cost functional, the gradient of (4.35) must be derived.

4.2.1 Phaseless Spherical Gradient Derivation

The derivation of the gradient of (4.35) will be performed in the continuous domain and then the considerations for the discrete case will be explained. The norm and inner products over D are defined in (2.23) and the norm and inner products over the measurement surfaces are defined in (2.22). In the continuous domain the cost functional is

$$\mathcal{C}(x) = \mathcal{C}_1(x) + \mathcal{C}_2(x), \tag{4.40}$$

where the data error terms $\mathcal{C}_1(x)$ and $\mathcal{C}_2(x)$ are given as

$$\mathcal{C}_1(x) = \eta_1 \left\| |\mathcal{A}_1 x|^2 - |E_1|^2 \right\|_{S_1}^2 \tag{4.41}$$

$$\mathcal{C}_2(x) = \eta_2 \left\| |\mathcal{A}_2 x|^2 - |E_2|^2 \right\|_{S_2}^2 \tag{4.42}$$

and are completely analogous to their discrete counterparts in (4.35) to (4.37). Our goal is to optimize $\mathcal{C}(x)$ over x, but this means optimizing a real-valued functional over a complex quantity. The challenge arises from the fact that any real-valued functional is not analytic in the complex domain, and therefore is not complex differentiable [52]. To deal with this difficulty we can treat the complex function x and its complex conjugate x^* as *indepen-*

dent quantities over which the minimization is performed. This method has been used in similar applications including microwave tomography [53, 54], and makes use of Wirtinger calculus [55].

We will start by finding the first variation of $\mathcal{C}_1(x)$, *i.e.* the derivative of $\mathcal{C}_1(x)$ with respect to x when x is slightly varied by some function ψ (which has the same form as x).

$$\begin{aligned}\partial\mathcal{C}_1 &= \lim_{\epsilon\to 0}\frac{\mathcal{C}_1(x+\epsilon\psi)-\mathcal{C}_1(x)}{\epsilon}\\ &= \lim_{\epsilon\to 0}\frac{\eta_1\left\|\left|\mathcal{A}_1(x+\epsilon\psi)\right|^2-\left|E_1\right|^2\right\|_{S_1}^2-\eta_1\left\|\left|\mathcal{A}_1x\right|^2-\left|E_1\right|^2\right\|_{S_1}^2}{\epsilon}.\end{aligned} \tag{4.43}$$

If we denote the residual for each measurement domain as

$$R_i = \left|\mathcal{A}_i x\right|^2-\left|E_i\right|^2,\quad i=\{1,2\}, \tag{4.44}$$

then (4.43) simplifies to[2]

$$\begin{aligned}\partial\mathcal{C}_1 &= \lim_{\epsilon\to 0}\frac{\eta_1\left\|\left|\mathcal{A}_1(x+\epsilon\psi)\right|^2-\left|E_1\right|^2\right\|_{S_1}^2-\eta_1\left\|R_1\right\|_{S_1}^2}{\epsilon}\\ &= \lim_{\epsilon\to 0}\frac{\eta_1\left\|\left(\mathcal{A}_1x+\epsilon\mathcal{A}_1\psi\right)\left(\mathcal{A}_1x+\epsilon\mathcal{A}_1\psi\right)^*-\left|E_1\right|^2\right\|_{S_1}^2-\eta_1\left\|R_1\right\|_{S_1}^2}{\epsilon}\\ &= \lim_{\epsilon\to 0}\frac{\eta_1\left\|\left|\mathcal{A}_1x\right|^2-\left|E_1\right|^2+\epsilon^2\left|\mathcal{A}_1\psi\right|^2+2\epsilon\mathrm{Re}\left[\left(\mathcal{A}_1\psi\right)\left(\mathcal{A}_1x\right)^*\right]\right\|_{S_1}^2-\eta_1\left\|R_1\right\|_{S_1}^2}{\epsilon}\\ &= \lim_{\epsilon\to 0}\frac{\eta_1\left\|R_1+\epsilon^2\left|\mathcal{A}_1\psi\right|^2+2\epsilon\mathrm{Re}\left[\left(\mathcal{A}_1\psi\right)\left(\mathcal{A}_1x\right)^*\right]\right\|_{S_1}^2-\eta_1\left\|R_1\right\|_{S_1}^2}{\epsilon}.\end{aligned} \tag{4.45}$$

[2]Computing the term $(\mathcal{A}_1\psi)(\mathcal{A}_1x)^*$ (and similar products) requires some clarification concerning the notation. Multiplication of two terms of the same 'concatenated' form as E_1 or E_2 is performed as follows: multiply the individual tangential components (*i.e.* $E_{1,t1}$ or $E_{1,t2}$) together separately, and then concatenate the results such that the product is of the same form as the two factors.

Using the definition of the norm and inner product in (2.22), we can expand (4.45) as

$$\begin{aligned}
\partial\mathcal{C}_1 &= \lim_{\epsilon\to 0}\frac{1}{\epsilon}\Bigg[\eta_1\langle R_1 + \epsilon^2\left|\mathcal{A}_1\psi\right|^2 + 2\epsilon\mathrm{Re}\Big[\left(\mathcal{A}_1\psi\right)\left(\mathcal{A}_1 x\right)^*\Big], R_1 \\
&\qquad + \epsilon^2\left|\mathcal{A}_1\psi\right|^2 + 2\epsilon\mathrm{Re}\Big[\left(\mathcal{A}_1\psi\right)\left(\mathcal{A}_1 x\right)^*\Big]\rangle_{S_1} - \eta_1\left\|R_1\right\|_{S_1}^2\Bigg] \\
&= \lim_{\epsilon\to 0}\frac{\eta_1}{\epsilon}\Bigg[\left\|R_1\right\|_{S_1}^2 + \Big\|\epsilon^2\left|\mathcal{A}_1\psi\right|^2 + 2\epsilon\mathrm{Re}\Big[\left(\mathcal{A}_1\psi\right)\left(\mathcal{A}_1 x\right)^*\Big]\Big\|_{S_1}^2 \\
&\qquad + 2\mathrm{Re}\langle R_1, \epsilon^2\left|\mathcal{A}_1\psi\right|^2 + 2\epsilon\mathrm{Re}\Big[\left(\mathcal{A}_1\psi\right)\left(\mathcal{A}_1 x\right)^*\Big]\rangle_{S_1} - \left\|R_1\right\|_{S_1}^2\Bigg] \\
&= \lim_{\epsilon\to 0}\frac{\eta_1}{\epsilon}\Bigg[\Big\|\epsilon^2\left|\mathcal{A}_1\psi\right|^2 + 2\epsilon\mathrm{Re}\Big[\left(\mathcal{A}_1\psi\right)\left(\mathcal{A}_1 x\right)^*\Big]\Big\|_{S_1}^2 \\
&\qquad + 2\mathrm{Re}\langle R_1, \epsilon^2\left|\mathcal{A}_1\psi\right|^2 + 2\epsilon\mathrm{Re}\Big[\left(\mathcal{A}_1\psi\right)\left(\mathcal{A}_1 x\right)^*\Big]\rangle_{S_1}\Bigg]. \qquad (4.46)
\end{aligned}$$

Evaluating the limit results in

$$\begin{aligned}
\partial\mathcal{C}_1 &= 2\eta_1\mathrm{Re}\langle R_1, 2\mathrm{Re}\Big[\left(\mathcal{A}_1\psi\right)\left(\mathcal{A}_1 x\right)^*\Big]\rangle_{S_1} \\
&= 4\eta_1\mathrm{Re}\langle R_1, \left(\mathcal{A}_1\psi\right)\left(\mathcal{A}_1 x\right)^*\rangle_{S_1} \\
&= 4\eta_1\mathrm{Re}\langle R_1\mathcal{A}_1 x, \mathcal{A}_1\psi\rangle_{S_1} \\
&= 4\eta_1\mathrm{Re}\langle \mathcal{A}_1^a R_1\mathcal{A}_1 x, \psi\rangle_D \\
&= 2\eta_1\mathrm{Re}\langle \mathcal{A}_1^a R_1\mathcal{A}_1 x, \psi\rangle_D, \qquad (4.47)
\end{aligned}$$

and this expression can be expanded to

$$\partial\mathcal{C}_1 = \langle\left[2\eta_1\mathcal{A}_1^a R_1\mathcal{A}_1 x\right]^*, \psi^*\rangle_D + \langle 2\eta_1\mathcal{A}_1^a R_1\mathcal{A}_1 x, \psi\rangle_D. \qquad (4.48)$$

At this point we consider the cost functional $\tilde{\mathcal{C}}_1\left(x, x^*\right)$ such that $\tilde{\mathcal{C}}_1\left(x, x^*\right) = \mathcal{C}_1\left(x\right)$. Using

Wirtinger calculus, we can write the first variation of $\mathcal{C}_1$ as

$$\partial\mathcal{C}_1 = \frac{\partial\tilde{\mathcal{C}}_1}{\partial x}(\psi) + \frac{\partial\tilde{\mathcal{C}}_1}{\partial x^*}(\psi^*), \tag{4.49}$$

where the following equality holds

$$\frac{\partial\tilde{\mathcal{C}}_1}{\partial x}(\psi) = \left[\frac{\partial\tilde{\mathcal{C}}_1}{\partial x^*}(\psi^*)\right]^*. \tag{4.50}$$

From (4.48), (4.49), and (4.50), we can see that

$$\frac{\partial\tilde{\mathcal{C}}_1}{\partial x}(\psi) = \langle[2\eta_1\mathcal{A}_1^a R_1\mathcal{A}_1 x]^*, \psi^*\rangle_D \tag{4.51}$$

$$\frac{\partial\tilde{\mathcal{C}}_1}{\partial x^*}(\psi^*) = \langle 2\eta_1\mathcal{A}_1^a R_1\mathcal{A}_1 x, \psi\rangle_D, \tag{4.52}$$

and therefore the discretized gradient operator [56, 57] (evaluated at $\mathbf{x}_{(k)}$) that we desire will be of the form

$$\mathbf{g}_1 = 2\eta_1\mathbf{A}_1^H\mathbf{r}_{1,(k)} \odot \mathbf{A}_1\mathbf{x}_{(k)}. \tag{4.53}$$

Similarly, the gradient operator for $\mathcal{C}_2$ is

$$\mathbf{g}_2 = 2\eta_2\mathbf{A}_2^H\mathbf{r}_{2,(k)} \odot \mathbf{A}_2\mathbf{x}_{(k)}, \tag{4.54}$$

where $\odot$ denotes a Hadamard (elementwise) product and the residuals $\mathbf{r}_{1,(k)}$ and $\mathbf{r}_{2,(k)}$ are defined as

$$\mathbf{r}_{1,(k)} = \left|\mathbf{A}_1\mathbf{x}_{(k)}\right|^2 - |\mathbf{f}_1|^2 \tag{4.55}$$

$$\mathbf{r}_{2,(k)} = \left|\mathbf{A}_2\mathbf{x}_{(k)}\right|^2 - |\mathbf{f}_2|^2. \tag{4.56}$$

Therefore the gradient of $\mathcal{C}(\mathbf{x})$ evaluated at $\mathbf{x}_{(k)}$ is given by

$$\mathbf{g}_{(k)} = 2\eta_1 \mathbf{A}_1^H \Big(\mathbf{r}_{1,(k)} \odot \big(\mathbf{A}_1 \mathbf{x}_{(k)} \big) \Big) + 2\eta_2 \mathbf{A}_2^H \Big(\mathbf{r}_{2,(k)} \odot \big(\mathbf{A}_2 \mathbf{x}_{(k)} \big) \Big). \tag{4.57}$$

The search direction $\mathbf{d}_{(k)}$ at each iteration is a combination of the gradient at the current and previous iterations, given by the Polak-Ribière expression

$$\mathbf{d}_{(k)} = \mathbf{g}_{(k)} + \frac{\big(\mathbf{g}_{(k)} - \mathbf{g}_{(k-1)} \big)^H \mathbf{g}_{(k)}}{\mathbf{g}_{(k-1)}^H \mathbf{g}_{(k-1)}}. \tag{4.58}$$

4.2.2 Finding the Step Length

Once the search direction is computed, the step length $\alpha_{(k)}$ is found by minimizing

$$\mathcal{C}\left(\mathbf{x}_{(k)} + \alpha_{(k)} \mathbf{d}_{(k)} \right) \tag{4.59}$$

with respect to $\alpha_{(k)}$. In other words, $\alpha_{(k)}$ is explicitly equal to

$$\alpha_{(k)} = \arg\min_{\alpha} \mathcal{C}\left(\mathbf{x}_{(k)} + \alpha_{(k)} \mathbf{d}_{(k)} \right). \tag{4.60}$$

To accomplish this we start with an expression for $\mathcal{C}\left(\mathbf{x}_{(k)} + \alpha_{(k)} \mathbf{d}_{(k)} \right)$

$$\mathcal{C}(\mathbf{x} + \alpha \mathbf{d}) = \mathcal{C}_1(\mathbf{x} + \alpha \mathbf{d}) + \mathcal{C}_2(\mathbf{x} + \alpha \mathbf{d}) \tag{4.61}$$

where the (k) subscripts have been dropped for simplicity. We first expand $\mathcal{C}_1(\mathbf{x}+\alpha\mathbf{d})$ as

$$\begin{aligned}\mathcal{C}_1(\mathbf{x}+\alpha\mathbf{d}) &= \Big\| |\mathbf{A}_1(\mathbf{x}+\alpha\mathbf{d})|^2 - |\mathbf{f}|^2 \Big\|_{S_1}^2 \\ &= \Big\| (\mathbf{A}_1\mathbf{x}+\alpha\mathbf{A}_1\mathbf{d}) \odot (\mathbf{A}_1\mathbf{x}+\alpha\mathbf{A}_1\mathbf{d})^* - |\mathbf{f}|^2 \Big\|_{S_1}^2 \\ &= \Big\| |\mathbf{A}_1\mathbf{x}|^2 + \alpha^2 |\mathbf{A}_1\mathbf{d}|^2 + \alpha\Big[(\mathbf{A}_1\mathbf{x}) \odot (\mathbf{A}_1\mathbf{d})^* + (\mathbf{A}_1\mathbf{x})^* \odot (\mathbf{A}_1\mathbf{d}) \Big] - |\mathbf{f}|^2 \Big\|_{S_1}^2 \\ &= \Big\| \mathbf{r}_1 + \alpha^2 |\mathbf{A}_1\mathbf{d}|^2 + 2\alpha \mathrm{Re}\Big[(\mathbf{A}_1\mathbf{x}) \odot (\mathbf{A}_1\mathbf{d})^* \Big] \Big\|_{S_1}^2 . \end{aligned} \tag{4.62}$$

To simplify (4.62) further, we use the following

$$\begin{aligned}\|\mathbf{p}+\mathbf{q}+\mathbf{s}\|^2 &= \langle \mathbf{p}+\mathbf{q}+\mathbf{s}, \mathbf{p}+\mathbf{q}+\mathbf{s} \rangle \\ &= \|\mathbf{p}\|^2 + \|\mathbf{q}\|^2 + \|\mathbf{s}\|^2 + 2\mathrm{Re}\langle \mathbf{p},\mathbf{q}\rangle + 2\mathrm{Re}\langle \mathbf{q},\mathbf{s}\rangle + 2\mathrm{Re}\langle \mathbf{p},\mathbf{s}\rangle. \end{aligned} \tag{4.63}$$

The expression in (4.62) then becomes a fourth-degree polynomial in alpha

$$\begin{aligned}\mathcal{C}_1(\mathbf{x}+\alpha\mathbf{d}) = \alpha^4 \Big\| |\mathbf{A}_1\mathbf{d}|^2 \Big\|_{S_1}^2 &+ 4\alpha^3 \mathrm{Re}\langle |\mathbf{A}_1\mathbf{d}|^2, (\mathbf{A}_1\mathbf{x}) \odot (\mathbf{A}_1\mathbf{d})^* \rangle_{S_1} \\ &+ 2\alpha^2 \Big[\mathrm{Re}\langle \mathbf{r}_1, |\mathbf{A}_1\mathbf{d}|^2 \rangle_{S_1} + \Big\| \mathrm{Re}\big((\mathbf{A}_1\mathbf{x}) \odot (\mathbf{A}_1\mathbf{d})^* \big) \Big\|_{S_1}^2 \Big] \\ &+ 4\alpha \mathrm{Re}\langle \mathbf{r}_1, (\mathbf{A}_1\mathbf{x}) \odot (\mathbf{A}_1\mathbf{d})^* \rangle_{S_1} + \|\mathbf{r}_1\|_{S_1}^2 . \end{aligned} \tag{4.64}$$

In a similar fashion, $\mathcal{C}_2(\mathbf{x}+\alpha\mathbf{d})$ can be written as

$$\begin{aligned}\mathcal{C}_2(\mathbf{x}+\alpha\mathbf{d}) = \alpha^4 \Big\| |\mathbf{A}_2\mathbf{d}|^2 \Big\|_{S_2}^2 &+ 4\alpha^3 \mathrm{Re}\langle |\mathbf{A}_2\mathbf{d}|^2, (\mathbf{A}_2\mathbf{x}) \odot (\mathbf{A}_2\mathbf{d})^* \rangle_{S_2} \\ &+ 2\alpha^2 \Big[\mathrm{Re}\langle \mathbf{r}_2, |\mathbf{A}_2\mathbf{d}|^2 \rangle_{S_2} + \Big\| \mathrm{Re}\big((\mathbf{A}_2\mathbf{x}) \odot (\mathbf{A}_2\mathbf{d})^* \big) \Big\|_{S_2}^2 \Big] \\ &+ 4\alpha \mathrm{Re}\langle \mathbf{r}_2, (\mathbf{A}_2\mathbf{x}) \odot (\mathbf{A}_2\mathbf{d})^* \rangle_{S_2} + \|\mathbf{r}_2\|_{S_2}^2 . \end{aligned} \tag{4.65}$$

Adding (4.64) and (4.65) and differentiating results in a third-degree polynomial in α. The roots of this polynomial expression are found numerically, resulting in a pair of complex

conjugate roots and one real root. The step length is then taken to be the real root. Once the step length is determined, the solution is updated in the same way as the amplitude-and-phase case using (4.27). The iterations are truncated once the condition in (4.29) is reached or the maximum number of iterations have been completed.

4.3 Planar Measurements

In a planar measurement system, the electric field is measured over a planar grid, typically with uniformly spaced points and rectangular in shape. A simple schematic of a typical planar measurement setup is shown in Figure 4.1. The two measurement planes S_1 and

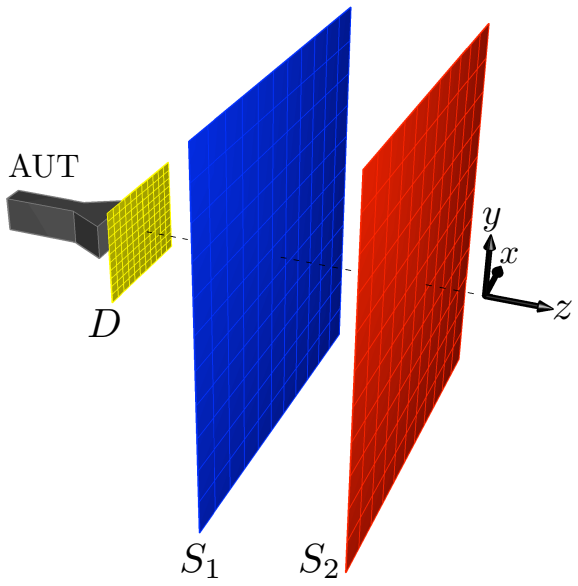

Fig. 4.1: A typical planar NF measurement setup. The x and y components of the electric (or magnetic) field are sampled over a uniform planar domains S_1 and S_2. The reconstruction surface is denoted as D.

S_2 shown are only necessary for phaseless measurements, which will be described in more detail in Section 4.3.1. For amplitude-and-phase measurements, only one measurement plane is required for an accurate NF-FF transformation. On these measurement planes the

tangential electric field is measured, *i.e.* E_x and E_y.

With the planar measurement configurations, a few simplifications can be introduced. We first let the reconstruction surface D be an infinite plane slightly in front of the aperture of the AUT, as shown in Figure 4.2. This infinite plane divides the space into two regions:

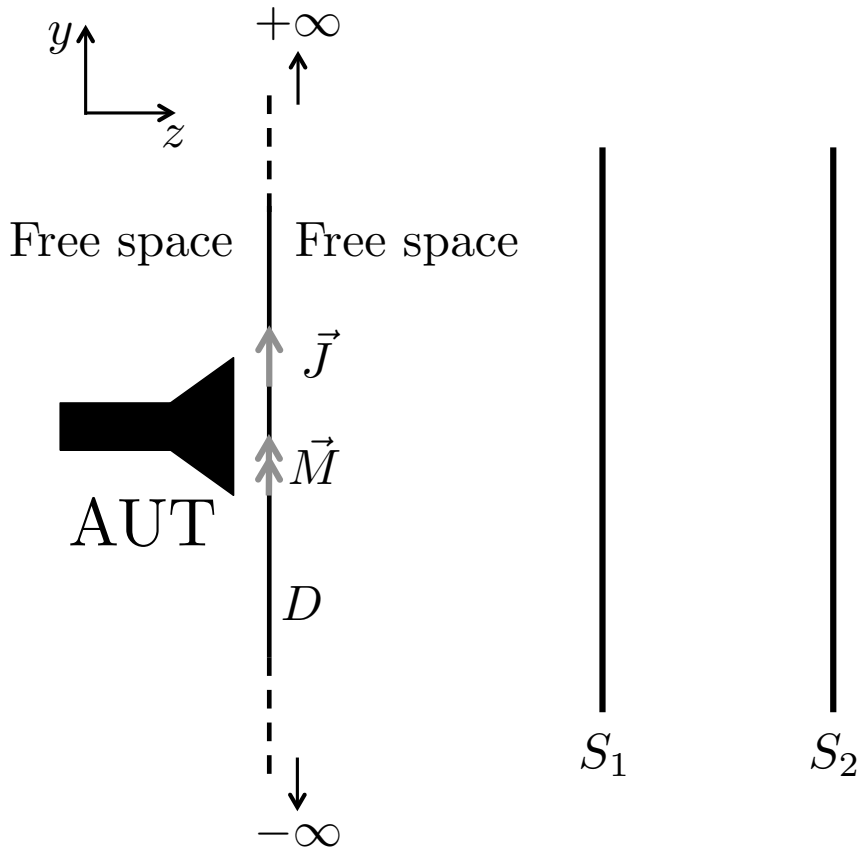

Fig. 4.2: The reconstruction surface D and measurement surfaces S_1 and S_2 in relation to the AUT. Note that the surface currents $\vec{J}$ and $\vec{M}$ are *equivalent* to the AUT in terms of their radiation to the right of the infinite plane.

one that contains the AUT (the 'inner' region) and one that contains the measurement planes (the 'outer' region). The aim is to find a set of equivalent currents that radiate the same field as the AUT in the outer region, and for this reason we can impose any restriction on the field in the inner region. Instead of enforcing Love's condition, we enforce

that the inner region should behave as a PEC, *i.e.* Schelkunoff's equivalence condition. Using the reciprocity theorem it can be shown that any electric current next to a PEC will not radiate [29], and therefore we are left with only the equivalent magnetic current $\vec{M}$ as shown in Figure 4.3. Currently $\vec{M}$ would radiate next to a PEC into the outer region consisting of free space. In this state we would need to find the Green's function for this configuration, but this can be avoided by employing another simplification. Image theory states that $\vec{M}$ radiating next to an infinite PEC is equivalent to $2\vec{M}$ radiating in free space when we are only concerned about the outer (free space) region [29]. This allows us to use the well-known free space Green's function to compute the radiation integrals needed to model the forward problem. It is important to note that although we have made several simplifications thus far, we have *not* made any approximations. Until this point, each step has been equivalent to the initial problem in Figure 4.2.

With these simplifications in place, the electric field integral equations shown in (2.14) and (2.15) become

$$\vec{E}(\vec{r}) = -2\,\nabla \times \int_D \vec{M}(\vec{r}\,')\; g_0(\vec{r},\vec{r}\,')d\vec{r}\,'. \tag{4.66}$$

Since we are not concerned with any z components of $\vec{E}$ or $\vec{M}$, (4.66) can be decoupled into two scalar equations

$$E_x(\vec{r}) = 2\int_D M_y(\vec{r}\,')\frac{\partial g_0(\vec{r},\vec{r}\,')}{\partial z'}d\vec{r}\,' \tag{4.67}$$

$$E_y(\vec{r}) = -2\int_D M_x(\vec{r}\,')\frac{\partial g_0(\vec{r},\vec{r}\,')}{\partial z'}d\vec{r}\,'. \tag{4.68}$$

In the present state D is infinite plane, which is not possible to realize physically. To overcome this practical limitation we truncate D so that it is slightly larger than the aperture of the AUT. Since planar measurement systems are typically used for directive antennas, the electric field, and therefore equivalent magnetic current, on the truncated portion of the plane will be negligible. For this reason the excluded part of the integrals in (4.67)

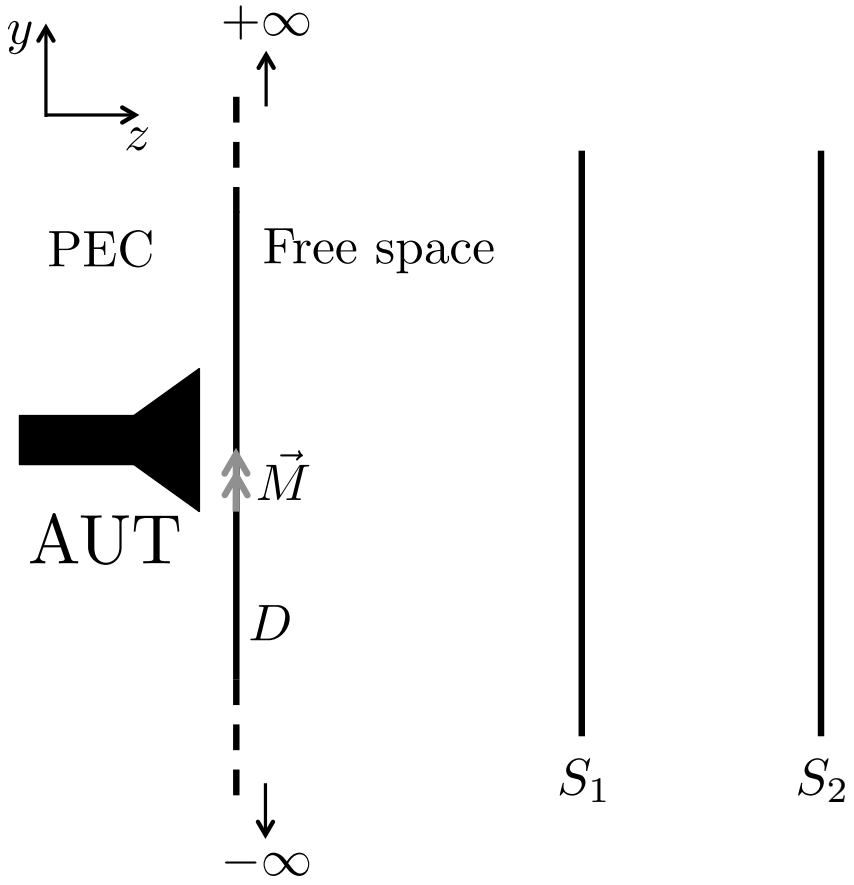

Fig. 4.3: A scenario equivalent to Figure 4.2. The effect of the electric equivalent current has been negated by the presence of the PEC.

and (4.68) result in minimal error. These equations represent the forward problem and are what we discretize to create an operator that relates the equivalent current to the measured electric field.

The reconstruction surface D is discretized into uniform square elements of side length $\lambda/10$. To represent the x and y components of the equivalent current on the reconstruction surface we use pulse basis functions

$$\vec{M}(\vec{r}\,') = \sum_{n=1}^{N} \left(x_{n,x}^{M} \hat{x} + x_{n,y}^{M} \hat{y} \right) f_n(\vec{r}\,'), \tag{4.69}$$

where $x_{n,x}^{M}$ and $x_{n,y}^{M}$ are complex expansion coefficients corresponding to the x and y components of the magnetic current, respectively, and $f_n(\vec{r}\,')$ is the pulse basis function associated with the n^{th} element, defined as

$$f_n(\vec{r}\,') = \begin{cases} 1, & \vec{r}\,' \text{ in } T_n \\ 0, & \text{otherwise} \end{cases} \tag{4.70}$$

where T_n refers to the n^{th} element. Although the pulse basis does not enforce continuity, it is used for the planar SRM to facilitate the addition of multiplicative regularization that will be discussed in Chapter 5. Discretizing equations (4.67) and (4.68), we are able to write the linear integral equations as a matrix equation

$$\begin{bmatrix} \mathbf{A}_{yx} & \mathbf{0} \\ \mathbf{0} & \mathbf{A}_{xy} \end{bmatrix} \begin{bmatrix} \mathbf{x}_x^M \\ \mathbf{x}_y^M \end{bmatrix} = \begin{bmatrix} \mathbf{E}_y \\ \mathbf{E}_x \end{bmatrix}. \tag{4.71}$$

The submatrices $\mathbf{A}_{yx}$ and $\mathbf{A}_{xy}$ are the discrete forms of (4.68) and (4.67), respectively. The vectors $\mathbf{E}_x$ and $\mathbf{E}_y$ contain the measured electric field as sampled on the measurement

plane. This matrix equation can then be written in a simpler form as

$$\mathbf{A}\mathbf{x} = \mathbf{f}. \tag{4.72}$$

It is important to note that because of the decoupled nature of the integral equations, *half* of the elements in $\mathbf{A}$ will be zero. Any operations that involve $\mathbf{A}$ (*i.e.* matrix-vector products, Hadamard products, Hermitian, etc.) have been implemented in an efficient way to take advantage of this property. This system is then solved using the CG scheme outlined in detail in Section 4.1.2. Once the inverse problem is solved, the pulse basis coefficients can then be used to generate the FF using a matrix operator produced in a similar way to $\mathbf{A}$.

4.3.1 Phaseless Planar Measurements

When phase information is not available, a NF-FF transformation can still be performed if amplitude measurements over two (or more) measurement planes is available. Two operators are formed in the same way as that in (4.72), resulting in

$$\mathbf{A}_1\mathbf{x} = \mathbf{f}_1 \tag{4.73}$$

$$\mathbf{A}_2\mathbf{x} = \mathbf{f}_2. \tag{4.74}$$

In this case we use the same cost functional as the spherical case (4.35), and the minimization is also performed in the same way.

Chapter 5

Multiplicatively Regularized SRM

As mentioned in Section 4.1.2, selecting an appropriate regularization constant, or equivalently the number of CG iterations, typically requires some knowledge of the problem and can be difficult. Some common methods used for selecting an appropriate amount of regularization include the previously mentioned L-curve method and generalized cross-validation [58], but these methods can become computationally expensive for some problems. Such methods have also been designed to be used with linear ill-posed problems, and are not necessarily appropriate for nonlinear ill-posed problems such as the use of phaseless NF antenna measurements to reconstruct equivalent currents [59]. To avoid this limitation, we adapt a multiplicative regularization (MR) scheme originally developed for inverse scattering [28] and image deblurring [60] to the source reconstruction problem. The modified scheme is developed for planar NF measurements only due to the complexity of the implementation for other measurement geometries, but to the best of our knowledge the scheme could be extended to other geometries in the future. As will be seen, the three main advantages of the utilized MR are as follows: (I) it provides an automated way to determine the regularization weight during the inversion process; (II) it provides the so-called adaptive regularization which is beneficial for nonlinear ill-posed problems [59]; and, (III) it

simultaneously provides Laplacian regularization, which is useful for suppressing spurious oscillations in the reconstructed current, and edge preserving regularization, which is useful for the detection of defects in the AUT.

5.1 Modified Cost Functional

Multiplicative regularization is introduced by modifying the cost-functional shown in (4.35) to include a term referred to as a multiplicative regularizer. The formulation presented here has been modified from that presented in [60] and extended in [61]. The modified cost functional is

$$\mathcal{C}\left(\mathbf{x}\right) = \Big(\mathcal{C}_1\left(\mathbf{x}\right) + \mathcal{C}_2\left(\mathbf{x}\right)\Big)\mathcal{C}_{\mathrm{MR}}\left(\mathbf{x}\right), \tag{5.1}$$

where $\mathcal{C}_{\mathrm{MR}}\left(\mathbf{x}\right)$ is the multiplicative regularizer defined as a weighted L_2-norm

$$\mathcal{C}_{\mathrm{MR}}\left(\mathbf{x}\right) = \int_D \mathbf{b}^2(\vec{r}\,') \left(\left|\nabla \mathbf{x}\left(\vec{r}\,'\right)\right|^2 + \delta^2\right) d\vec{r}\,'. \tag{5.2}$$

The purpose of the multiplicative regularizer is to penalize solutions that are undesirable—what exactly is meant by 'undesirable' will be discussed shortly—thereby favouring a certain set of appropriate solutions. In (5.2), $\mathbf{b}(\vec{r}\,')$ is a positive weighting function and δ is a positive steering parameter. The exact form of these terms will be shown in detail in the following section.

Before discussing the minimization of (5.1), it is important to emphasize the reason for introducing a multiplicative constraint. While an additive regularizer (such as the Tikhonov regularizer in (2.26)) requires an additional regularization weighting parameter, the multiplicative regularizer is weighted by the sum of the error terms $\mathcal{C}_1\left(\mathbf{x}\right)$ and $\mathcal{C}_2\left(\mathbf{x}\right)$. If the data error is large, the regularization term is weighted more heavily by definition. As the solution estimate becomes closer to the true solution, the data error decreases and the amount of

regularization is decreased automatically. As noted above, this inherent ability is known as adaptive regularization [62, 63], which is provided here in an automated fashion, thus removing the difficult task of selecting an appropriate regularization weight at each step of the iterative minimization process. As an added benefit, the multiplicative regularizer in (5.2) has been shown to have 'edge-preserving' characteristics as well as Laplacian regularization characteristics that should result in an improved equivalent current reconstruction [64].

5.2 Conjugate Gradient Minimization

As with the previous methods, we use the CG method to minimize the cost functional in (5.1). This method requires us to find an update $\mathbf{x}_{(n+1)}$ from the previous estimate of the solution $\mathbf{x}_{(n)}$ during the n^{th} CG iteration. To formulate the update expression, we need to compute the gradient $\mathbf{g}_{(n)}$ of (5.1) required during the n^{th} CG iteration, evaluated at $\mathbf{x}_{(n)}$. To accomplish this we need the gradients of each of the three terms in (5.1).

5.2.1 Finding the Gradient of the Cost Functional

We begin by finding the gradient of $\mathcal{C}_{\mathrm{MR}}(\mathbf{x})$ evaluated at $\mathbf{x}_{(n)}$, which we denote as $\mathbf{g}_{MR,(n)}$. Since we need the gradient evaluated at $\mathbf{x}_{(n)}$, we start with an expression for $\mathcal{C}_{\mathrm{MR}}(\mathbf{x})$ evaluated at $\mathbf{x}_{(n)}$

$$\mathcal{C}_{\mathrm{MR}}\left(\mathbf{x}_{(n)}\right) = \int_D \mathbf{b}^2_{(n)}(\vec{r}\,') \left(\left| \nabla \mathbf{x}_{(n)}\left(\vec{r}\,'\right) \right|^2 + \delta^2_{(n)} \right) d\vec{r}\,'. \tag{5.3}$$

We now define $\mathbf{b}_{(n)}(\vec{r}\,')$ explicitly as

$$\mathbf{b}_{(n)}(\vec{r}\,') = A^{-\frac{1}{2}} \left(\left| \nabla \mathbf{x}_{(n)}\left(\vec{r}\,'\right) \right|^2 + \delta^2_{(n)} \right)^{-\frac{1}{2}}, \tag{5.4}$$

where A is the total area of the reconstruction plane D. At this point, it is important to notice that this specific choice for $\mathbf{b}_{(n)}(\vec{r}\,')$ results in $\mathcal{C}_{\mathrm{MR}}\left(\mathbf{x}_{(n)}\right) \equiv 1$. This is beneficial because it removes the need to compute $\mathcal{C}_{\mathrm{MR}}\left(\mathbf{x}_{(n)}\right)$ during each CG iteration. We then define the steering parameter $\delta^2_{(n)}$ as

$$\delta^2_{(n)} = \frac{\mathcal{C}_1\left(\mathbf{x}_{(n)}\right) + \mathcal{C}_2\left(\mathbf{x}_{(n)}\right)}{2\Delta x \Delta y}, \tag{5.5}$$

where Δx and Δy are the dimensions of each square element on D. The gradient of (5.3) can be derived as [53]

$$\mathbf{g}_{\mathrm{MR,(n)}} = -\nabla \cdot \Big(\mathbf{b}^2_{(n)} \nabla \mathbf{x}_{(n)} \Big). \tag{5.6}$$

From this expression we can rationalize the chosen form of $\delta_{(n)}$ given in (5.5). When the solution estimate $\mathbf{x}_{(n)}$ is far from the true solution, $\mathcal{C}_1\left(\mathbf{x}_{(n)}\right)$ and $\mathcal{C}_2\left(\mathbf{x}_{(n)}\right)$ will be (relatively) large, which will cause the steering parameter $\delta_{(n)}$ to be large as well. This results in the weighting function $\mathbf{b}_{(n)}$ becoming approximately equal to $A^{-\frac{1}{2}}\left|\delta_{(n)}\right|^{-1}$. Since $\mathbf{b}_{(n)}$ is no longer a function of spatial coordinates, $\mathbf{g}_{\mathrm{MR,(n)}} \approx -\mathbf{b}^2_{(n)} \nabla^2 \mathbf{x}_{(n)}$. The presence of the Laplacian operator introduces smoothing properties that are favorable while the solution estimate is far from the true solution, such as in early iterations of the CG procedure. On the contrary, when $\mathbf{x}_{(n)}$ is close to the true solution, causing $\mathcal{C}_1\left(\mathbf{x}_{(n)}\right)$, $\mathcal{C}_2\left(\mathbf{x}_{(n)}\right)$, and $\delta_{(n)}$ to be small, resulting in $\mathbf{b}_{(n)}$ becoming approximately equal to $A^{-\frac{1}{2}}\left|\nabla \mathbf{x}_{(n)}\right|^{-1}$. In this case, $\mathbf{g}_{\mathrm{MR,(n)}}$ takes the form of a weighted Laplacian operator that has edge-preserving characteristics [65] which are beneficial when the estimate is close to the true solution.

The gradients of $\mathcal{C}_1(\mathbf{x})$ and $\mathcal{C}_2(\mathbf{x})$ evaluated at $\mathbf{x}_{(n)}$ are given in (4.53) and (4.54). A detailed derivation of these gradients can be found in Section 4.2.1. The complete gradient of $\mathcal{C}(\mathbf{x})$ evaluated at $\mathbf{x}_{(n)}$ is given by

$$\mathbf{g}_{(n)} = \mathcal{C}_{\mathrm{MR}}\left(\mathbf{x}_{(n)}\right)\left(\mathbf{g}_{1,(n)} + \mathbf{g}_{2,(n)}\right) + \Big(\mathcal{C}_1\left(\mathbf{x}_{(n)}\right) + \mathcal{C}_2\left(\mathbf{x}_{(n)}\right)\Big)\mathbf{g}_{\mathrm{MR,(n)}}, \tag{5.7}$$

but since $\mathcal{C}_{\mathrm{MR}}\left(\mathbf{x}_{(n)}\right) \equiv 1$, we have

$$\mathbf{g}_{(n)} = \mathbf{g}_{1,(n)} + \mathbf{g}_{2,(n)} + \Big(\mathcal{C}_1\left(\mathbf{x}_{(n)}\right) + \mathcal{C}_2\left(\mathbf{x}_{(n)}\right)\Big)\mathbf{g}_{\mathrm{MR,(n)}}. \tag{5.8}$$

Note that the weight of $\mathbf{g}_{\mathrm{MR,(n)}}$ in the above equation changes automatically *and* adaptively, thus resulting in an automated adaptive regularization scheme. Using the expressions in (4.54), (4.53), and (5.6) we get

$$\begin{aligned}\mathbf{g}_{(n)} = {} & 2\eta_1 \mathbf{A}_1^H \mathbf{r}_{1,(n)} \odot \mathbf{A}_1\mathbf{x}_{(n)} + 2\eta_2 \mathbf{A}_2^H \mathbf{r}_{2,(n)} \odot \mathbf{A}_2\mathbf{x}_{(n)} \\ & + \Big(\mathcal{C}_1\left(\mathbf{x}_{(n)}\right) + \mathcal{C}_2\left(\mathbf{x}_{(n)}\right)\Big)\Big[-\nabla\cdot\Big(\mathbf{b}_{(n)}^2\,\nabla\,\mathbf{x}_{(n)}\Big)\Big].\end{aligned} \tag{5.9}$$

Now that we have the gradient operator, we can explain the formulation of the CG procedure. During the n^{th} CG iteration, the update equation for the solution estimate is

$$\mathbf{x}_{(n+1)} = \mathbf{x}_{(n)} + \alpha_{(n)}\mathbf{d}_{(n)}, \tag{5.10}$$

where $\mathbf{d}_{(n)}$ is the search direction and $\alpha_{(n)}$ is a real-valued step length in the search direction. In CG methods the search direction is typically a combination of the gradient at the current iteration and the previous search direction. In this work the search direction $\mathbf{d}_{(n)}$ is computed as

$$\mathbf{d}_{(n)} = \mathbf{g}_{(n)} + \beta_{(n)}\mathbf{d}_{(n-1)}, \tag{5.11}$$

where $\beta_{(n)}$ is a weighting parameter. Again, we use the Polak-Ribiére weighting factor given by [49]

$$\beta_{(n)} = \frac{\mathbf{g}_{(n)}^H\left(\mathbf{g}_{(n)} - \mathbf{g}_{(n-1)}\right)}{\left\|\mathbf{g}_{(n-1)}\right\|_D^2}. \tag{5.12}$$

5.2.2 Finding the Step Length

The step length $\alpha_{(n)}$ is found by analytically minimizing $\mathcal{C}(\mathbf{x})$ along the direction $\mathbf{d}_{(n)}$, in the same manner as discussed for the phaseless spherical case in Section 4.2.1. In this case the expression for $\mathcal{C}\left(\mathbf{x}_{(n)} + \alpha_{(n)}\mathbf{d}_{(n)}\right)$ includes the MR term and is given by

$$\mathcal{C}(\mathbf{x} + \alpha\mathbf{d}) = \Big(\mathcal{C}_1(\mathbf{x} + \alpha\mathbf{d}) + \mathcal{C}_2(\mathbf{x} + \alpha\mathbf{d})\Big)\mathcal{C}_{\mathrm{MR}}(\mathbf{x} + \alpha\mathbf{d}), \tag{5.13}$$

where the (n) subscripts have again been excluded for simplicity. The terms $\mathcal{C}_1(\mathbf{x} + \alpha\mathbf{d})$ and $\mathcal{C}_2(\mathbf{x} + \alpha\mathbf{d})$ have been derived in Section 4.2.1 and are given in (4.64) and (4.65). We now need to find an expression for $\mathcal{C}_{\mathrm{MR}}(\mathbf{x} + \alpha\mathbf{d})$. We begin by using the following relationship

$$\mathcal{C}_{\mathrm{MR}}(\mathbf{x}) = \int_D \mathbf{b}^2(\vec{r}\,')\left(\left|\nabla\mathbf{x}\left(\vec{r}\,'\right)\right|^2 + \delta^2\right)d\vec{r}\,' = \|\mathbf{b}\,\nabla\mathbf{x}\|_D^2 + \delta^2\|\mathbf{b}\|_D^2, \tag{5.14}$$

and thus we can write

$$\begin{aligned}\mathcal{C}_{\mathrm{MR}}(\mathbf{x} + \alpha\mathbf{d}) &= \|\mathbf{b} \odot \nabla(\mathbf{x} + \alpha\mathbf{d})\|_D^2 + \delta^2\|\mathbf{b}\|_D^2 \\ &= \langle \mathbf{b} \odot \nabla(\mathbf{x} + \alpha\mathbf{d}), \mathbf{b} \odot \nabla(\mathbf{x} + \alpha\mathbf{d})\rangle_D + \delta^2\|\mathbf{b}\|_D^2 \\ &= \alpha^2\|\mathbf{b} \odot \nabla\mathbf{d}\|_D^2 + 2\alpha\mathrm{Re}\langle \mathbf{b} \odot \nabla\mathbf{x}, \mathbf{b} \odot \nabla\mathbf{d}\rangle_D + \|\mathbf{b} \odot \nabla\mathbf{x}\|_D^2 + \delta^2\|\mathbf{b}\|_D^2,\end{aligned} \tag{5.15}$$

showing that $\mathcal{C}_{\mathrm{MR}}(\mathbf{x} + \alpha\mathbf{d})$ is a second-degree polynomial in α as shown in [60].

Using (4.64), (4.65), and (5.15), the expression in (5.13) becomes a sixth-degree polynomial in α, and differentiation leads to a fifth-degree polynomial. The roots of the fifth-degree polynomial are found numerically, resulting in two pairs of complex conjugate roots and one real root. The step length is then taken to be the real root.

Once the solution update $\mathbf{x}_{(n+1)}$ is found, we then check if the convergence criterion in (4.29) is met. Otherwise the process continues until the condition is satisfied or a preset

maximum number of iterations has occurred.

5.2.3 Finding the Initial Guess

One important aspect that has not yet been discussed is the initial guess for the unknowns $\mathbf{x}_{(0)}$. In this work we demonstrate the robustness of the methods and because of this we use a simplistic initial guess based on back propagation. The initial back propagation estimation is found according to

$$\mathbf{x}_{\mathrm{BP}} = \mathbf{A}_1^H \left|\mathbf{f}_1\right|. \tag{5.16}$$

We use the closest measurement plane (S_1) for this estimation because more information about the evanescent radiation is captured when compared to the farther plane. The increased information quality results in a more accurate initial guess which in turn leads to improved convergence and stability. We then find the real value ζ such that $\mathcal{C}\left(\zeta \mathbf{x}_{\mathrm{BP}}\right)$ is a minimum with respect to ζ, and the initial guess for the solution becomes

$$\mathbf{x}_{(0)} = \zeta \mathbf{x}_{\mathrm{BP}}. \tag{5.17}$$

This concludes the presentation of the proposed MR-SRM. In the next chapter, the advantages of using MR in conjunction with the SRM will be presented.

Chapter 6

Results

The SRM algorithms developed for planar and spherical systems were tested with synthetic NF measurement data for verification and evaluation, and the planar algorithms were tested with experimental data as well. All of the tests were performed on a 2013 iMac with a 2.9 GHz quad-core Intel i5 processor equipped with 16 GB of RAM.

6.1 Error Metrics

To evaluate the performance of the various SRM algorithms, a set of error metrics is required. The first error metric that is used is the FF error, defined as

$$\text{FF error} = \frac{\left\| \left| \mathbf{E}_{FF}^{\text{true}} \right| - \left| \mathbf{E}_{FF}^{SRM} \right| \right\|}{\left\| \left| \mathbf{E}_{FF}^{\text{true}} \right| \right\|} \times 100\%, \tag{6.1}$$

where $\mathbf{E}_{FF}^{\text{true}}$ is the true FF electric field and $\mathbf{E}_{FF}^{SRM}$ is the FF electric field produced by the SRM. Additionally, sometimes the true FF is not available, such as the case during experimental tests. In these cases, a similar expression to (6.1) is used to evaluate the

discrepancy between two FF patterns, given by

$$\text{FF discrepancy} = \frac{\left\| |\mathbf{E}_{FF}| - \left|\mathbf{E}_{FF}^{SRM}\right| \right\|}{\||\mathbf{E}_{FF}|\|} \times 100\%, \tag{6.2}$$

where $\mathbf{E}_{FF}$ is the FF produced by the alternative method, such as the IFT or ME. It is important to note that this metric does not give any indication of the error in the FF pattern produced by the SRM, it simply quantifies how different the result is from the result produced by a different technique.

Secondly, it is useful to quantify how well the optimization process was able to 'fit' the measured data. To this end we take note of the $\mathcal{C}_1$ and potentially $\mathcal{C}_2$ terms of the cost functional after the final CG iteration. Expressed as a percentage, these values represent how accurately the equivalent currents are able to produce the NF data, although this accuracy does not directly correlate to accuracy of the corresponding FF pattern.

In addition, the convergence behaviour of the SRM during the CG minimization process is observed for each test. The memory and time requirements are also recorded to evaluate the practical limitations of each method.

6.2 Synthetic Tests

The initial tests of the SRM algorithms were performed on synthetically-generated NF measurement data. The 'AUT' for many of these tests consisted of an array of elementary, (*i.e.* Hertzian), dipoles. The use of such dipoles allowed for generation of the electric field in both the NF and FF regions analytically. The EFIE in (2.14) can be used to compute the electric field from an arbitrarily positioned infinitesimal dipole. The EFIE is evaluated by considering each infinitesimal dipole as an 'impulse' function of electric current and through the use of the dyadic Green's function. More specifically, the electric field can be computed

as

$$\vec{E}\left(\vec{r}\right) = -j\eta k_0 \overline{\overline{G}}\left(\vec{r},\vec{r}\,'\right) \cdot \vec{J}\left(\vec{r}\,'\right), \tag{6.3}$$

where $\vec{J}\left(\vec{r}\,'\right)$ is a unit vector in the direction of the elementary dipole (we arbitrarily assign a magnitude of one) and $\overline{\overline{G}}\left(\vec{r},\vec{r}\,'\right)$ is the dyadic Green's function computed analytically as

$$\overline{\overline{G}}\left(\vec{r},\vec{r}\,'\right) = \left[1 + \frac{1}{k_0^2}\nabla\nabla'_D \cdot\right] g_0 \overline{\overline{I}}, \tag{6.4}$$

with $\overline{\overline{I}}$ being the unit dyad. The expression in (6.3) is used to compute the field from each elementary dipole and the total field can then be found using superposition.

Noise is also added to the synthetic measurement data to analyze the performance of the various algorithms under non-ideal conditions. The measurement noise for each data point i is generated according to

$$f_i^{\text{noise}} = \Upsilon_i \rho \left|f_{\max}\right| e^{j\Psi_i}, \tag{6.5}$$

where Υ_i is a random number between -1 and 1 (uniformly distributed), Ψ_i is a random number between 0 and 2π (also uniformly distributed), and ρ is a positive parameter that controls the amount of noise added. A value of 0.01 for ρ results in the noise having a potential maximum value equal to 1% of the maximum measured electric field magnitude. Once generated, the noise vector is added to the synthetic measurement data prior to inversion.

6.2.1 Spherical SRM Tests

The synthetic test with the developed SRM for spherical NF measurements is performed on an array consisting of five y-directed elementary dipoles, as shown in Figure 6.1. The dipoles are arranged in a 'plus sign' configuration with a spacing of $\lambda/2$ and excited with uniform

magnitude and phase. The expression in (6.3) is used to generate the electric field produced

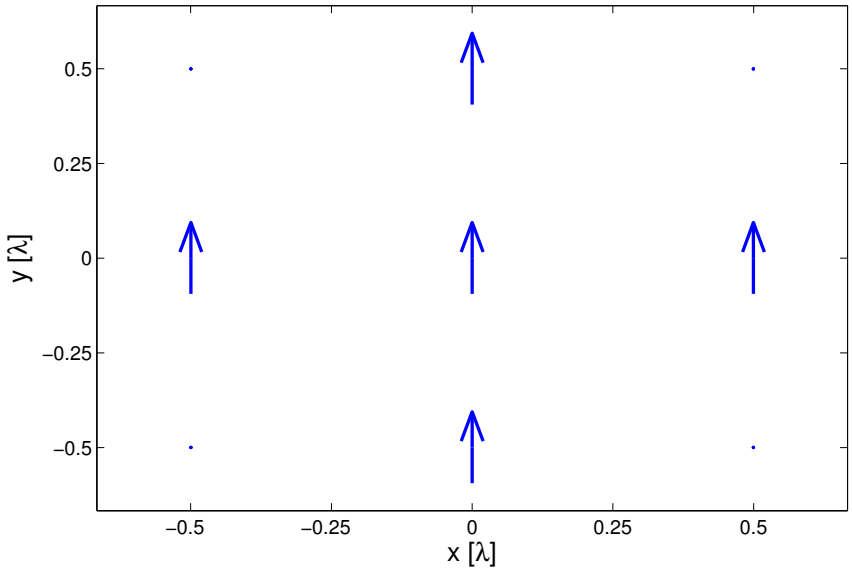

Fig. 6.1: The synthetic AUT formed by five elementary dipoles.

by the dipoles on two spherical measurement domains with radii of 3λ and 6.3λ. Since the maximum radial extent (MRE) of the AUT is half a wavelength, a sampling resolution of three degrees over both θ and φ is sufficient [42] and a realistic measurement scenario. This sampling resolution results in 7381 measurement locations, and therefore 14762 complex (amplitude and phase) data points (E_θ and E_φ) on each measurement domain. Note that only the measurement data from the first domain is used for the amplitude and phase SRM.

The generated synthetic data are shown in Figure 6.2, displaying the magnitude and phase of the θ and φ components of the measured electric field on the first measurement domain, including the 1% added noise.

For the first example we enclose the elementary dipoles with a spherical reconstruction surface of radius 0.75λ. We set the maximum edge length of the triangular mesh elements (generated using the open-source software GMSH [66]) to be $\lambda/10$. Further refinement of the mesh did not result in any significant reduction in the reconstruction error. This

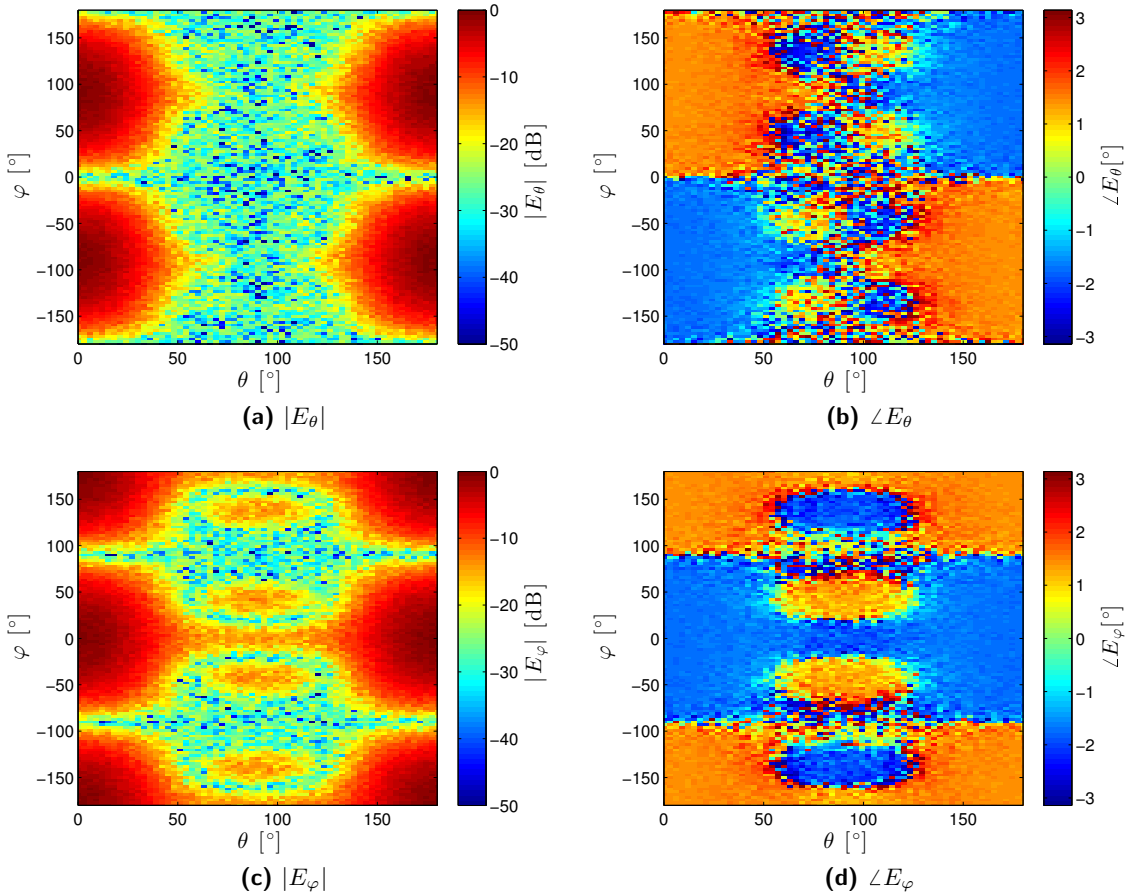

(a) $|E_\theta|$ **(b)** $\angle E_\theta$

(c) $|E_\varphi|$ **(d)** $\angle E_\varphi$

Fig. 6.2: The synthetically generated NF data from the five-dipole array on the measurement domain located 3λ away from the AUT. Both the (a,b) θ and (c,d) φ components of the measured electric field are shown including the 1% added noise.

discretization resulted in 1722 triangular elements, and thus 2583 RWG basis functions (one for each edge of the mesh). Since we must reconstruct both electric and magnetic currents in the spherical case, this problem results in 5166 unknowns and thus an operator size (for each measurement domain) of 14762×5166. Although these operators are dense they are never explicitly constructed in their entirety, but rather are efficiently approximated, as explained in what follows. The discretization of the problem leads to operators that are numerically rank-deficient, *i.e.* the operators contain many equations that contain very similar (redundant) information. For this reason we use adaptive cross approximation (ACA) [67] to build and store compressed operators that are approximately equal to their dense counterparts, reducing both time and memory requirements. In order to enforce Love's condition we add 'virtual' measurement data ($E = 0$) at points located on a spherical surface that is of a radius $\lambda/10$ *smaller* than the radius of the reconstruction surface. For this example enforcing Love's condition results in 2668 added data points, and since we enforce that the tangential electric field is zero at these points (two components) the size of each operator is increased to 20138×5166.

The equivalent electric and magnetic current distributions are generated by applying the SRM to both the phaseless measurement data and the data including both amplitude and phase. The equivalent currents are then used to produce the FF pattern over a spherical region of radius 1000λ. The true FF pattern is produced analytically over the same region and is used for comparison. Figure 6.3 shows a comparison of the produced FF magnitude patterns. To further clarify the difference between the reconstructed and true FF patterns, Figure 6.3 also shows plots of the residual FF pattern (*i.e.* the absolute difference between the normalized true FF pattern and the normalized FF pattern using the SRM) for each case.

The magnitude and direction of the produced equivalent surface currents are shown in Figure 6.4. The current distributions exist over the complete spherical surface but only one

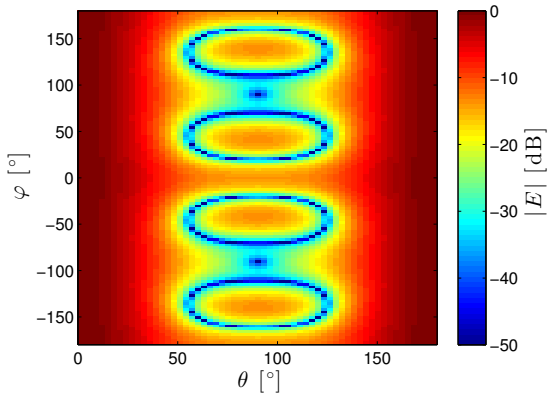

(a) True FF

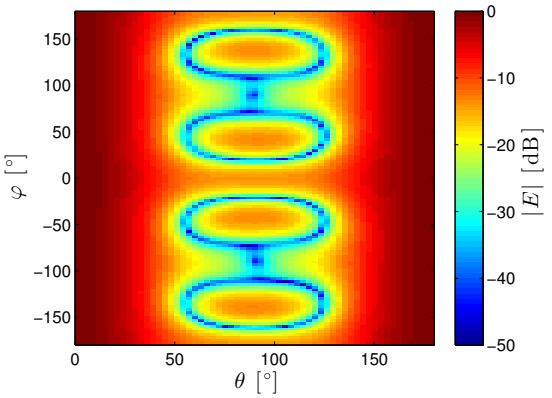

(b) FF from SRM

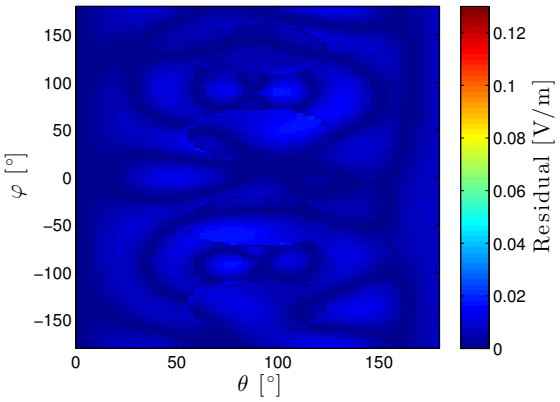

(c) FF Residual from SRM

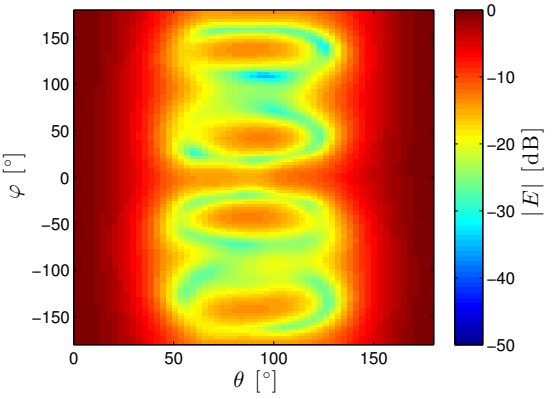

(d) FF from SRM with phaseless data

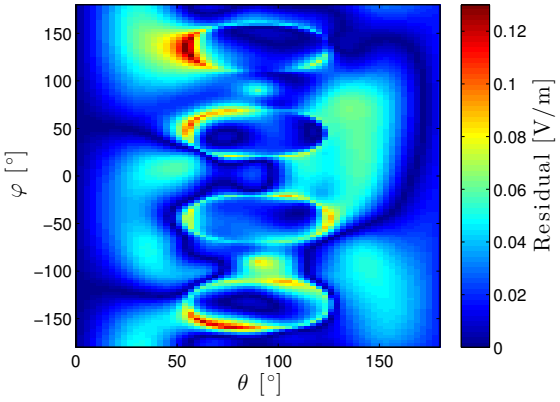

(e) FF Residual from SRM with phaseless data

Fig. 6.3: A comparison of the FF patterns for the five-dipole array. The true FF pattern (a) is compared to the FF patterns produced using (b) SRM with both amplitude and phase data and (d) SRM with phaseless data. Residual plots are also shown in (c) and (e) for the amplitude-and-phase and phaseless cases, respectively.

half ($z > 0$) of the surface is shown for simplicity. Enforcing Love's condition forces the currents to relate to the fields on the reconstruction surface according to (2.27) and (2.28). To verify this we plot the actual tangential electric field on the reconstruction surface and qualitatively observe the relationship. Figure 6.5 shows the tangential electric field produced by the AUT on the reconstruction surface compared with the reconstructed magnetic current distributions. The point of view for these plots is from the positive z for clarity. Note that the directions of the currents and fields will be perpendicular to each other as a result of the cross-products in the boundary conditions. With this in mind, we can see that the reconstructed magnetic current distribution has the same relative magnitude distribution as the true tangential electric field and the correct direction in the case when phase information is used. Without phase information the magnitude accuracy degrades slightly. Keep in mind that the reconstructed currents are attempted solutions to an ill-posed inverse problem, and we cannot expect excellent agreement with the true fields.

The FF error, CG times, and memory requirements are shown in Table 6.1. The time

Table 6.1: Five-Dipole Array SRM Results - With Love's Condition

	SRM (w/phase)	SRM (phaseless)
FF error	1.20%	6.59%
Iterations	34	500
CG Time	6.37 s	2 min 32 s
Memory	673 MB	795 MB

required to build the operators is 34 minutes and 50 seconds when phase information is used and increases to 44 minutes and 54 seconds in the phaseless case. The FF operator required 20 minutes and 13 seconds to build, but this is highly dependent on the desired resolution of the FF pattern. It should be noted that the condition number of the operator matrices is approximately 10^{19} when Love's condition is not enforced and decreases to 10^{7} when Love's condition is enforced. The improvement in conditioning reduces the ill-posedness of

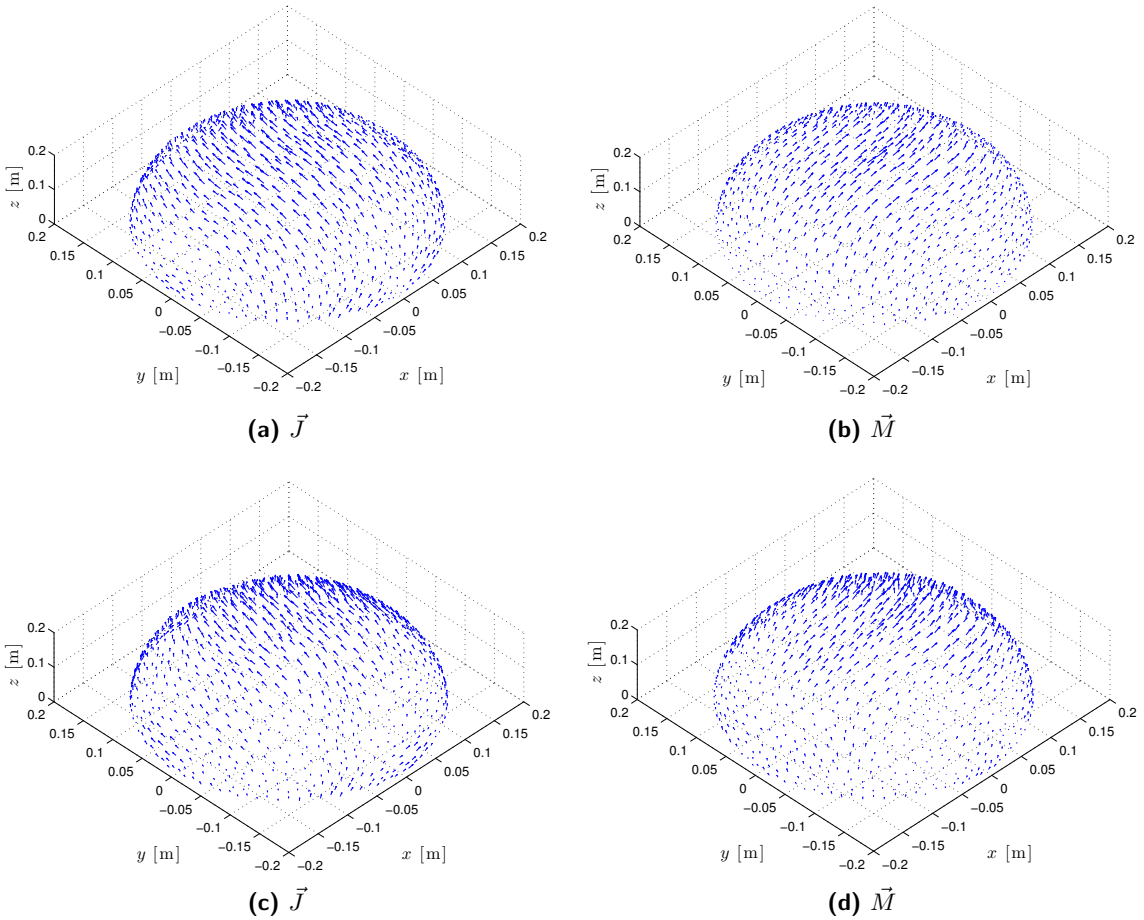

(a) $\vec{J}$ **(b)** $\vec{M}$

(c) $\vec{J}$ **(d)** $\vec{M}$

Fig. 6.4: The produced equivalent currents on the spherical reconstruction surface of radius 0.75λ using Love's condition. The electric and magnetic currents generated from the SRM applied to complex (amplitude and phase) data are shown in (a) and (b), while the currents produced using SRM with phaseless data are shown in (c) and (d).

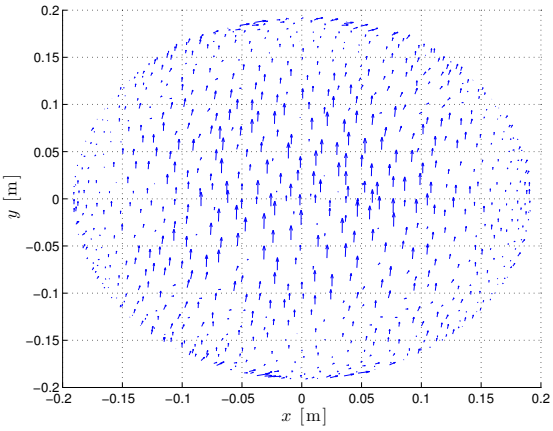

(a) True tangential $\vec{E}$

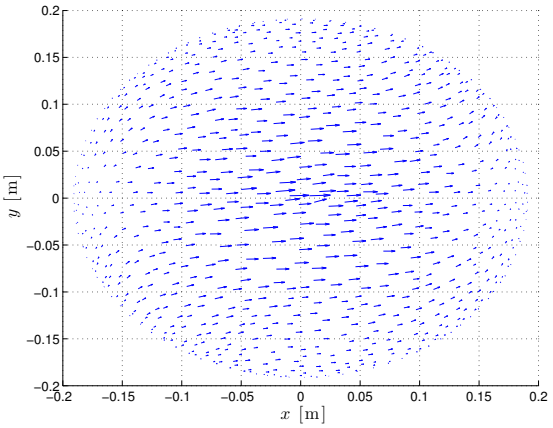

(b) $\vec{M}$ from amplitude and phase data

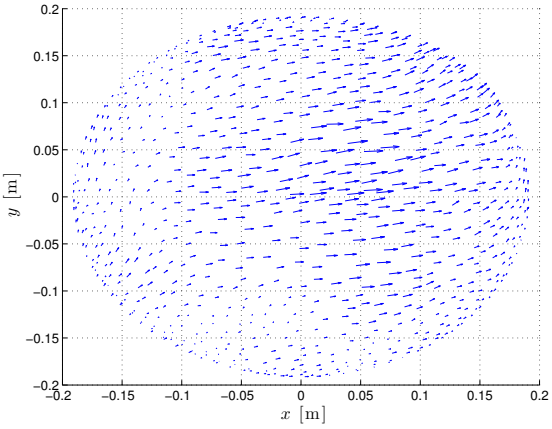

(c) $\vec{M}$ from phaseless data

Fig. 6.5: The true tangential electric field on the reconstruction surface (a) compared with the reconstructed magnetic current distributions produced by the SRM using complex (b) and phaseless data (c).

the system and increases the stability of the solution process. The agreement between the FF patterns produced by SRM and the true FF pattern is very good, and the decrease in accuracy when phase information is removed is expected. The time requirements for these algorithms are dominated by the time taken to build the matrix operators, and is the main limitation of the SRM. The other limitation of this implementation is the large memory requirement that may become impractical if a larger reconstruction surface is needed for a larger antenna.

Please note that in the developed implementation it is not a requirement that the reconstruction surface be spherical in shape. In fact, the reconstruction surface can be any closed surface that completely surrounds the AUT. This feature can be taken advantage of to reduce the number of unknowns by using a surface that is conformal to the AUT.

6.2.2 Planar SRM Tests

Elliptical Array

The first synthetic test is performed on a uniformly-spaced array of elementary dipoles, all oriented in the y direction. The elements are uniformly spaced at $\lambda/2$ intervals and span 8λ along the x axis and 4λ along the y axis, as shown in Figure 6.6. The excitation magnitude and phase of the array elements is uniform in this first example. The expression in (6.3) is used to generate the field produced by the array on two measurement planes, located 3λ and 5.3λ away from the array, in the direction of the positive z axis. The electric field is computed at $\lambda/2$ intervals over the measurement planes, each having x and y dimensions of $30\lambda \times 30\lambda$. This results in 7442 pieces of measurement data (E_x and E_y) on *each* measurement plane. Just as in the spherical examples, only the first plane of measurement data is used for the amplitude-and-phase SRM. The amplitude and phase of the NF measurement data is shown in Figure 6.7 for reference, with 2% noise added according to (6.5). Note that for this example the antenna is linearly polarized in the y

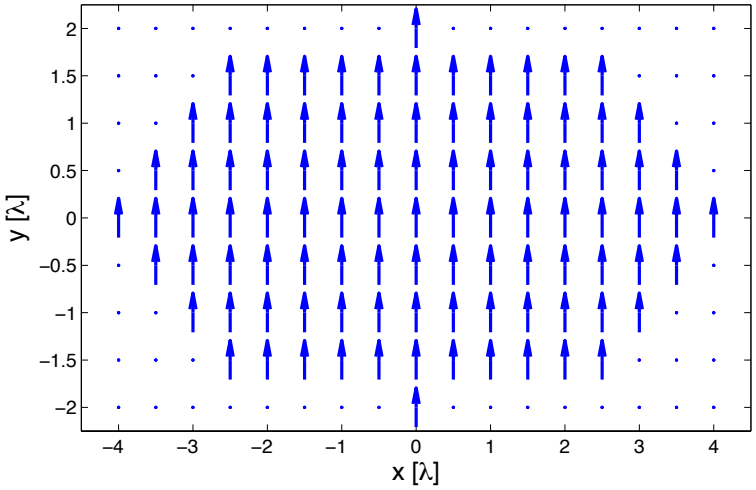

Fig. 6.6: The synthetic AUT consisting of a uniformly-spaced array of elementary dipoles.

direction, thus, the 'measured' E_x is very small compared to E_y and not shown here.

In this example, the reconstruction surface D is a planar surface of dimensions $8.5\lambda \times 4.5\lambda$ (slightly larger than the AUT), discretized into uniform square elements of side length $\lambda/10$, and placed a distance of $\lambda/20$ in front of the array. This discretization leads to 3956 elements, and therefore 7912 unknowns (M_x and M_y). This results in each operator having a size of 7442×7912, although half of the elements are *zero* because of the decoupled nature of the integral equations, as explained in Section 4.3. The parts of the operator that are zero are not computed, stored, or used during the computation of any matrix-vector products.

The equivalent currents are produced from the phaseless NF data using MR-SRM as well as basic SRM (without MR) for comparison. Once the equivalent magnetic currents are found, the FF is computed on a spherical surface with a radius of 1000λ. The results generated from applying SRM to the measurement data *with* both amplitude and phase information are included as well. The FF pattern from the true sources as well as the FF produced using ME (amplitude and phase data) and the IFT (phaseless data) are generated for comparison. The IFT method used is explained in further detail in [41]. It should be

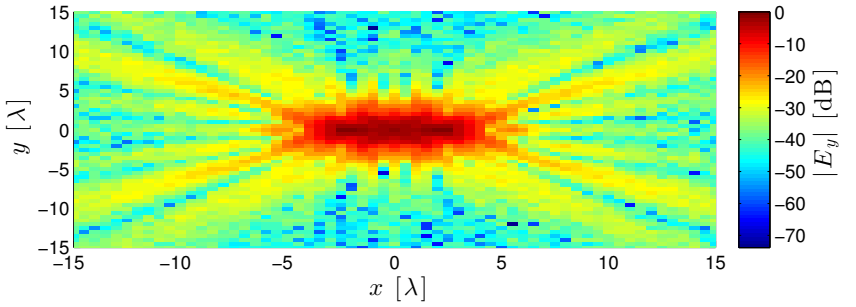

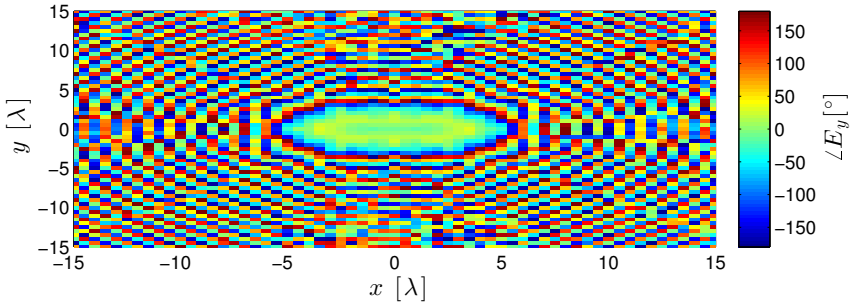

(a) 3λ plane

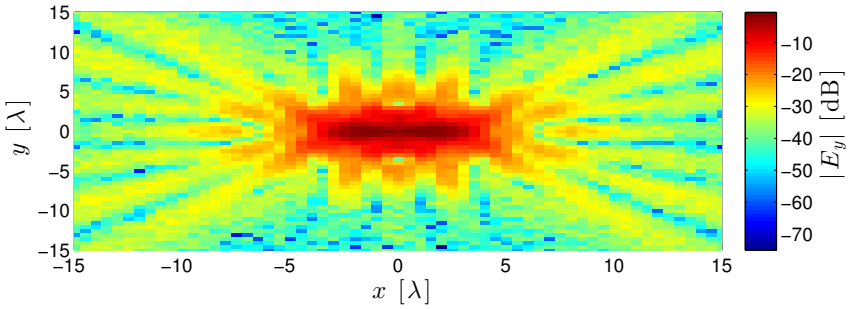

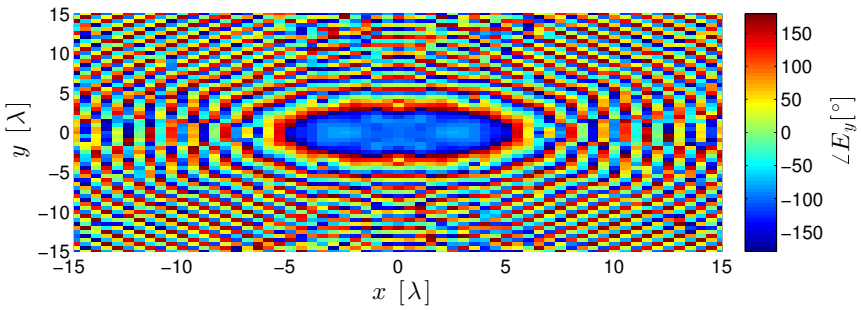

(b) 5.3λ plane

Fig. 6.7: The synthetically generated NF data (E_y) on the measurement planes located (a) 3λ and (b) 5.3λ away from the AUT.

noted that the initial guess for the IFT takes into account the shape of the AUT aperture as well as the direction of the main beam, while the SRM and MR-SRM do not have any information regarding the beam direction. For these tests a tolerance value of 10^{-3} is used to determine when the iterative procedures should be stopped.

The results of applying the various NF-FF transformation methods are shown in Figure 6.8, which compares the performance of the amplitude-and-phase algorithms, and Figure 6.9, which compares the performance of the phaseless algorithms. It should be noted that the displayed FF patterns are truncated at $\theta = \pm 65^{\circ}$, consistent with the critical angle for planar measurements determined by the size and location of the *farthest* measurement plane [68].

Additionally, a second synthetic test was performed on the same setup as above, with the exception of the excitation amplitudes of the dipole elements. In this case, the elements are excited in a cosine-tapered manner along the x-axis, with a maximum of one in the center and decreasing to zero at the right and left edges of the array. The resulting FF patterns are shown in Figure 6.10, for the amplitude and phase data, and Figure 6.11 for the phaseless data.

The FF error levels for the uniform and tapered array tests are shown along with the number of CG iterations, minimization time, and memory requirements in Tables 6.2 and 6.3. As can be seen from the FF plots and the tabulated results, the FF patterns produced by the SRM-based techniques agree quite well with the true FF pattern, and the inclusion of MR for the phaseless test resulted in a slight improvement in the FF accuracy compared to basic SRM. The main disadvantage exhibited by the SRM in comparison to ME-based methods are the time and memory requirements. For this example, the IFT and ME transformations were performed almost in real time and required negligible amounts of memory. On the other hand, the SRM FF patterns were consistently more accurate than those produced by ME and the IFT, especially when considering the sidelobes. We speculate

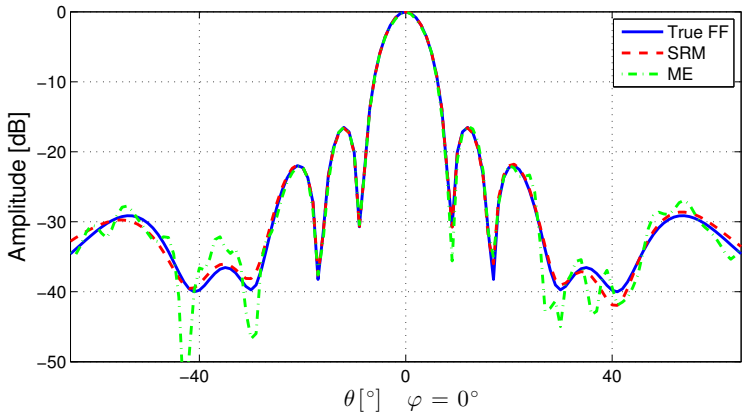

(a)

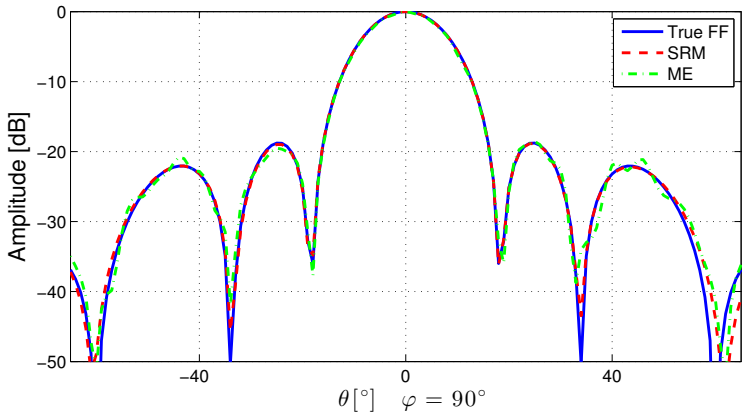

(b)

Fig. 6.8: A comparison of the uniform array FF pattern produced using NF data with both amplitude and phase at two different cuts: $\varphi = 0°$ and $\varphi = 90°$. Results are shown for the true FF computed analytically (blue solid line) and the FF produced by: (i) SRM (red dashed line) and (ii) ME (green dash-dotted line).

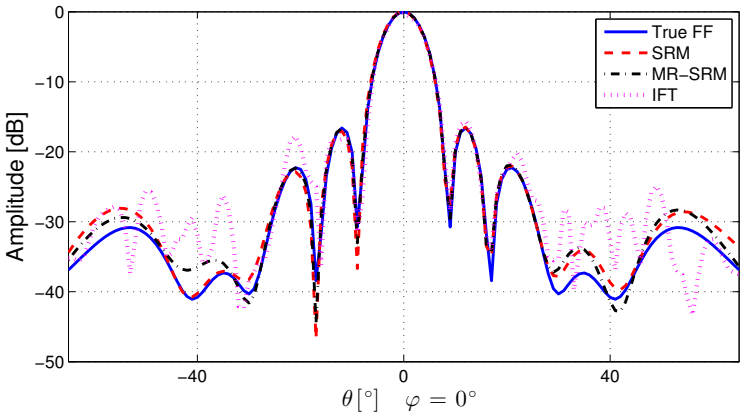

(a)

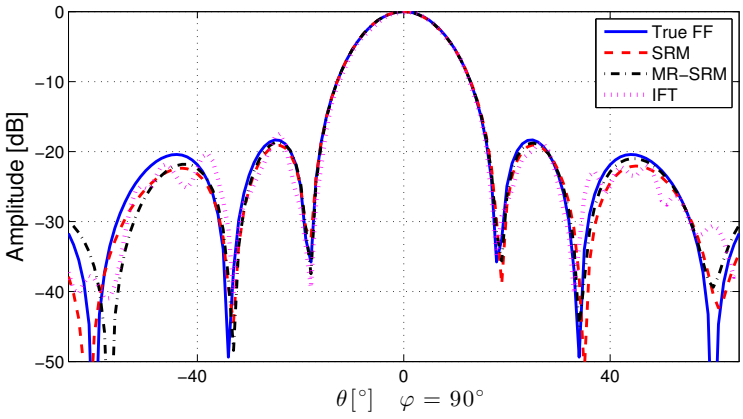

(b)

Fig. 6.9: A comparison of the uniform array FF pattern produced using phaseless NF data at two different cuts: $\varphi = 0^\circ$ and $\varphi = 90^\circ$. Results are shown for the true FF computed analytically (blue solid line) and the FF produced by: (i) SRM without MR (red dashed line); (ii) MR-SRM (black dash-dotted line); and, (iii) IFT (magenta dotted line).

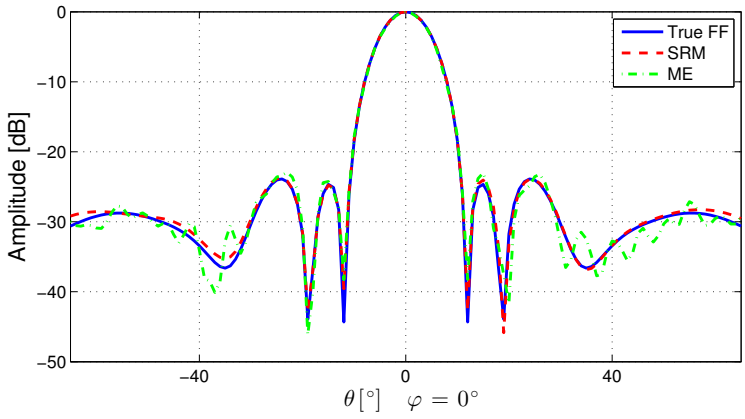

(a)

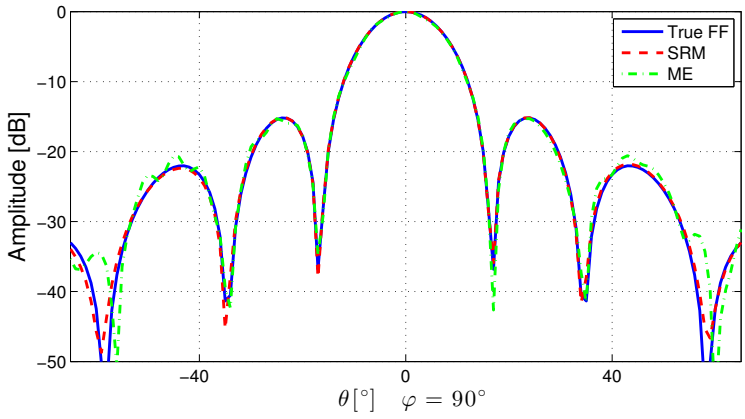

(b)

Fig. 6.10: A comparison of the tapered array FF pattern produced using NF data with amplitude and phase at two different cuts: $\varphi = 0°$ and $\varphi = 90°$. Results are shown for the true FF computed analytically (blue solid line) and the FF produced by: (i) SRM (red dashed line) and (ii) ME (green dash-dotted line).

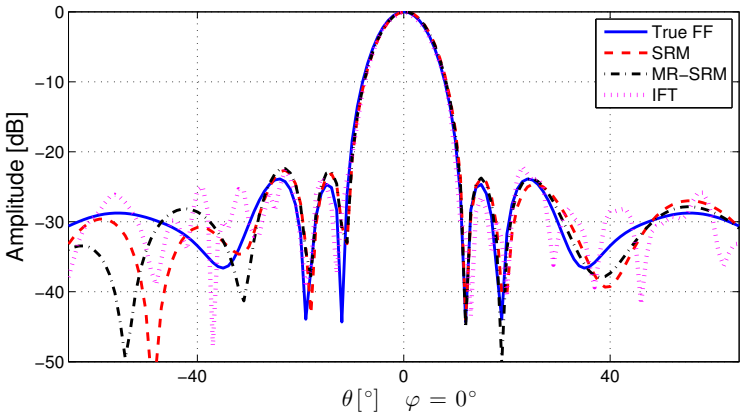

(a)

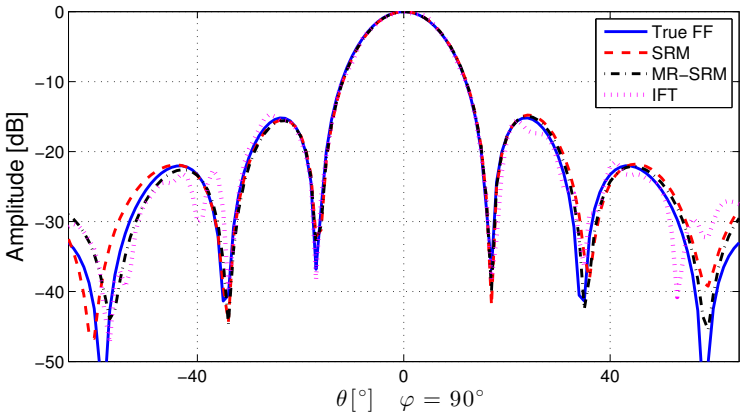

(b)

Fig. 6.11: A comparison of the tapered array FF pattern produced using phaseless NF data at two different cuts: $\varphi = 0^\circ$ and $\varphi = 90^\circ$. Results are shown for the true FF computed analytically (blue solid line) and the FF produced by: (i) SRM without MR (red dashed line); (ii) MR-SRM (black dash-dotted line); and, (iii) IFT (magenta dotted line).

that this enhanced accuracy might be due to the fact that the ME-based algorithms assume that the NF data outside the measurement plane is zero whereas the SRM-based methods make no such assumptions.

Table 6.2: Uniform Excitation Results

	SRM (w/phase)	ME (w/phase)	MR-SRM	SRM	IFT
FF error	0.68%	2.60%	2.48%	3.44%	6.06%
Iterations	11	N/A	282	338	62
Min. Time	4.47 s	N/A	3 min 51 s	4 min 37 s	5.47 s
Memory	641 MB	669 KB	1091 MB	1091 MB	4.94 MB

Table 6.3: Tapered Excitation Results

	SRM (w/phase)	ME (w/phase)	MR-SRM	SRM	IFT
FF error	0.71%	2.66%	3.80%	4.29%	5.36%
Iterations	13	N/A	346	347	39
Min. Time	6.56 s	N/A	4 min 44 s	4 min 45 s	5.36 s
Memory	641 MB	669 KB	1091 MB	1091 MB	4.94 MB

Although the phaseless FF patterns produced by MR-SRM were slightly more accurate than those produced by basic SRM (phaseless), the benefit of MR is more pronounced in the reconstructed equivalent currents. The equivalent current distributions (M_x) produced by both methods applied to phaseless NF data are shown in Figures 6.12 and 6.13. The currents produced by MR-SRM accurately represent the AUT aperture field, while the currents produced by SRM exhibit unrepresentative variations (spurious oscillations). The reason that such spurious oscillations are suppressed in the MR-SRM is mainly due to the Laplacian regularizer associated with MR. The edge-preserving characteristics of MR will be demonstrated in the next example when there is a defect in the AUT. It is also important to note that the IFT cannot directly produce the equivalent current information.

The convergence behaviour of the MR-SRM and SRM as applied to the phaseless NF

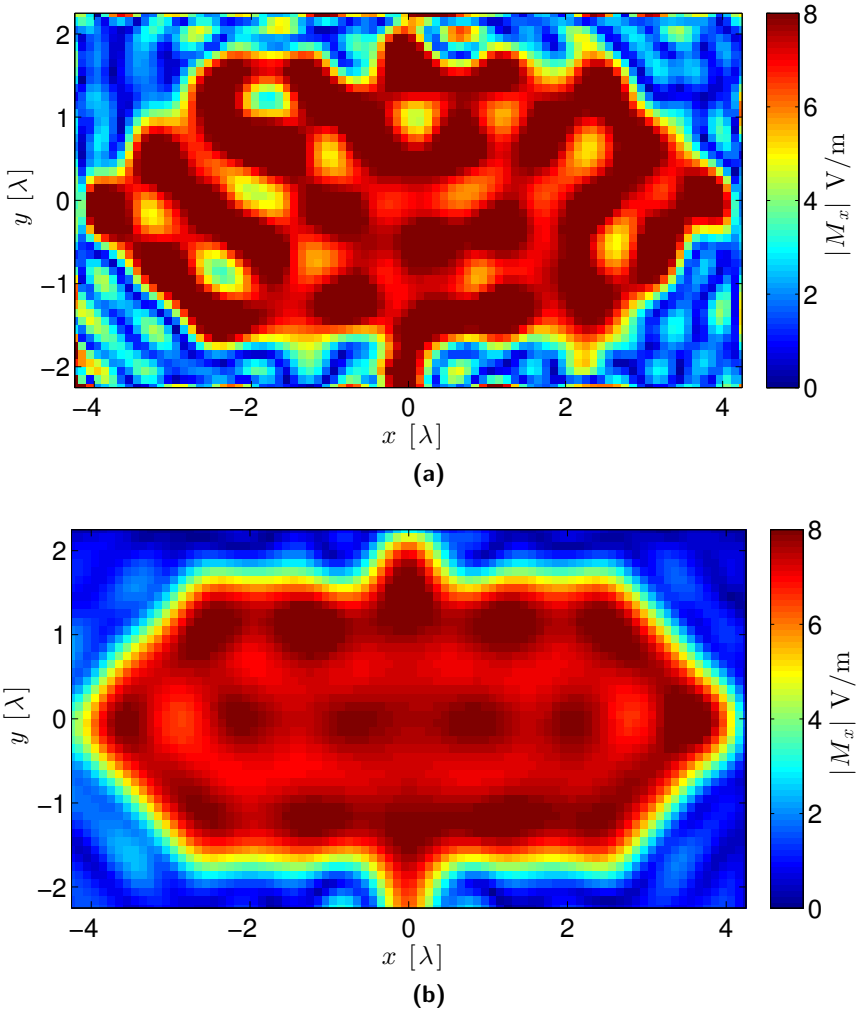

Fig. 6.12: A comparison of the equivalent magnetic current distribution produced by (a) SRM without MR and (b) MR-SRM for the uniformly excited dipole array using phaseless NF data.

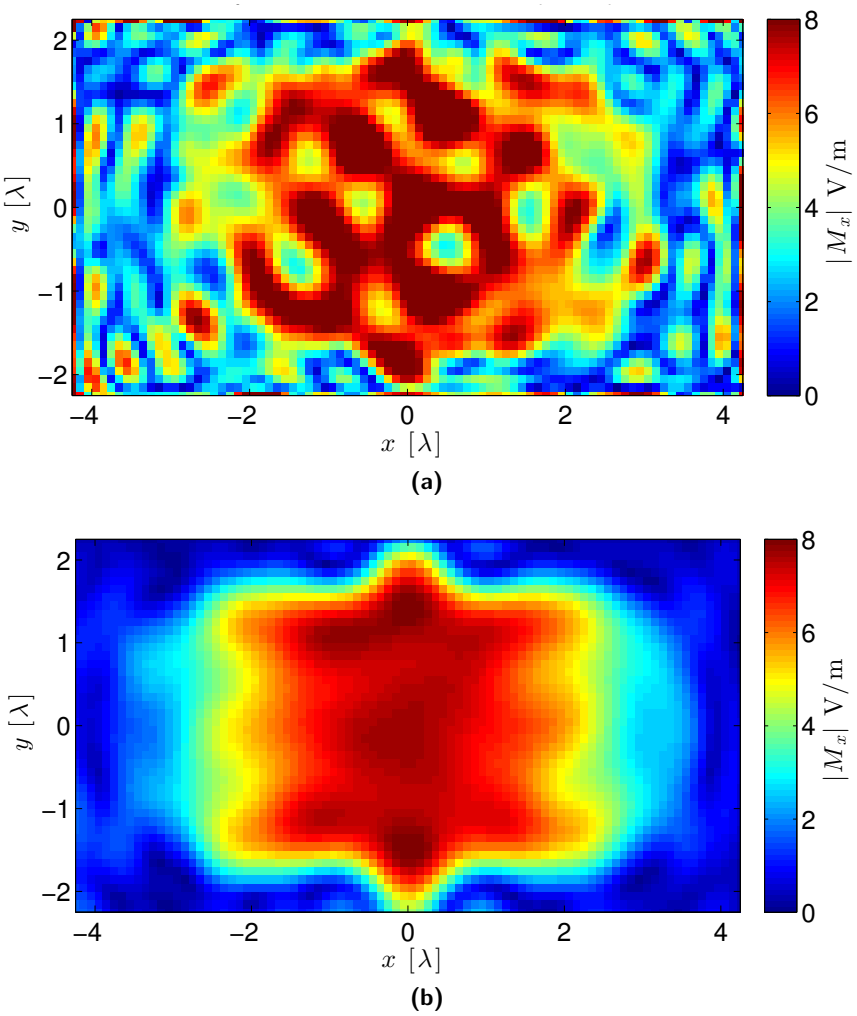

Fig. 6.13: A comparison of the equivalent magnetic current distribution produced by (a) SRM without MR and (b) MR-SRM for the tapered excitation dipole array using phaseless NF data.

data is shown in Figure 6.14 for the uniform and tapered array tests. Initially, the magnitude errors $\mathcal{C}_1\left(\mathbf{x}_{(n)}\right)$ and $\mathcal{C}_2\left(\mathbf{x}_{(n)}\right)$ are minimized by both methods at the same rate. After 30-40 iterations, the difference between the two methods becomes clear. Although SRM is able to minimize the terms $\mathcal{C}_1$ and $\mathcal{C}_2$ to a greater extend than MR-SRM, this does not result in a more accurate solution in terms of the equivalent currents and the FF radiation pattern. The lack of MR allows the CG procedure to further minimize $\mathcal{C}_1$ and $\mathcal{C}_2$ at the expense of solution quality. This can also be better understood by noting the shape of a standard L-curve plot and that an appropriate solution (the corner of the L-curve) does not necessarily correspond to the smallest data misfit.

Array With Scanned Beam

To further evaluate the performance of the developed planar SRM algorithms we introduce a scanned beam antenna as our AUT. The setup for this test is the same as the elliptical array in Section 6.2.2 with the uniform excitation magnitude, except that we now add a linear phase shift to the array elements along the x-axis to direct the main beam in the $\theta = 20^\circ$ direction, similar to an example presented in [13]. In this test we also decrease the tolerance factor to 10^{-4} to allow the methods to converge to a proper solution.

It should be noted that the initial back propagation guesses for the equivalent currents used by the various SRM methods are not able to approximately estimate the direction of the main beam. A more advanced guess could be employed, such as the one used in the IFT method, but for the purposes of this test the simple guess will demonstrate the robustness of our proposed method. The FF patterns produced by the various methods are shown in Figures 6.15 and 6.16, using complex and phaseless NF data, respectively.

The performance metrics and error information for the scanned beam tests are shown in Table 6.4. As an initial observation, it is clear that again the SRM-based techniques resulted in an improved FF pattern accuracy compared to ME and the IFT. In the phaseless case,

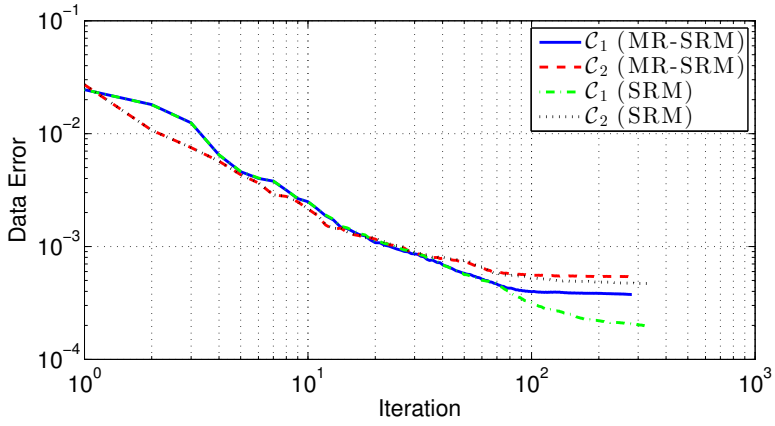

(a)

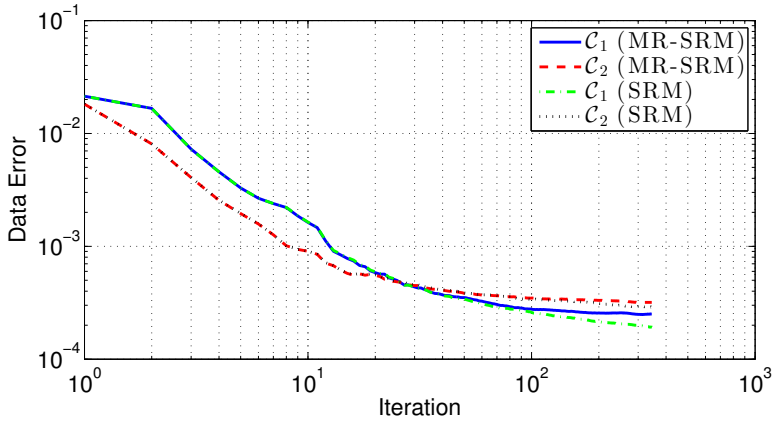

(b)

Fig. 6.14: The convergence behaviour of the MR-SRM and SRM for the (a) uniform and (b) tapered excitation of the dipole array. The progression of the data error on each plane, *i.e.* $\mathcal{C}_1\left(\mathbf{x}_{(n)}\right)$ and $\mathcal{C}_2\left(\mathbf{x}_{(n)}\right)$, is shown as a function of the CG iterations.

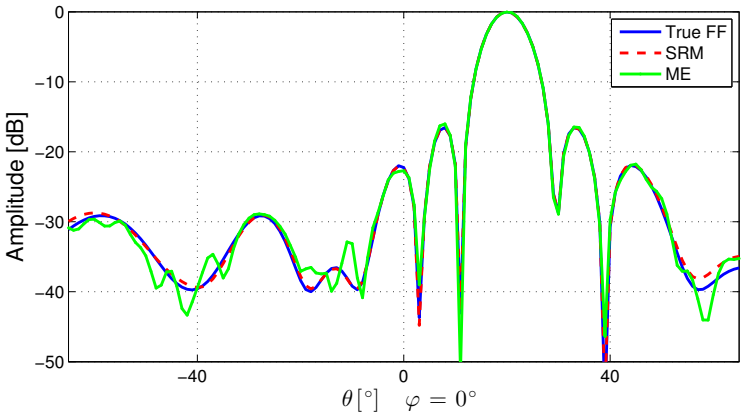

(a)

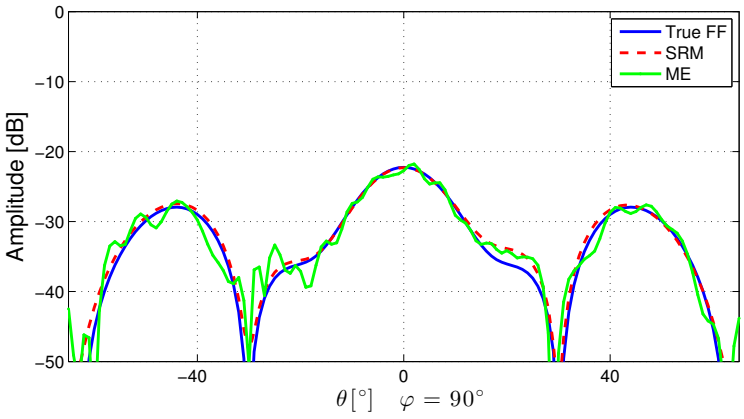

(b)

Fig. 6.15: A comparison of the scanned beam FF pattern produced using NF data with both amplitude and phase at two different cuts: $\varphi = 0°$ and $\varphi = 90°$. Results are shown for the true FF computed analytically (blue solid line) and the FF produced by: (i) SRM (red dashed line) and (ii) ME (green dash-dotted line).

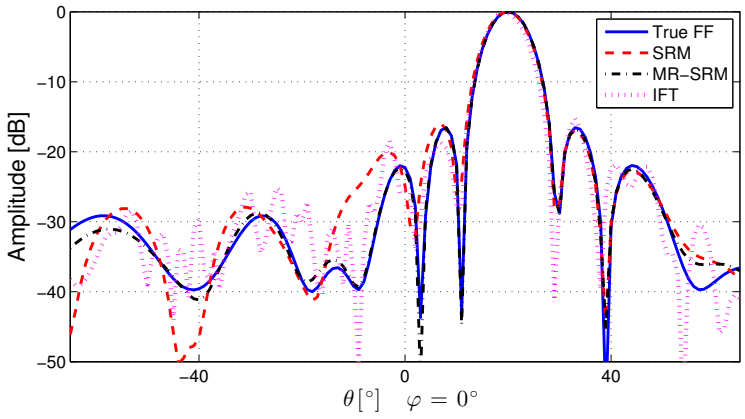

(a)

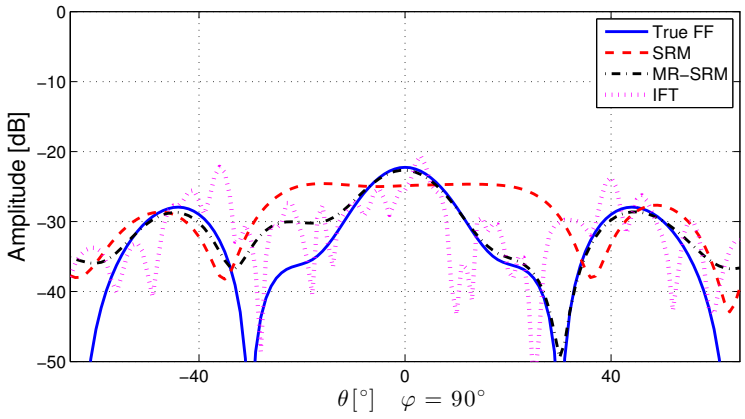

(b)

Fig. 6.16: A comparison of the scanned beam FF pattern produced using phaseless NF data at two different cuts: $\varphi = 0°$ and $\varphi = 90°$. Results are shown for the true FF computed analytically (blue solid line) and the FF produced by: (i) SRM without MR (red dashed line); (ii) MR-SRM (black dash-dotted line); and, (iii) IFT (magenta dotted line).

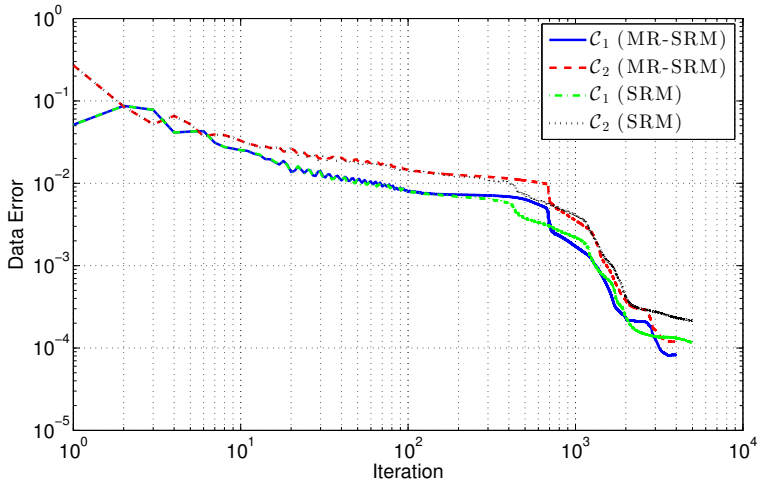

Fig. 6.17: The convergence behaviour of the MR-SRM and SRM for the scanned beam array. The progression of the data error on each plane, *i.e.* $\mathcal{C}_1\left(\mathbf{x}_{(n)}\right)$ and $\mathcal{C}_2\left(\mathbf{x}_{(n)}\right)$, is shown as a function of the CG iterations.

the agreement between MR-SRM and the true FF pattern was significantly better than both SRM and the IFT. Furthermore, both SRM methods seem to be more robust in the presence of noise compared to ME and the IFT as indicated by the reconstruction of the FF sidelobes. In this example, the unfavorable time requirements of the MR-SRM and the SRM are further accentuated, although the time may be reduced if the beam direction is taken into account with the initial guess.

Table 6.4: Scanned Beam Results

	SRM (w/phase)	ME (w/phase)	MR-SRM	SRM	IFT
FF error	0.91%	2.11%	3.32%	12.22%	13.45%
Iterations	12	N/A	4026	5000	1019
Min. Time	5.91 s	N/A	50 min 30 s	62 min 11 s	10.58 s
Memory	641 MB	669 KB	1091 MB	1091 MB	4.94 MB

The convergence behaviour of MR-SRM and SRM is shown in Figure 6.17. The same conclusions about the convergence can be drawn as those based on the uniform and tapered array examples.

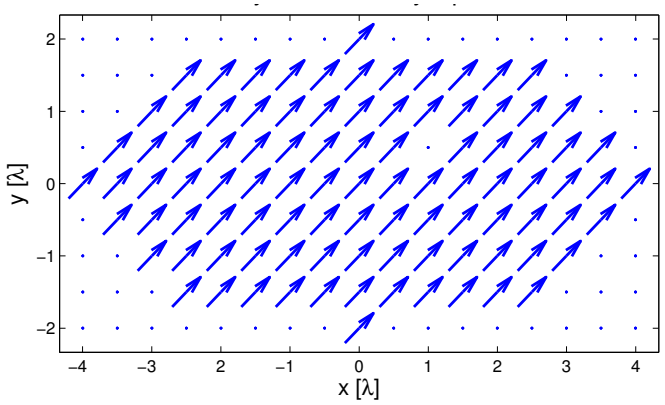

Fig. 6.18: The array of elementary dipoles at a $45°$ angle with one element deactivated.

Diagnostics

The equivalent currents are not only byproducts during the generation of the FF pattern, but in fact they can provide very useful information on their own. Since the currents are directly related to the tangential fields on the reconstruction surface, any irregularities or defects can be identified visually. The same cannot be said for ME or the IFT, since the equivalent currents and/or aperture fields are not directly produced. To demonstrate this advantage, we will use the same uniform elementary dipole array as in Section 6.2.2 with a few changes. First, we will rotate all of the dipoles in the x-y plane by $45°$ to demonstrate that anomalies in both x and y directed current distributions can be detected accurately. Secondly, we deactivate one element in the array, as shown in Figure 6.18. Both the MR-SRM and SRM are used to perform the NF-FF transformation, and the produced equivalent current distributions are shown in Figures 6.19 and 6.20. The deactivated array element can be easily identified using the current distribution produced by MR-SRM, but cannot be clearly identified from the current distribution produced by SRM. Also of note, the rest of the aperture field of the AUT was reconstructed accurately by the MR-SRM. This is because the added MR provides both a Laplacian regularizer and an edge-preserving regularizer. The Laplacian regularizer is responsible for suppressing any 'spurious' variations in the current

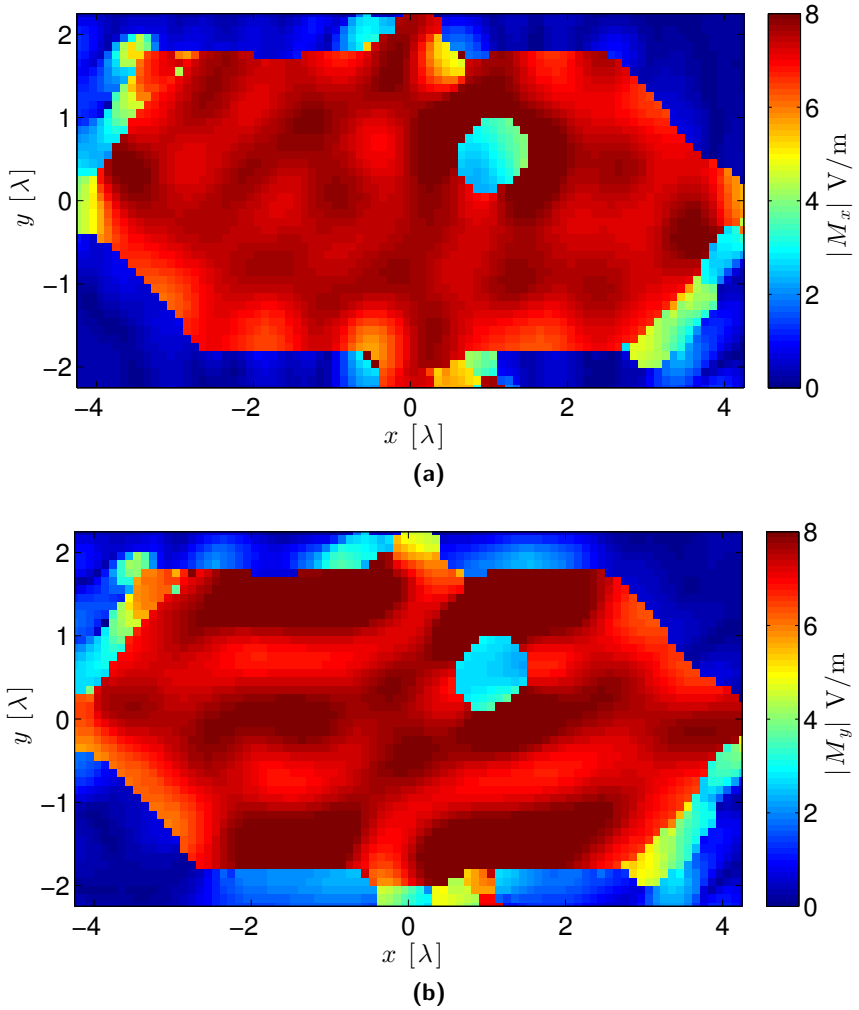

Fig. 6.19: The equivalent magnetic current reconstructed by MR-SRM for the uniform dipole array with one deactivated element using phaseless NF data. M_x is shown in (a) and M_y in (b).

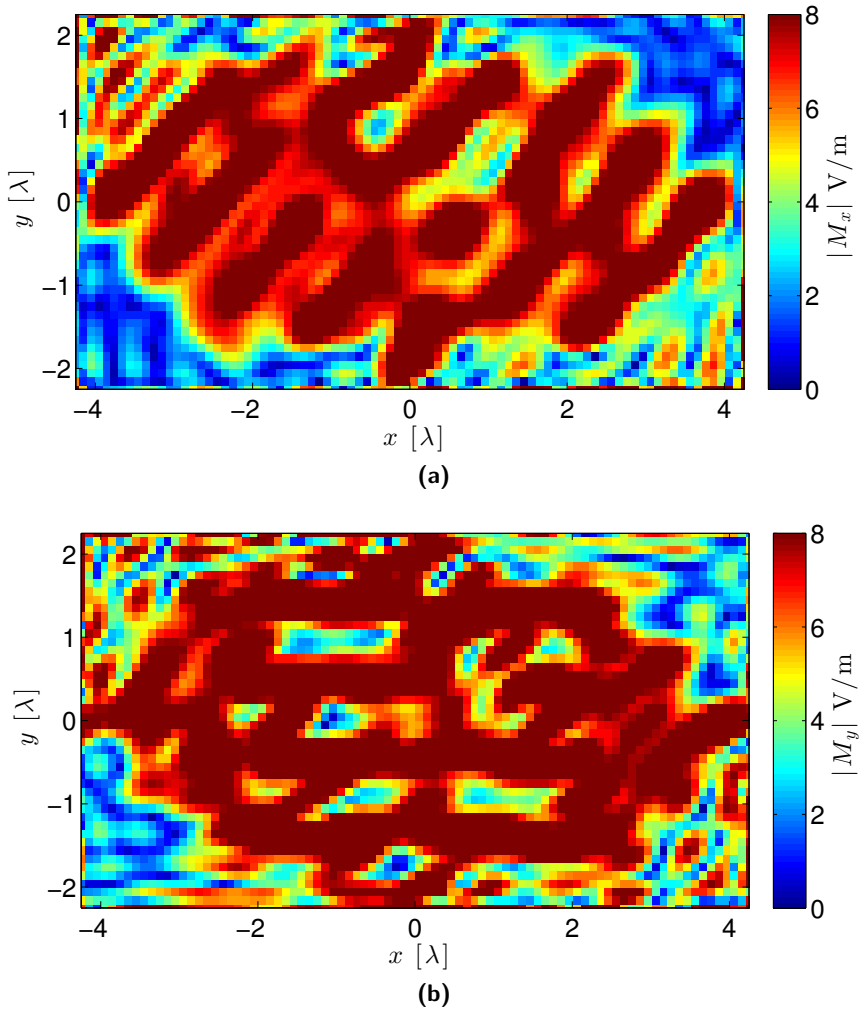

Fig. 6.20: The equivalent magnetic current reconstructed by SRM for the uniform dipole array with one deactivated element using phaseless NF data. M_x is shown in (a) and M_y in (b).

distribution and the edge-preserving regularizer is responsible for clearly identifying the deactivated array element.

6.3 Experimental Tests

To further evaluate the developed planar SRM algorithms, we collected a set of NF measurement data using the planar near-field range (PNFR) at the University of Manitoba (manufactured by Nearfield Systems Inc.). This test will examine the performance of the algorithms in the presence of potential measurement errors including alignment errors, probe positioning errors, multiple reflections, and interference. The AUT used was a dual-ridged pyramidal horn antenna that is linearly polarized. The horn antenna is shown for reference in Figure 6.21. The aperture size of the horn is approximately 12.5 cm $\times$ 7 cm and the mea-

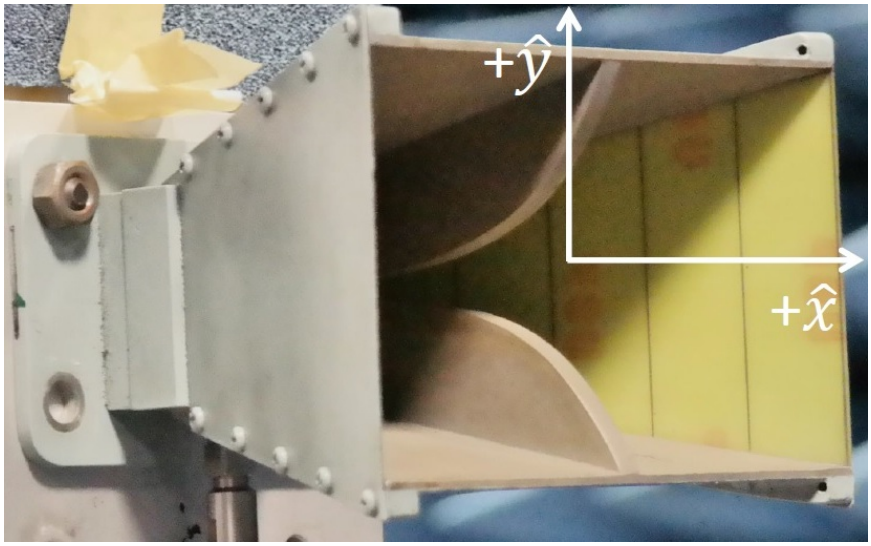

Fig. 6.21: The dual-ridged pyramidal horn antenna used for experimental verification with the PNFR. The horn antenna is linearly polarized along the y-axis. Image courtesy of X. Li.

surements were taken at a frequency of 9 GHz. The probe used to collect the measurement data was a WR-90 open-ended waveguide (OEW) antenna, operating in the X-band (8.2

to 12.4 GHz). This probe also has tapered ends for the purpose of minimizing diffraction effects. The tangential electric field was measured over a rectilinear grids of size 0.68 m $\times$ 0.68 m at distances of 4.68λ and 6.51λ from the AUT, with a sampling resolution of approximately 1.17 cm. Although both the amplitude and phase of the electric field was measured, the phase information was discarded when applying the phaseless NF-FF transformation techniques. The reconstruction surface D has a size of 12.5 cm $\times$ 7 cm with uniform square cells of size 2.5 mm $\times$ 2.5 mm, and is placed in front of the horn antenna at a distance of $\lambda/20$.

The amplitude and phase of the measured NF data is shown in Figure 6.22. The SRM was applied to the experimental NF measurements *with phase* and the obtained FF pattern is compared to that obtained by ME in Figure 6.23. For reference, the 'true FF' has been produced by the NSI software (which uses an algorithm based on ME). It should be noted that the FF produced by the NSI software includes probe compensation[1] (or correction), and the other produced FF patterns do not. For this reason the discrepancies between the calculated FF patterns and the 'true' FF will be less if probe correction is implemented in the algorithms. In addition, the FF patterns shown are truncated according to the critical angle of 52° corresponding to the second measurement plane.

The FF patterns produced using the SRM, MR-SRM, and the IFT with the phaseless measurement data are shown in Figure 6.24. In addition to the FF plots, the FF discrepancy (relative to the pattern provided by the NSI software) and other performance metrics are shown in Table 6.5. As can be seen from the FF plots and the tables, the SRM resulted in a slight improvement in terms of the FF discrepancy compared with ME when phase information was used. Without phase information, the inclusion of MR resulted in a significantly lower FF discrepancy than both the SRM and the IFT. One other important observation is that the SRM methods (both with and without MR) produced FF radiation

[1]Probe compensation attempts to take into account and remove the effect of the probe pattern in performing NF antenna measurements.

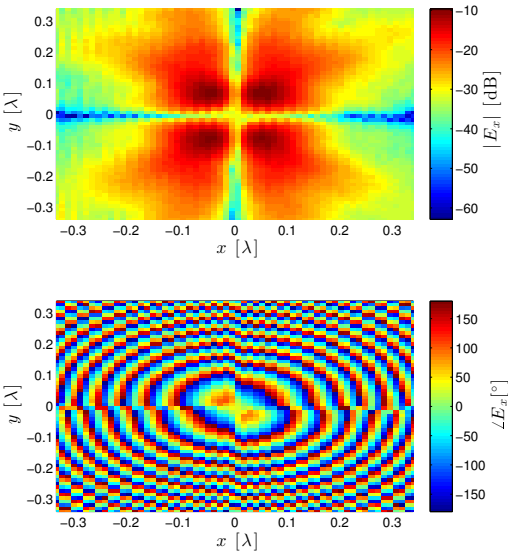

(a) Measured E_x, 1^{st} plane

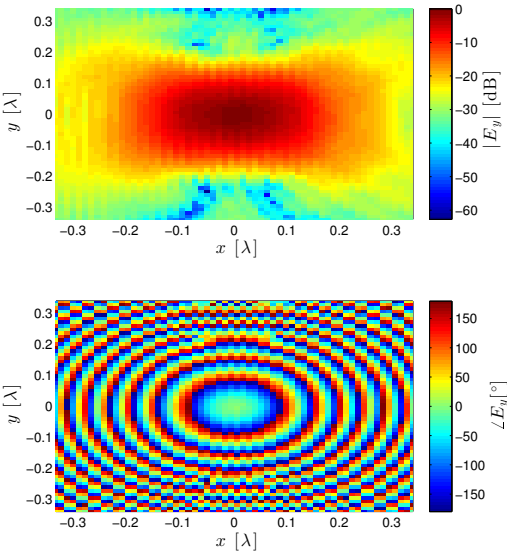

(b) Measured E_y, 1^{st} plane

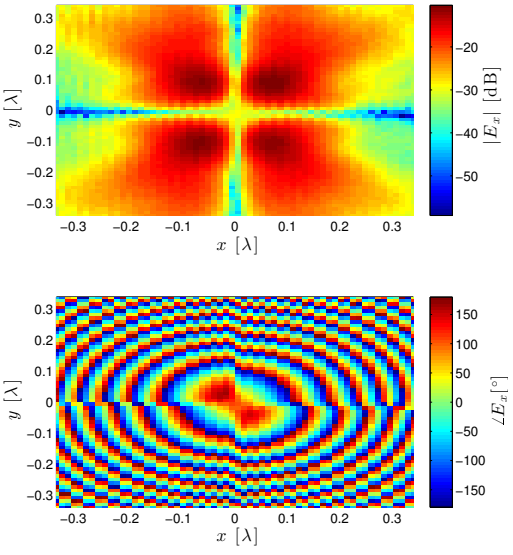

(c) Measured E_x, 2^{nd} plane

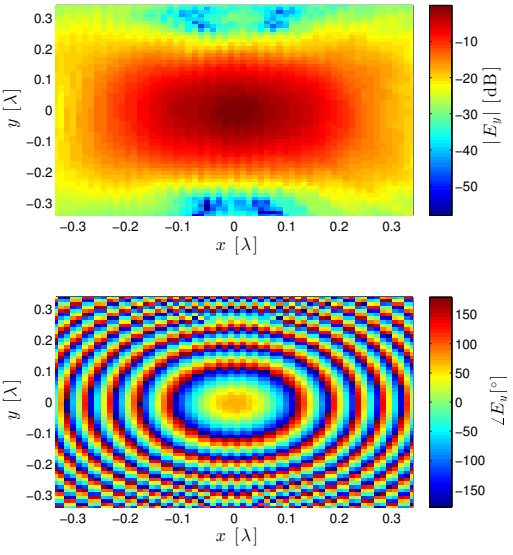

(d) Measured E_y, 2^{nd} plane

Fig. 6.22: The experimentally collected NF data on the measurement planes located 4.68λ [(a) and (b), E_x and E_y] and 6.51λ [(c) and (d), E_x and E_y] away from the AUT.

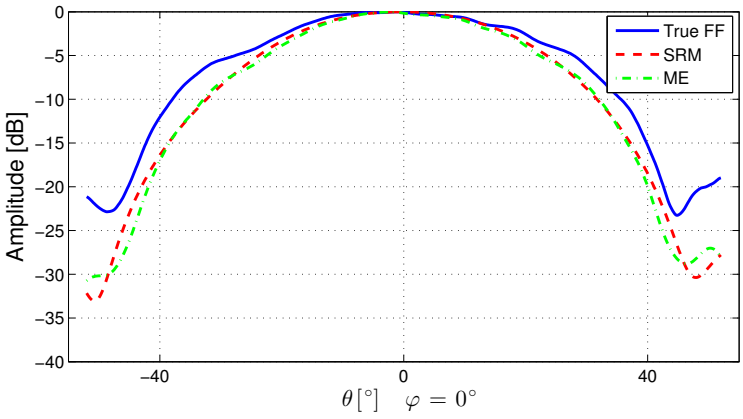

(a)

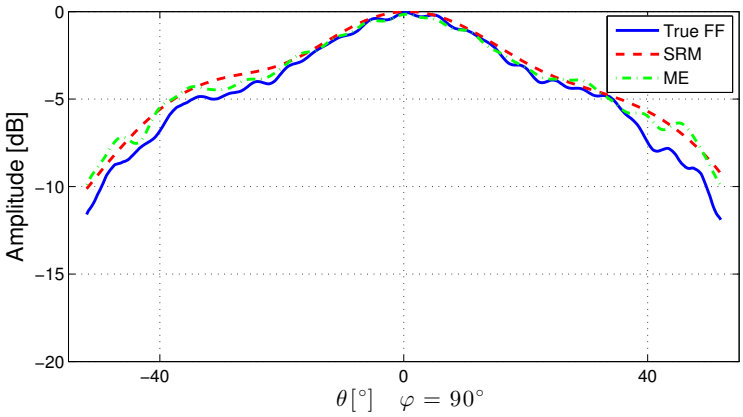

(b)

Fig. 6.23: A comparison of the dual-ridged horn FF produced from the measured NF data with both amplitude and phase at two different cuts: $\varphi = 0°$ and $\varphi = 90°$. Results are shown for the FF provided by the NSI software (blue solid line; denoted as 'True FF') and the FF produced by: (i) SRM (red dashed line) and (ii) ME (green dash-dotted line).

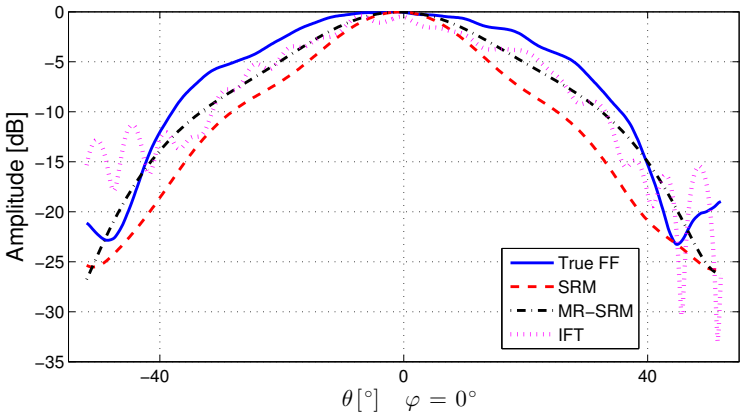

(a)

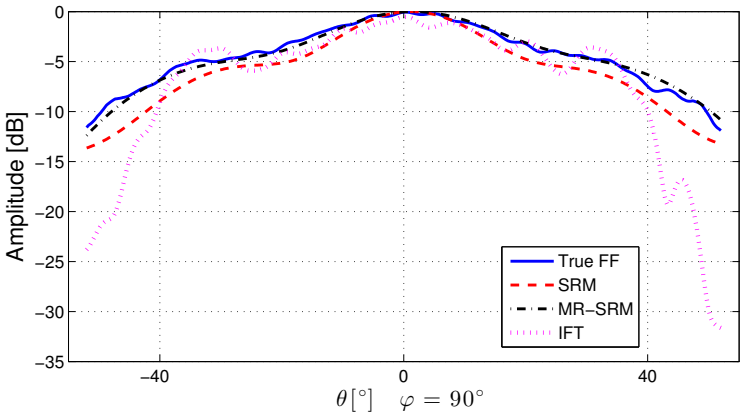

(b)

Fig. 6.24: A comparison of the dual-ridged horn FF produced from the measured NF data *without phase information*. Results are shown for the FF provided by the NSI software (blue solid line; denoted as 'True FF') and the FF produced by: (i) SRM without MR (red dashed line); (ii) MR-SRM (black dash-dotted line); and, (iii) IFT (magenta dotted line).

Table 6.5: Dual-ridged Horn Results

	SRM (w/phase)	ME (w/phase)	MR-SRM	SRM	IFT
FF discrepancy	9.82%	10.1%	12.1%	23.4%	19.4%
Iterations	66	N/A	38	194	2000
Min. Time	7.38 s	N/A	13.79 s	1 min 10 s	7.86 s
Memory	310 MB	8.06 MB	416 MB	416 MB	20.10 MB

patterns that did not exhibit the 'ripples' that can be found in the FF patterns produced by the IFT and (to a lesser degree) ME and the NSI software. These 'ripples' are most likely due to unwanted interference and multiple reflections in the anechoic chamber and these results show that the SRM is able to naturally filter out these effects. In the phaseless test MR-SRM did not require many iterations before the stopping criterion was met, and this resulted in a computational time that is comparable with the time required by the IFT.

The reconstructed equivalent currents produced by SRM and MR-SRM using the phaseless measurement data are shown in Figures 6.25 and 6.26. Although we do not have the true aperture fields of the AUT for comparison, intuitively the current distribution produced using MR-SRM is more realistic than that produced by SRM. Without MR the magnitude of the magnetic current is large around the edges of the aperture, but we know this is not possible since the tangential electric field must be zero on the surface of a PEC (the edge of the horn aperture).

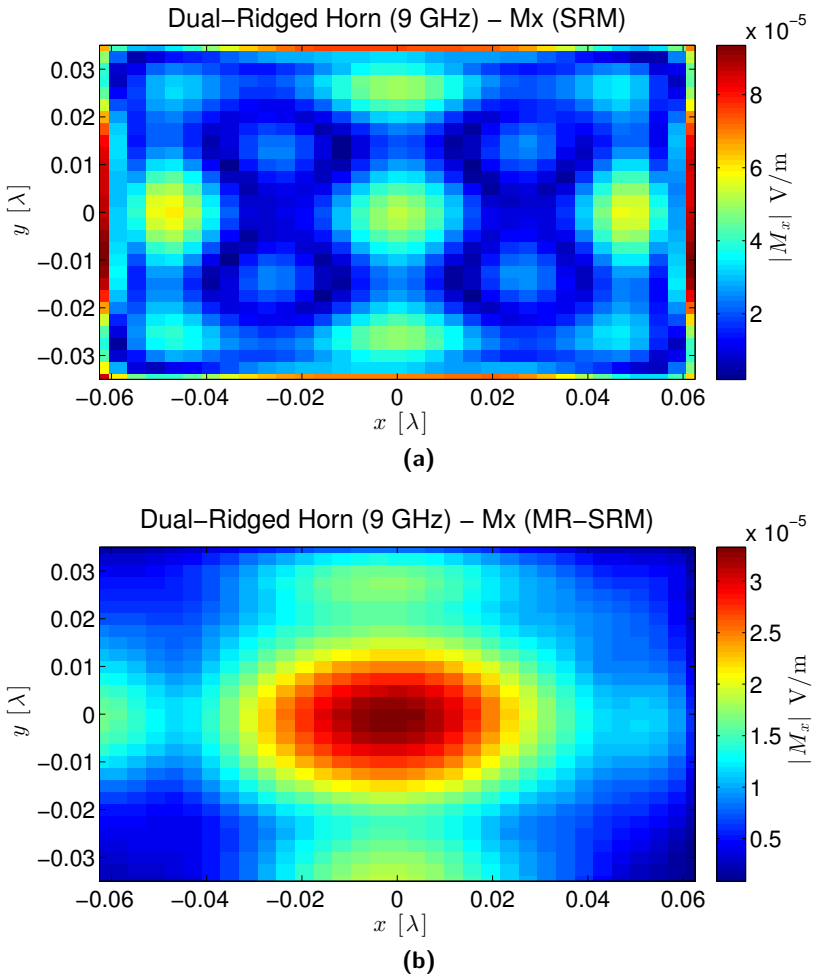

Fig. 6.25: A comparison of the x-directed equivalent magnetic current distribution produced by (a) SRM without MR and (b) MR-SRM for the dual-ridged horn antenna using phaseless NF data.

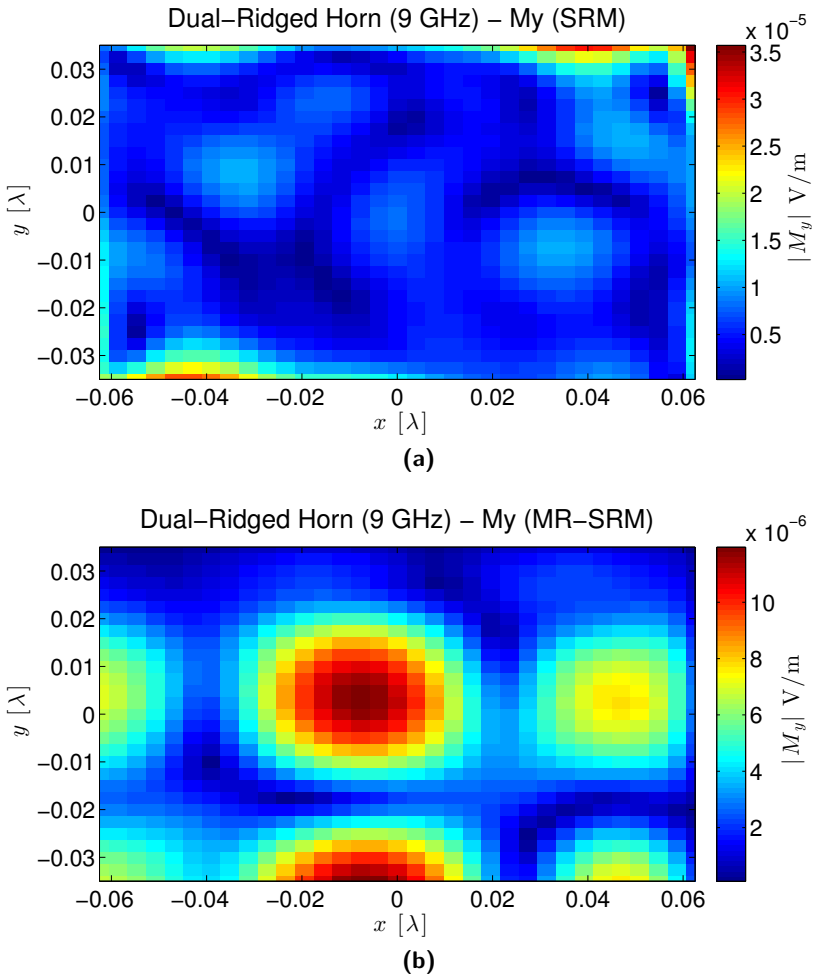

Fig. 6.26: A comparison of the y-directed equivalent magnetic current distribution produced by (a) SRM without MR and (b) MR-SRM for the dual-ridged horn antenna using phaseless NF data.

Chapter 7

Conclusions and Future Work

In this thesis we analyzed the problem of characterizing antennas using phaseless (amplitude-only) near-field measurement data. To this end, we developed an understanding of the theory behind near-field measurements when phase data are available, particularly the concept of modal expansion (ME) and the source reconstruction method (SRM). We then summarized how these methods can be extended to the case when phase information is not available/reliable, and discussed the challenges pertaining to each class of methods.

We initially described the details of a numerical implementation of the SRM for spherical NF measurements. An explanation of the challenges arising from the ill-posed nature of the problem were presented along with an overview of the truncated singular value decomposition and conjugate gradient procedures that can be used to seek solutions. The mathematical framework required to extend the SRM to the phaseless measurement case was derived fully, along with the expressions required to minimize the phaseless cost functional using the conjugate gradient method. Secondly, the details of the implementation for planar NF measurements were presented along with a description of several practical simplifications resulting from the planar geometry. In order to overcome the difficulty of selecting a regularization parameter, a multiplicative regularization (MR) scheme was introduced.

The MR scheme was adapted from inverse scattering and image deblurring problems to suit the nonlinear cost functional for phaseless NF measurements and incorporates adaptive regularization and edge-preserving characteristics.

The spherical SRM was evaluated using several synthetic examples demonstrating the performance of the SRM in the presence of noise. Examples using synthetic data were presented to evaluate the planar SRM (with and without phase data) and the developed MR-SRM. The developed methods were compared with the state-of-the-art ME method and the iterative Fourier technique (IFT), and the SRM-based methods consistently produced more accurate FF patterns. The inclusion of MR further improved the accuracy of the FF pattern and resulted in equivalent current distributions that can be used for antenna diagnostics. MR-SRM was also able to reasonably reconstruct the FF pattern of a scanned beam antenna without any prior knowledge of the beam direction. Lastly, conclusions drawn from the synthetic tests were strengthened by another comparison using experimentally collected NF data with the planar algorithms.

The results and analysis presented in this thesis show that the SRM and the newly developed MR-SRM have several benefits over ME and the IFT including the improved FF accuracy, the ability to provide antenna diagnostic information via the equivalent currents, and the potential advantage of being able to naturally filter out the effects multiple reflections and interference. This being said, the developed SRM and MR-SRM are not without limitations. In many cases, the time and memory required to perform the NF-FF transformations can become significantly larger than ME and the IFT, and may even become impractical for larger antennas and higher frequencies. In conclusion, we believe the SRM and MR-SRM both have the potential to be viable choices for performing antenna characterization using phaseless NF measurement data. In particular, the proposed MR-SRM is advantageous since it is automated and therefore the user does not need to adjust any parameters including the initial guess or regularization parameters.

There are several possible extensions of this work that should be investigated. First of all, the developed SRM algorithm could be extended to arbitrary measurement geometries, resulting in a unified, general method that would be suitable for any antenna measurement system. Next, the developed MR framework could be extended to measurement geometries beyond the planar case, and its advantages and disadvantages could then be studied in more detail. Also, instead of using a reconstruction surface of standard shape (sphere, box, plane, etc.), creating a reconstruction surface that conforms to the antenna under test would allow for more useful diagnostic information and analysis. To make the developed SRM and MR-SRM algorithms more suitable for commercial use, the use of appropriate acceleration and compression techniques should be further studied. Lastly, the inclusion of probe compensation is necessary for the developed SRM techniques to be practically useful.

References

[1] Y. Álvarez, F. Las-Heras, and M. R. Pino, "Reconstruction of equivalent currents distribution over arbitrary three-dimensional surfaces based on integral equation algorithms," *Antennas and Propagation, IEEE Transactions on*, vol. 55, no. 12, pp. 3460–3468, 2007.

[2] C. A. Balanis, *Antenna theory: analysis and design*. John Wiley & Sons, 2005, vol. 1.

[3] T. Isernia, G. Leone, and R. Pierri, "New approach to antenna testing from near field phaseless data: the cylindrical scanning," in *IEE Proceedings H (Microwaves, Antennas and Propagation)*, vol. 139, no. 4. IET, 1992, pp. 363–368.

[4] S. F. Razavi and Y. Rahmat-Samii, "Resilience to probe-positioning errors in planar phaseless near-field measurements," *Antennas and Propagation, IEEE Transactions on*, vol. 58, no. 8, pp. 2632–2640, 2010.

[5] ——, "On the uniqueness of planar near-field phaseless antenna measurements based on two amplitude-only measurements," in *Antennas and Propagation Society International Symposium, 2008. AP-S 2008. IEEE*. IEEE, 2008, pp. 1–4.

[6] O. M. Bucci, G. D'Elia, G. Leone, and R. Pierri, "Far-field pattern determination from the near-field amplitude on two surfaces," *Antennas and Propagation, IEEE Transactions on*, vol. 38, no. 11, pp. 1772–1779, 1990.

[7] T. Isernia, G. Leone, and R. Pierri, "Radiation pattern evaluation from near-field intensities on planes," *Antennas and Propagation, IEEE Transactions on*, vol. 44, no. 5, p. 701, 1996.

[8] O. M. Bucci, G. D'Elia, and M. D. Migliore, "An effective near-field far-field transformation technique from truncated and inaccurate amplitude-only data," *Antennas and Propagation, IEEE Transactions on*, vol. 47, no. 9, pp. 1377–1385, 1999.

[9] C. Niu, Y. Maddahi, and P. Mojabi, "A pendulum-based planar near-field antenna measurement system," in *2016 IEEE International Symposium on Antennas and Propagation USNC/URSI National Radio Science Meeting*. IEEE, 2016.

[10] R. G. Yaccarino and Y. Rahmat-Samii, "Phaseless bi-polar planar near-field measurements and diagnostics of array antennas," *Antennas and Propagation, IEEE Transactions on*, vol. 47, no. 3, pp. 574–583, 1999.

[11] J.-R. Regué, M. Ribó, J.-M. Garrell, and A. Martín, "A genetic algorithm based method for source identification and far-field radiated emissions prediction from near-field measurements for PCB characterization," *Electromagnetic Compatibility, IEEE Transactions on*, vol. 43, no. 4, pp. 520–530, 2001.

[12] S. F. Razavi and Y. Rahmat-Samii, "A new look at phaseless planar near-field measurements: limitations, simulations, measurements, and a hybrid solution," *Antennas and Propagation Magazine, IEEE*, vol. 49, no. 2, pp. 170–178, 2007.

[13] S. F. Razavi, "Planar near-field phaseless measurement techniques for antenna characterization and diagnostics," Ph.D. dissertation, University of California, Los Angeles, 2011.

[14] A. Tennant, G. Junkin, and A. Anderson, "Antenna far-field predictions from two phaseless cylindrical near-field measurements," *Electronics Letters*, vol. 28, no. 23, pp. 2120–2122, 1992.

[15] C. H. Schmidt, S. Razavi, T. F. Eibert, and Y. Rahmat-Samii, "Phaseless spherical near-field antenna measurements for low and medium gain antennas," *Advances in Radio Science*, vol. 8, no. 4, pp. 43–48, 2010.

[16] P. Petre and T. K. Sarkar, "A planar near-field to far-field transformation using an equivalent magnetic current approach," in *Antennas and Propagation Society International Symposium, 1992. AP-S. 1992 Digest. Held in Conjunction with: URSI Radio Science Meeting and Nuclear EMP Meeting., IEEE.* IEEE, 1992, pp. 1534–1537.

[17] A. Taaghol and T. Sarkar, "Near-field to near/far-field transformation for arbitrary near-field geometry, utilizing an equivalent magnetic current," *Electromagnetic Compatibility, IEEE Transactions on*, vol. 38, no. 3, pp. 536–542, Aug 1996.

[18] Y. A. Lopez, F. Las-Heras Andres, M. R. Pino, and T. K. Sarkar, "An improved super-resolution source reconstruction method," *Instrumentation and Measurement, IEEE Transactions on*, vol. 58, no. 11, pp. 3855–3866, 2009.

[19] T. F. Eibert and C. H. Schmidt, "Multilevel fast multipole accelerated inverse equivalent current method employing Rao–Wilton–Glisson discretization of electric and magnetic surface currents," *Antennas and Propagation, IEEE Transactions on*, vol. 57, no. 4, pp. 1178–1185, 2009.

[20] J. L. A. Quijano and G. Vecchi, "Improved-accuracy source reconstruction on arbitrary 3-D surfaces," *Antennas and Wireless Propagation Letters, IEEE*, vol. 8, pp. 1046–1049, 2009.

[21] L. Foged, L. Scialacqua, F. Saccardi, J. Quijano, G. Vecchi, and M. Sabbadini, "Practical application of the equivalent source method as an antenna diagnostics tool [AMTA Corner]," *Antennas and Propagation Magazine, IEEE*, vol. 54, no. 5, pp. 243–249, 2012.

[22] F. Las-Heras and T. K. Sarkar, "A direct optimization approach for source reconstruction and NF-FF transformation using amplitude-only data," *Antennas and Propagation, IEEE Transactions on*, vol. 50, no. 4, pp. 500–510, 2002.

[23] Y. Alvarez, F. Las-Heras, and M. R. Pino, "The sources reconstruction method for amplitude-only field measurements," *Antennas and Propagation, IEEE Transactions on*, vol. 58, no. 8, pp. 2776–2781, 2010.

[24] P. Li and L. J. Jiang, "An iterative source reconstruction method exploiting phaseless electric field data," *Progress In Electromagnetics Research*, vol. 134, pp. 419–435, 2013.

[25] A. Capozzoli, C. Curcio, G. D'Elia, and A. Liseno, "Effective antenna characterization at millimeter-wave frequencies and experimental validation at 100GHz," in *First Europ. Conf. on Antennas Prop.* EurAAP, 2006, pp. 1–5.

[26] P. Vinetti, "A non invasive, near-field and very near-field, phaseless antenna characterization system," Ph.D. dissertation, Università degli Studi di Napoli Federico II, 2008.

[27] A. Capozzoli, C. Curcio, G. D'Elia, and A. Liseno, "Phaseless antenna characterization by effective aperture field and data representations," *Antennas and Propagation, IEEE Transactions on*, vol. 57, no. 1, pp. 215–230, 2009.

[28] A. Abubakar and P. M. van den Berg, "Total variation as a multiplicative constraint for solving inverse problems," *Image Processing, IEEE Transactions on*, vol. 10, no. 9, pp. 1384–1392, 2001.

[29] R. F. Harrington, *Time-harmonic electromagnetic fields*. McGraw-Hill, 1961.

[30] A. D. Yaghjian, "An overview of near-field antenna measurements," *Antennas and Propagation, IEEE Transactions on*, vol. 34, no. 1, pp. 30–45, 1986.

[31] S. Schelkunoff, "Some equivalence theorems of electromagnetics and their application to radiation problems," *Bell System Technical Journal*, vol. 15, no. 1, pp. 92–112, 1936.

[32] J. Hadamard, *Lectures on Cauchy's problem in linear partial differential equations*. Courier Dover Publications, 2003.

[33] C. W. Groetsch, *The theory of Tikhonov regularization for Fredholm equations of the first kind*. Pitman Advanced Publishing Program, 1984, vol. 105.

[34] P. C. Hansen, *Rank-deficient and discrete ill-posed problems: numerical aspects of linear inversion*. Siam, 1998, vol. 4.

[35] A. Love, "The integration of the equations of propagation of electric waves." *Proceedings of the Royal Society of London*, vol. 68, no. 442-450, pp. 19–21, 1901.

[36] J. L. A. Quijano and G. Vecchi, "Field and source equivalence in source reconstruction on 3D surfaces," *Progress In Electromagnetics Research*, vol. 103, pp. 67–100, 2010.

[37] S. R. Rengarajan and Y. Rahmat-Samii, "The field equivalence principle: Illustration of the establishment of the non-intuitive null fields," *Antennas and Propagation Magazine, IEEE*, vol. 42, no. 4, pp. 122–128, 2000.

[38] P. Petre and T. K. Sarkar, "Differences between modal expansion and intergral equation methods for planar near-field to far-field transformation," *Progress In Electromagnetics Research*, vol. 12, pp. 37–56, 1996.

[39] K. Persson, M. Gustafsson, G. Kristensson, and B. Widenberg, "Radome diagnostics - source reconstruction of phase objects with an equivalent currents approach," *Antennas and Propagation, IEEE Transactions on*, vol. 62, no. 4, pp. 2041–2051, 2014.

[40] R. Pierri, G. D. Elia, and F. Soldovieri, "A two probes scanning phaseless near-field far-field transformation technique," *Antennas and Propagation, IEEE Transactions on*, vol. 47, no. 5, pp. 792–802, 1999.

[41] X. Li, "Investigation of the iterative Fourier technique for phaseless planar near-field antenna measurements," Master's thesis, University of Manitoba, 2015.

[42] E. Joy, *Near-field Antenna Measurement Techniques.* Georgia Tech Distance Learning and Professional Education, 2012.

[43] S. M. Rao, D. Wilton, and A. W. Glisson, "Electromagnetic scattering by surfaces of arbitrary shape," *Antennas and Propagation, IEEE Transactions on*, vol. 30, no. 3, pp. 409–418, 1982.

[44] K. Sarabandi, *EECS 730 Lecture: Dyadic Green's Function.* University of Michigan, 2009.

[45] Encyclopaedia of cubature formulas. [Online]. Available: http://nines.cs.kuleuven.be/research/ecf/ecf.html

[46] P. C. Hansen, "The discrete Picard condition for discrete ill-posed problems," *BIT Numerical Mathematics*, vol. 30, no. 4, pp. 658–672, 1990.

[47] ——, "The truncated SVD as a method for regularization," *BIT Numerical Mathematics*, vol. 27, no. 4, pp. 534–553, 1987.

[48] J. R. Shewchuk, "An introduction to the conjugate gradient method without the agonizing pain," 1994.

[49] E. Polak and G. Ribiere, "Note sur la convergence de méthodes de directions conjuguées," *Revue française d'informatique et de recherche opérationnelle, série rouge*, vol. 3, no. 1, pp. 35–43, 1969.

[50] R. Fletcher and C. M. Reeves, "Function minimization by conjugate gradients," *The computer journal*, vol. 7, no. 2, pp. 149–154, 1964.

[51] P. C. Hansen, *The L-curve and its use in the numerical treatment of inverse problems*. IMM, Department of Mathematical Modelling, Technical University of Denmark, 1999.

[52] H. Li and T. Adali, "Complex-valued adaptive signal processing using nonlinear functions," *EURASIP Journal on Advances in Signal Processing*, vol. 2008, p. 122, 2008.

[53] P. Mojabi, "Investigation and development of algorithms and techniques for microwave tomography," Ph.D. dissertation, University of Manitoba, 2010.

[54] P. Mojabi and J. LoVetri, "Use of Wirtinger calculus in Gauss-Newton inversion of microwave tomography data," in *General Assembly and Scientific Symposium (URSI GASS), 2014 XXXIth URSI*. IEEE, 2014, pp. 1–4.

[55] W. Wirtinger, "Zur formalen theorie der funktionen von mehr komplexen veränderlichen," *Mathematische Annalen*, vol. 97, no. 1, pp. 357–375, 1927.

[56] D. Brandwood, "A complex gradient operator and its application in adaptive array theory," in *IEE Proceedings F: Communications Radar and Signal Processing*, vol. 130, 1983, pp. 11–16.

[57] A. Van Den Bos, "Complex gradient and Hessian," *IEE Proceedings-Vision, Image and Signal Processing*, vol. 141, no. 6, pp. 380–383, 1994.

[58] G. Wahba, *Spline models for observational data*. Siam, 1990, vol. 59.

[59] P. Mojabi and J. LoVetri, "Overview and classification of some regularization techniques for the Gauss-Newton inversion method applied to inverse scattering problems," *Antennas and Propagation, IEEE Transactions on*, vol. 57, no. 9, pp. 2658–2665, 2009.

[60] A. Abubakar, P. M. van den Berg, T. M. Habashy, and H. Braunisch, "A multiplicative regularization approach for deblurring problems," *Image Processing, IEEE Transactions on*, vol. 13, no. 11, pp. 1524–1532, 2004.

[61] A. Abubakar, W. Hu, P. van den Berg, and T. Habashy, "A finite-difference contrast source inversion method," *Inverse Problems*, vol. 24, no. 6, p. 065004, 2008.

[62] A. Abubakar and P. M. van den Berg, "Iterative forward and inverse algorithms based on domain integral equations for three-dimensional electric and magnetic objects," *Journal of Computational Physics*, vol. 195, no. 1, pp. 236 – 262, 2004. [Online]. Available: http://www.sciencedirect.com/science/article/pii/S002199910300531X

[63] M. S. Zhdanov, *Geophysical inverse theory and regularization problems.* Elsevier, 2002, vol. 36.

[64] L. I. Rudin, S. Osher, and E. Fatemi, "Nonlinear total variation based noise removal algorithms," *Physica D: Nonlinear Phenomena*, vol. 60, no. 1, pp. 259–268, 1992.

[65] P. Charbonnier, L. Blanc-Feraud, G. Aubert, and M. Barlaud, "Deterministic edge-preserving regularization in computed imaging," *Image Processing, IEEE Transactions on*, vol. 6, no. 2, pp. 298–311, Feb 1997.

[66] C. Geuzaine and J.-F. Remacle, "Gmsh: A 3-D finite element mesh generator with built-in pre-and post-processing facilities," *International Journal for Numerical Methods in Engineering*, vol. 79, no. 11, pp. 1309–1331, 2009.

[67] K. Frederix and M. Van Barel, "Solving a large dense linear system by adaptive cross approximation," *Journal of computational and applied mathematics*, vol. 234, no. 11, pp. 3181–3195, 2010.

[68] C. Parini, S. Gregson, J. McCormick, and D. Janse van Rensburg, *Theory and Practice of Modern Antenna Range Measurements.* The Institution of Engineering and Technology, 2014, vol. 1.